ADVANCES IN BIOMEDICAL APPLICATIONS AND ASSESSMENT OF ULTRASOUND NONRIGID IMAGE REGISTRATION

by

Ganesh Narayanasamy

A dissertation submitted in partial fulfillment
of the requirements for the degree of
Doctor of Philosophy
(Applied Physics)
in The University of Michigan
2009

Doctoral Committee:

Professor Paul L Carson, Chair
Professor J Brian Fowlkes
Professor Bradford Orr
Professor Marilyn A Roubidoux

For My Parents

ACKNOWLEDGEMENTS

I would like to thank the financial support from the Radiology department as well as the Applied Physics program at the University of Michigan. Without this, it would have been impossible to complete such a task as Ph.D. that took around 5 years.

This is truly a work of an individual standing on the shoulders of giants. I am really indebted to my advisor, Dr. Paul L Carson for his continued academic and moral support. As a saying in Sanskrit goes, it may take a life to repay a debt but a few lifetimes to repay a guru. He has always encouraged me and believed in my abilities, even at times when I had tons of questions! His passion for science is easily noticeable as he is able to add value to people around him. Learning from his wisdom and years of experience is such a blessing.

I have also learnt a lot from my co-advisor, Dr. Brian Fowlkes. Every time that I remember walking into office, I came out having learnt something new. He is a wonderful teacher, a great leader to look up to and he inspires many people with a positive attitude. It is a nice experience working with him.

I would also like to acknowledge help from Dr. Marilyn Roubidoux for spending countless hours looking at images without complaints. Thanks to her, I am back in physical shape with a cholesterol-free diet! I would also like to acknowledge Dr. Bradford Orr for both moral and financial support, in the early years of research life in UM.

Basic Radiological Sciences has been my home for the last 5 years. I would like to thank Dr. Gerald LeCarpentier for all the discussions and ideas, Dr. Mitch Goodsitt for teaching Medical physics, Dr. Oliver Kripfgans for his charismatic enthusiasm, Dr. Aaron Moskalik for tips on statistics, Dr. Kim Ives for handling the tissue phantoms, Dr. Zhi Yang for developing software tools, Dr. Maggie Zhang for her contagious enthusiasm,

Dr. Jie Li for being goal driven, Dr. Frederic Padilla for being an unassuming individual just to name a few.

I thank all my fellow students for their help and support including Ramkrishnan Narayanan for coding skills, Titaina for her bubbly character, Rich Rhee for system administration, Huzefa Neemuchwala for all the stories about Bombay (now Mumbai), Sakina for being such a down to earth individual, Becca Booi for her inter-personal skills, Sumedha Sinha for all the ImageJ plug-ins, and Fong Ming for teaching me Field-II software. Carol Cribbins and Sharan Karahan have provided tremendous administrative support by working through hoops of regulations and countless paper work. Special thanks go to Carol for proof-reading my papers. I would also like to acknowledge the software support provided by Peyton Bland and Gary Laderach in Digital Image Processing Lab (DIPL), Radiology Department, University of Michigan Health System.

I am also indebted to Applied Physics program and the close-knit family. Special thanks goes to Cynthia McNabb, Charles Sutton for making me feel very welcome when I was new in Ann Arbor and also helping me navigate through maze of rules and regulations.

Finally I would like to thank my entire family for their love and unflinching support especially my mom Bhuvaneswari, dad Narayanasamy, brother Balasubramanian and sister Vijayalakshmi. A great human being that I am blessed with in our family is my granddad Shri. Viswapathy Sastrigal. Last but not the least is the last few years with my wife, Anu. I only hope to live up to her level of compassion, love and friendliness to everybody around.

Ann Arbor
Nov 2009

TABLE OF CONTENTS

LIST OF FIGURES

LIST OF TABLES

ABSTRACT

ADVANCES IN BIOMEDICAL APPLICATIONS AND ASSESSMENT OF ULTRASOUND NONRIGID IMAGE REGISTRATION

by

Ganesh Narayanasamy

Chair: Paul L Carson

Image volume based registration (IVBaR) is the process of determining a one-to-one transformation between points in two images that relates the information in one image to that in the other image quantitatively. IVBaR is done primarily to spatially align the two images in the same coordinate system in order to allow better comparison and visualization of changes. The potential use of IVBaR has been explored in three different contexts.

In a preliminary study on identification of biometric from internal finger structure, semi-automated IVBaR-based study provided a sensitivity and specificity of 0.93 and 1.00 respectively. Visual matching of all image pairs by four readers yielded 96% successful match.

IVBaR could potentially be useful for routine breast cancer screening and diagnosis. Nearly whole breast ultrasound (US) scanning with mammographic-style compression and successful IVBaR were achieved. The image volume was registered off-

line with a mutual information cost function and global interpolation based on the non-rigid thin-plate spline deformation. This Institutional Review Board approved study was conducted on 10 patients undergoing chemotherapy and 14 patients with a suspicious/unknown mass scheduled to undergo biopsy. IVBaR was successful with mean registration error (MRE) of 5.2±2 mm in 12 of 17 ABU image pairs collected before, during or after 115±14 days of chemotherapy. Semi-automated tumor volume estimation was performed on registered image volumes giving 86±8% mean accuracy compared with a radiologist hand-segmented tumor volume on 7 cases with correlation coefficient of 0.99 ($p<0.001$). In a reader study by 3 radiologists assigned to mark the tumor boundary, significant reduction in time taken ($p<0.03$) was seen due to IVBaR in 6 cases. Three new methods were developed for independent validation of IVBaR based on Doppler US signals.

Non-rigid registration tools were also applied in the field of interventional guidance of medical tools used in minimally invasive surgery. The mean positional error in a CT scanner environment improved from 3.9±1.5 mm to 1.0±0.3 mm ($p<0.0002$).

These results show that 3D image volumes and data can be spatially aligned using non-rigid registration for comparison as well as quantification of changes.

CHAPTER 1 INTRODUCTION

In this thesis, image volume based registration (IVBaR) has been developed and applied to three-dimensional (3D) ultrasound (US) imaging for easy comparison of image volumes for identification of similar pattern, detection of lesion, for tumor volume change estimation as well as in interventional guidance.

Medical imaging involves physical imaging techniques that can produce images of internal organs of the body, non-invasively. This has served multiple purposes such as diagnosis, planning and monitoring treatment of diseases.[1] Image-guided therapy and measuring the effectiveness of therapy can also be considered as an extension of medical imaging. As a field, medical imaging has diversified from primarily X-ray imaging (penetration of ionizing radiation through biological tissue) and matured into a multi-modality field that uses various technologies that serve the clinicians. For example, in radiotherapy, medical imaging allows the delivery of a fatal dose of radiation to a tumor with minimal collateral damage to healthy tissue. Each of the modalities deals with studying the physical properties of biological tissue using various forms of energy.[2] While conventional X-ray systems provide projection image of the 3D object in 2D space, modern day imaging systems provide 4D (3D in real-time) information.

The rapid development and proliferation of medical imaging technologies is revolutionizing medicine. Medical imaging allows scientists and physicians to obtain potentially lifesaving information by looking non-invasively into the human body. Beyond the simple visualization and inspection of anatomic structures, it has evolved into a tool for intra-operative navigation, radiotherapy planning, surgical planning, and for tracking the progress of disease. The arsenal of imaging tools available to radiologists has shown considerable improvement over the last two decades, mainly because of key scientific and technological advancements, inexpensive computational resources and the people involved as well as with emergence of new modalities.[3]

US has been a very useful modality for imaging soft-tissue including muscles using acoustics or sound waves.[4] This fifty plus year-old field has gained importance in clinical utility due to its non-ionizing radiation, faster image acquisition, smaller sized portable scanners and inexpensive over other modalities including Magnetic Resonance Imaging (MRI) and Computed Tomography (CT).[5] Real-time live update in US imaging helps in fetal imaging, cardiac imaging as well as US-guided interventional procedures like biopsies, aspirations and surgeries.[6, 7] US had been used predominantly as a diagnostic tool for non-invasive studies of the body organs like in breast, heart valve, liver, kidney etc while therapeutic uses have been gaining importance since the last few years. In dealing with breast imaging, US is used mainly for distinguishing solid tumors from fluid-filled cysts primarily in dense breasts. For breast tumor and peripheral imaging (of interest in this thesis), US uses backscatter and Doppler imaging techniques.

Although modern imaging devices provide exceptional views of internal anatomy, the use of computers to quantify and analyze the embedded structures with accuracy and efficiency is limited. Accurate, repeatable, quantitative data must be efficiently extracted in order to support the spectrum of biomedical investigations and clinical activities. With medical imaging playing an increasingly prominent role in the diagnosis and treatment of disease, there have been many challenges in extracting clinically useful information about anatomic structures imaged through CT, MR, PET, and other modalities, even with the assistance of computers.[8] Medical image processing holds exciting prospects for improved detection and diagnostic accuracy.[9, 10] Medical image processing can be categorized into three main categories:[11]

a. image processing to enhance the visual perception of digital images;
b. image analysis for determining and computing quantitative measures;
c. pattern recognition in the classification of anatomic features based on certain dimensions, shape and texture.

This thesis explores one aspect of image analysis - registration on 3D-US images in the clinical application of identification of structures, lesion detection, measurement of tumor volume change, and effectiveness of therapy.[12, 13] IVBaR is the process of transforming images acquired in different conditions into one coordinate system that facilitates comparison, integration of data and also measurement of changes.[14, 15]

Performed on sequential images, IVBaR could help measurement of change with time. [16] Registration of 3D US image volumes are, however, challenging due to the presence of speckle noise, large dependence of sound wave on incident angle and also shadow artifact. [17] Some of these limitations are inherent to US imaging and could be partly overcome using compound imaging, filtering etc. We have addressed a few such issues in this thesis that could eventually lead to more sophisticated image registration tools.

1.1 Ultrasound Imaging

US medical imaging is the acoustic mapping of the mechanical structures of the body determined by density and elasticity or stiffness. It is based on pulse-echo techniques to study the human or animal anatomy, mainly for medical purposes. US imaging is performed by transmission of high frequency longitudinal sound waves (2-20 megahertz range) produced most commonly by piezoelectric ultrasonic transducers in contact with the target to be imaged. This sound energy gets scattered, absorbed, reflected, and refracted by the target organ and tissue along the path leading to the target organ.

A basic assumption in US imaging is the homogeneity of the medium of propagation and therefore, a constant, isotropic speed-of-sound. Due to high water content, soft tissue and many organs of the body are assumed to have the same speed-of-sound as in water at room temperature. Acoustic impedance *(Z)* of a medium is defined as the product of density of medium (ρ) and speed-of-sound in the medium (c), $Z=\rho c$. The amplitude reflection factor of normally incident plane waves at the interface between 2 media with impedances Z_1 and Z_2 is given by the ratio $R=(Z_2-Z_1)/(Z_2+Z_1)$. Therefore some variation in sound speed and density among tissues is necessary as a source of contrast in imaging.

The shape of the US pulse determines the resolution of an imaging system. In conventional piezoelectric transducer, electrical signal excites the transducer element with a short pulse that propagates sound wave through the target and reflects off the impedance inhomogeneities. The incident US beam profile depends on the spectrum of the pulse exciting the transducer and also transducer properties like aperture size and shape, resonance frequency and damping. The cross-section of the beam is depth-

dependent and is defined by both the lateral and the elevational extent of the beam. The US beam width narrows as it reaches the focal length (determined by transducer properties, user settings) and broadens beyond the focal zone.

US transducers come in various types, shapes and sizes including linear array, curved array, phased-array etc. In our study, linear array consisting of 128-512 piezoelectric elements was used. Multiplexer selects a small subset of adjacent elements that forms the active aperture at any time. These elements are simultaneously activated to transmit acoustic waves onto the target with fixed focal delay. These individual beams interact via constructive and destructive interference to produce a single collimated beam that has similar properties of that from a single element transducer of the same size. Lateral image resolution depends on the number of active elements during transmission as well as shape of the beam.

Image for display is formed by converting the amplitude of the received signal into grayscale level brightness. The amplitude of reflected component depends on the impedance of the tissue layers and direction of propagation of sound waves. Sound waves incident normal to a boundary with an impedance change creates the large reflection component. The reflected echoes are detected by the same transducer and converted into electrical signal and is shown as a bright structure in the display. A two-dimensional (2D) US image is obtained from the reflected signal as a function of time. Reflected signal received along each vertical line in imaging plane is called an “A-mode” (for amplitude) line or “A-line”. In “M-mode” (for motion), acoustic signals at a fixed location are displayed as a function of time. In the receive mode, echoes are received by acquiring signals from most of the elements and an A-line is formed at the center of the active element group. Subsequent A-line acquisition occurs by firing the adjacent set of transducer elements that are displaced by one or two elements. Spatially adjacent A-lines acquired likewise forms a 2D B-mode grayscale image with rectangular field of view. Grayscale picture formed with brightness scale proportional to the echo strength is “B-mode” (for brightness) image.

While 2D-US has been in use for a long time, 3D volumetric information was missing until a few decades ago. The first instance of 3D information was collected in early 1970’s when physicians were presented stack 2D CT image slices of the body.

Using conventional 2D imaging, the diagnostician must mentally transform the series of 2D images into volumetric information in order to obtain 3D impression of the anatomy and this was largely based on their experience. The volume of an organ is computed from 2D images that have information of only two of the three dimensions with assumptions about the missing third dimension that depends on interpretation by user and is error-prone. In certain body organs, it is difficult to find the best 2D imaging plane and is often difficult to replicate the scanning at a later time.

The goal of 3D US imaging is to overcome these limitations thus providing clinicians with a complete view of anatomy of the target organ. 3D US transducers are available commercially in recent times. Some of them have a 2D array of transducer elements with 100s of elements and as many number of connectors. Most of the commercially available 3D US transducers have a linear array of elements that is mechanically scanned or tilted to image a 3D volume of interest (VOI). Position encoders in the linear array provide the position and orientation of each imaging plane. Considerable interpolation is involved in forming 3D image volume and adequate sampling is needed along the elevation direction.

Other commonly used US modes are spatial and frequency compounding, Doppler (color flow and power mode), tissue Doppler, harmonic imaging and elasticity to name a few. Spatial compounding in US imaging is performed by imaging the region of interest repeatedly from different look directions and by averaging the values from the intersecting B-mode scans. In a modern day scanner, spatial compound image is constructed with three to eleven sweeps of the beam from one end of the transducer to the other. All sweeps are created by electronic beam steering at different angles of incidence creating a spatially and temporally compounded image. [18] This was shown to have better signal-to-noise ratio and reduced shadow, speckle artifacts. [19]

Doppler US imaging focuses on visualization and measurement of blood flow in the body. Blood velocity can be measured from frequency shift of reflected echo received from the target in motion with respect to the stationary transducer. In this modality, several narrow band pulses are transmitted and velocity of motion is detected by comparisons of phase shifts between pulses scattering from the moving target. In color Doppler (CD) imaging mode, color is displayed when the frequency shift is higher than a

user-defined threshold, otherwise the B-mode component gets displayed. In CD mode, resolution of grayscale pixels is lower than that of regular B-mode imaging at identical central frequency as the pulses have narrow bandwidth.

1.2 Artifacts in US imaging

While all imaging systems have artifacts, an appreciation of artifacts would likely enhance the clinical utility of US imaging. US suffers from loss of contrast and image resolution due to spatially varying speed-of-sound along the path traversed by US to reach the target. [20] Changes in speed-of-sound cause errors in transmission (focusing) as well as on reception (image reconstruction). These can be overcome by imaging an area near the VOI that has structures with known and uniform speed-of-sound. US imaging, along with other coherent imaging systems, suffers from speckle noise caused by interference effects between overlapping echoes from randomly distributed sub-resolution scatterers.[21] Speckle is a random interference pattern and the texture does not correspond to real structure. It degrades the signal to noise ratio of the image and can be tackled using filtering and compound imaging.

Reverberation artifact is seen as equally spaced artifactual echoes along the direction of propagation of US waves away from the real structures. In this study, reverberations are predominantly caused by the use of a thin plastic-like membrane for mammography-like uniform compression of the breast.

While shadowing artifact results from strongly attenuating structures, low attenuating objects along the direction of sound wave propagation causes enhancement. Shadowing and enhancement artifacts are very useful artifacts and helps in identification of tumor and cysts, respectively. Mirror image artifacts are caused by the presence of a strong reflector when structures present in one side appears on the other side as well.[22] Other artifacts include refraction artifacts caused at curved surface of structures like breast, comet-tail artifacts seen in lung alveoli, side lobe and grating lobe artifacts, artifacts from tissue with inhomogeneous speed of sound etc. Reflection from distinct tissue boundaries (specular) is very direction dependent resulting in images that are hard

to interpret.[23] Spatial resolution (mainly in the elevational direction to the US transducer) limits the ability to resolve two adjacent structures leading to loss of detail.

Artifacts in Doppler imaging are mainly due to aliasing or flash resulting in range ambiguity artifact. Cardiac motion or pulsatility of blood flow exacerbates some of the Doppler artifacts.[24] Ways to minimize the reverberation artifacts in Doppler due to the presence of a thin membrane between tissue and transducer are addressed in chapter 2. The spatial and temporal resolution of Doppler imaging is less than that of the B-mode US imaging on which it is superimposed.[25]

1.3 Image Volume Based Registration (IVBaR)

The amount of interest and need for image registration can be seen from the extensive publications on this topic. Spatial registration is a technique of aligning images in the same coordinate system for purposes of comparison as well as visualization of change. Manual registration for evaluation of large sets of image volumes may be extremely time-consuming and subject to substantial user variability depending on skill, patience and experience. Registration helps in correcting slight differences in scan positioning of the patient that resolves ambiguities in location of some of the structures. Multi-modal image registration works by integration and fusion of information from different modalities. In this study, semi-automated registration has been applied on 3D US image volumes.

A well studied suite of software, MIAMI-Fuse©, used in this study and developed at the University of Michigan works by maximizing a similarity measure, the classical Shannon mutual information (MI). MI of image intensity values of the corresponding voxel pairs is maximal if the two images are geometrically aligned which is discussed elsewhere in the literature.[26,27,28] MI of an US image volume pair depends on the amount of true structural information like specular reflectors and is affected by artifacts from shadowing, deformation of tissue, coherent echoes from structures larger than wavelength, refraction etc.[13] As a first step of registration, a 3D full-affine transformation was performed to take into account linear changes in an image volume that are global in nature like translation, rotation, scaling and shear. In order to accommodate elastic nature

of organs like breast mass with different elastic modulus than the surrounding tissue, a geometric model with a higher degree of freedom like warping is needed.[13] Registration using thin-plate spline (TPS) warping algorithm based on user-defined control points has been studied to show the significance of warping in correcting for images. [29, 30] User input is needed in the form of manual selection of control point pairs at approximately corresponding locations on the tissue structures in the image volume pair.[31] In this study, we have performed registration of US image volumes using control points based TPS warping algorithm with MI as the cost function and compared the results with that from an affine transformation. Registration is achieved by moving the control points so that MI is maximized.

Speckle degrades the signal to noise ratio of the image and this could lead to reduced performance in registration.[13] Signal processing could enhance the edges, reduce noise in the image and improve information content in the image and thereby image registration.

1.4 Finger Imaging and Biometric Study

Identification based on a fool-proof biometric system is the need of the hour in our society for safety and security of people. Biometrics refers to methods of unique identification or verification of human beings based on one or more intrinsic physical or behavioral traits. These traits should be universal, permanent (ageless) and unique to the individual. Biometric system based on such traits should have negligible false positives, and false negatives, ease of acquisition, social acceptance, convenience of use and also be economical. From the 2D image of the finger surface, it would be impossible to say whether the person is alive or not. On the other hand, the internal anatomic structures that are presumably unique might serve as a path towards achieving a fool-proof, secure identification system. Doppler US imaging could measure physiologic and vital status of a human being, although there are challenges. A novel 3D-US based on internal finger structures with a potential to become a secondary biometric identifier has been explored in this work.

1.5 Tumor Volume estimation: Phantom and *in-vivo* study

Size or volume of tumor has been a main prognostic factor of the tumor and could provide information about lethality and survival time. Estimation of tumor volume remains a challenge to date, mainly due to poor differentiation of tumor from surrounding soft tissue and difficulties in defining the tumor boundary. For chemo, radiation or hormonal therapy trials, it is of vital importance to measure the tumor volume accurately to determine the effectiveness of therapy. Complete and partial responders are preferred for continuation of treatment, but stable and progressive diseases need an alternate cure or a stronger dose of treatment. Early prediction of response to therapy could mean the difference between life and death in some cases.

Conventionally, largest length of cross-section of the tumor was considered as equivalent to the size of tumor. In 3D-US imaging, measurement of approximate tumor volume was obtained from ellipsoidal formula using height, width and depth. Accurate tumor volume measurement is obtained via manual segmentation by a radiologist. However, this is time consuming and suffers from inter and intra-reader variability. Semi-automated tumor volume estimation based on IVBaR of tumor image volumes acquired before and after chemotherapy has been attempted here. Radiologist hand segmentation was performed for verification of semi-automated tumor volume measurement.

Phantom made with tissue-like material has been modified for studying tumor volume change estimation. An insertion was made in the phantom where a balloon catheter of variable quantity of saline at room temperature was placed in order to mimic cyst. By using this phantom, the user has complete control over the tumor volume, shape as well as the background. However, as seen in the study, a sufficient amount of scatters or information content is needed to drive the registration. A fundamental assumption in this study is that the therapy alters the internal structure of the tumor leaving the background intact, which is true in many cases. The information in background structures was utilized to perform IVBaR. Transformation parameters of IVBaR were used in estimation of tumor volume and volume change.

1.6 Non-rigid Registration for interventional guidance

Currently, interventional radiology has relied on real-time imaging to monitor anatomic position and guide device navigation during procedures. US, fluoroscopy or CT imaging was utilized for this purpose with physicians making a mental note of anatomic information from previously acquired MRI or CT imaging. This process is prone to human error and depends on the experience of the physician performing the procedure.[32]

Electromagnetic (EM) navigation provides device navigation along with anatomic position from previously acquired and real-time images. Many procedures could benefit from this development including endoscopy, biopsy, thermal ablation etc. EM tracking systems suffer from EM field distortions due to presence of metal and ferromagnetic material in a clinical environment. In this work, modeling of the EM field distortion pattern was attempted with known positions of EM sensors on a CT patient table. Accuracy and validation of rigid and non-rigid distortion pattern was also studied.

1.7 Thesis Overview

The purpose of this research study is to assess physiologic and anatomic changes in human body using semi-automated IVBaR and visual study by radiologists. At the time of this writing, chapter 2 was published in the journal 'Ultrasound in Medicine and Biology'. chapter 3 was published in the journal 'Medical Physics'.

chapter 2 focuses on identification of individuals using 3D internal finger structure as imaged by US. This could act as a supplemental biometric measure and also provides ways to assess physiologic and cardiovascular status. This study is divided into 3 main parts: semi-automated IVBaR, a visual study by radiologists and Doppler study.

In chapter 3, anatomic changes in the breast during chemotherapy treatment of tumor are measured quantitatively using IVBaR on US image volume. Some new accuracy measures of IVBaR are evaluated using Doppler imaging that is independent of the original grayscale image used in registration.

chapter 4 reports on a reader study with radiologists, performed to assess the clinical utility of IVBaR in breast tumor volume estimation on US images. A group of radiologists marked the tumor boundary in a pair of 3D-US image volumes (typically, pre and post-chemotherapy) with and without IVBaR. The advantages of performing IVBaR for assessing tumor response to therapy are identified and studied in this chapter.

chapter 5 deals with IVBaR based lesion volume estimation on phantoms with minimal hand segmentation. A rough sketch around the lesion in one of the image volumes is needed to be able to determine where that tumor volume shrank when the subsequently collected images with different tumor volume are registered to the initial image volume. A basic assumption in this study is that the surrounding tissues remain largely unaffected while the tumor tissue can be substantially changed in response to the therapy.

chapter 6 is a first-hand application of non-rigid transformation in a clinical environment. Spatial distortions of an externally generated electromagnetic field on a CT table due to metallic and ferromagnetic materials in the vicinity are studied, corrected and tested for accuracy.

chapter 7 summarizes the conclusions of the thesis, while future work contains newer ideas for implementation that have implications to the scientific and medical community.

1.8 References

1 S Webb, “The Physics of Medical Imaging,” ISBN 0852743491, 9780852743492, 1988.

2 JT Bushberg, JA Seibert, EM Leidholdt, JM Boone, “The Essential Physics of Medical Imaging”. Lippincott Williams & Wilkins, ISBN 0683301187, 9780683301182, 2002.

3 JS Duncan, N Ayache, “Medical image analysis: progress over two decades and the challenges ahead,” IEEE Transactions on Pattern Analysis and Machine Intelligence, Vol. 22 (1), pp. 85–106, 2000.

4 TL Szabo, “Diagnostic Ultrasound Imaging: Inside Out.” Academic Press, ISBN 0126801452, 9780126801453, 2004.

5 KK Shung, “Diagnostic Ultrasound: Imaging and Blood Flow Measurements.” CRC Press, ISBN 0824740963, 9780824740962, 2005.

6 DB Kopans, “Breast Imaging.” Lippincott Williams & Wilkins, ISBN 0781747686, 9780781747684, 2006.

7 DD Dershaw, “Imaging-guided interventional breast techniques.” Springer, ISBN 0387954546, 9780387954547, 2002.

8 T McInerney, D Terzopoulos, “Deformable models in medical image analysis: a survey,” Medical Image Analysis, Vol. 1(2), pp. 91–108, 1996.

9 J Beutel, HL Kundel, RL Van Metter, ““Handbook of Medical Imaging: Medical Image Processing and Analysis.” SPIE Press, ISBN 0819436232, 9780819436238, 2000.

10 JK Udupa, GT Herman, ““3D Imaging in Medicine.” CRC Press, ISBN 084933179X, 9780849331794, 1999.

11 R Tadeusiewicz, MR Ogiela, “Medical Image Understanding Technology: Artificial Intelligence and Soft-Computing for Image Understanding.” Springer, ISBN 3540219854, 9783540219859, 2004.

12 CR Meyer, JL Boes, B Kim, PH Bland, KR Zasadny, PV Kison, K Koral, KA Frey, RL Wahl, “Demonstration of accuracy and clinical versatility of mutual information for automatic multimodality image fusion using affine and thin-plate spline warped geometric deformations,” Medical Image Analysis, Vol. 10(3), pp. 195–206, 1997.

13 CR Meyer, JL Boes, B Kim, PH Bland, GL Lecarpentier, JB Fowlkes, MA Roubidoux, PL Carson, “Semiautomatic registration of volumetric ultrasound scans,” Ultrasound Med Biol., Vol. 25(3), pp. 339–47, 1999.

14 CR Maurer, JM Fitzpatrick, “A review of medical image registration,” Proceedings Annual Interactive image guided neurosurgery Meeting, pp. 17–44, 2003.

15 FL Bookstein, “Thin-Plate splines and the atlas problem for biomedical images,” Springer-Verlag Series, ISBN 978-3-540-54246-9, 1991.

16 T Ishida, S Katsuragawa, K Nakamura, H MacMahon, K Doi, “Iterative image warping technique for temporal subtraction of sequential chest radiographs to detect interval change,” Med. Phys. Vol. 26 (7), pp. 1320–1329, 1999.

17 A Moskalik, PL Carson, CR Meyer, JB Fowlkes, JM Rubin, MA Roubidoux, “Registration of three-dimensional compound ultrasound scans of the breast for refraction and motion correction,” Ultrasound in Medicine and Biology, Vol. 21(6), pp. 769–778, 1995.

18 AT Stavros, CL Rapp, SH Parker, “Breast Ultrasound,” ISBN 039751624, 2004.

19 R Rohling, A Gee, L Berman, “Three-dimensional spatial compounding of ultrasound images,” Medical Image Analysis, Vol. 1(3), pp. 177–193, 1997.

20 ME Anderson, MS McKeag, GE Trahey, “The Impact of sound speed errors on medical ultrasound imaging,” Journal of Acoustical Society of America, Vol. 107(6), pp. 3540–8, 2000.

21 RD Park, TG Nyland, JC Lattimer, CW Miller, JL Lebel, “B-mode grayscale ultrasound: Imaging artifacts and interpretation principles,” Veterinary Radiology Ultrasound 22(5), 204–210, 1981.
22 FW Kremkau, KJ Taylor, “Artifacts in ultrasound imaging,” J. Ultras. Med. 5(4), 227–237, 1986.
23 P Carson, A Fenster, “Anniversary paper: Evolution of ultrasound physics and the role of medical physicists and the AAPM and its journal in that evolution,” Med. Phys. 36(2), 411–428, 2009.
24 TR Nelson, DH Pretorius, A Hull, M Riccabona, MS Sklansky, G James, “Sources and impacts of artifacts on clinical three-dimensional ultrasound imaging,” Ultrasound in obstetrics and gynecology, 16(4), 374–383, 2002.
25 DG Mitchell, “Color Doppler imaging: Principles, limitations and artifacts,” Radiology, 177, 1–10, 1990.
26 F Maes, A Collignon, D Vandermeulen, G Marchal, P Suetens, “Multimodality Image Registration by maximization of Mutual Information,” IEEE Transactions on Medical Imaging, Vol. 16(2), pp. 187–198, 1997.
27 P Viola, W Wells, “Alignment by Maximization of Mutual Information,” International Journal of Computer Vision, Vol. 24(2), pp. 137–154, 1997.
28 W Wells, P Viola, H Atsumi, S Nakajima, R Kikinis, “Multi-modal Volume Registration by maximization of Mutual Information,” Medical Image Analysis, Vol. 1(1), pp. 35–51, 1996.
29 FL Bookstein, “Principal Warps: Thin-Plate Splines and the Decomposition of Deformations,” IEEE Transactions on Pattern Analysis and Machine Intelligence, Vol 11(6), 1989.
30 FL Bookstein, WDK Green, “A feature space for edges in images with landmarks,” Journal of Mathematical Imaging and Vision Vol 3, pp. 231–261, 1993.
31 B Kim, JL Boes, KA Frey, CR Meyer, “Mutual information for automated unwarping of rat brain autoradiographs,” NeuroImage, Vol. 5, pp. 31–40, 1997.
32 BJ Wood, H Zhang, A Durrani, N Glossop, S Ranjan, D Lindisch, E Levy, F Banovac, J Borgert, S Krueger, J Kruecker, A Viswanathan, K Cleary, “Navigation with electromagnetic tracking for interventional radiology procedures,” J. Vasc. Interv. Radiol. 16(4), 493–505, 2005.

CHAPTER 2 ULTRASOUND OF THE FINGERS FOR HUMAN IDENTIFICATION USING BIOMETRICS

2.1 Introduction

Identification of individuals might become important in every society for safety and security of its people and their assets. Current identification methods use fingerprint systems that are susceptible to duplication and mismatch.[1]

Also, fingerprints do not indicate the vital and physiologic status of the individual, i.e. whether the person is alive or dead or extremely agitated. Even with the use of new and emerging technologies, human identification has been a challenge due to concerns of accuracy, usability, privacy and security of individuals involved.[2] The advantages of correct identification include safer medical care as well as safer societies, reduced fraud and user-friendly man-machine interfaces.

Here, we demonstrate the utility of US in identifying potential biometrics that could supplement existing identification methods. If successful, some of the measures can be achieved with inexpensive, new imaging systems. The internal anatomical structure of human fingers from grayscale US imaging offers a number of such identifiers. These metrics can be evaluated by trained observers, or possibly in the future by automated segmentation of image features and analysis thereof. Such techniques are investigated extensively in medical imaging as Computer Aided Diagnosis (CAD)[3,4] or tissue characterization.[5] A third, newer approach is to match the entire image or image volume to those of known individuals by maximizing a similarity measure(s) and setting threshold(s) for the degree of matching. This approach is often used in two-dimensional

(2D) images in the fields of machine vision and human face recognition[6] and has more recently been applied in the volumetric image sets acquired in medical imaging.[7,8]

These same and related techniques can be applied to color flow Doppler images of the finger vasculature, although the vessel flow is much more variable over time for a given individual, than are the structural shapes and sizes seen in grayscale imaging. Peripheral perfusion may be increased with exercise to allow more consistent imaging of a substantial portion of the vascular tree. Similarly, abnormally high perfusion or heart-rate might be employed as an indicator of individuals who are under high stress and perhaps not acting of their own free accord in conducting a legal or financial transaction.

2.2 Methods and materials

Studies were performed on individuals of both sexes and hand dominance, various races or ethnicities and age groups. A total of 20 volunteers were studied with mean age of 33 +/- 16 years, mean height of 5'7'' +/- 4" and mean weight of 146.5 +/- 24 lbs. We imaged the distal portions of three fingers - index, middle and ring - from both hands of all the subjects both before and after a physical exercise routine. As a result of technical complications and time constraints, 36 out of 40 pairs of images were collected. Due to computational overhead, 15 matched pairs and 12 unmatched pairs were randomly selected for image volume based registration (IVBaR) study from among the before and after exercise image pairs collected. For the human reader study, all of the 36 pairs were used. A set of 5 subjects were scanned separately for reader training purposes, and data from this set was not included in the analysis. The entire study was reviewed and approved by our Institutional Review Board (IRB) and informed consent was obtained from each participant.

Each hand of all volunteers was scanned using grayscale, power Doppler and time permitting, compound modes.[9] The scanning apparatus consisted of automated motorized two-axis translation stage to move the transducer holder as shown in Figure 2.1. This apparatus sits on top of a TPX (4-methylpentene-1 based polyolefin) plate of 2.5 mm thickness that separates it from the finger. The volunteer was seated comfortably to minimize any motion artifacts with his or her fingers pressed lightly against the paddle

after applying US gel for good coupling. The scans were performed by translating the probe in the elevational direction across the fingers by acquiring 2D images at a 0.4 mm interval. Translation speed was 2 mm/sec and the US system trigger rate was set at 5 Hz to assure completion of each frame. The 3D image size was about 500x200x125 pixels. The sonographic equipment used in this study was a commercially available GE Logiq-9 scanner (General Electric Medical Systems, Milwaukee, WI), modified to fire on input trigger pulses.

Figure 2.1: Experimental setup – apparatus to scan the finger and the TPX plate with the US scanner in the background. X and Y axes stepping motors for the transducer holders were on a frame attached to an upper compression paddle that helps stabilize the finger. Shown here, but not used in this study, are the vertical sliders and the bottom compression paddle.

The GE M12L array (General Electric Medical Systems, Milwaukee, WI) was used with a transmit carrier frequency of 14MHz for standard b-mode grayscale and compound imaging with seven angles (0°, +/-6°, +/-9° and +/-12°). For Doppler in color flow imaging, the transmit frequency was 6.6MHz and the pulse repetition frequency and wall filter settings were 800 and 45 Hz or 400 and 26 Hz, respectively, depending on flash artifacts. The Doppler study was cardiac-gated to allow acquisition of each image frame at the peak local systole.[10] With minimum color flow signal averaging, this gave peak color flow signal with no degradation of color spatial resolution in the elevation direction. The necessary triggering was provided by taking the waveform output from an

electrocardiogram (ECG) monitor (DINAMAP PRO 1000 ®, General Electric Medical Systems, Milwaukee, WI) via a 3.5mm socket and using an R-wave (the initial upward deflection of the QRS complex that corresponds to the depolarization of the ventricles in the ECG) threshold detector circuit with adjustable trigger level to produce a TTL pulse after the arrival of the R-wave. A time delay of 250 milliseconds after the R-wave was used before capturing a 2D Doppler image. The transducer is then translated to its new location and another time delay of 50 ms is then implemented to stabilize the scanning assembly and reduce the motion artifacts in the Doppler image. This process gets repeated for the length of the scan across the three fingers.

We studied two techniques to identify individuals by matching of the image sets.

Preliminary evaluation of semi-automatic identification (using MIAMI-Fuse© software) and

Reader study using visual matching of selected internal structures.

In a third study, we examined the effects of an exercise protocol on blood flow.

Each of these is described in detail below.

2.2.1 Semi-automatic identification using IVBaR

Registration software (described below) was used to align any two 3D image sets using 3D transformations (translation, rotation and scale) and the classical Shannon mutual information (MI) metric. This alignment should correct for any distortion due to repositioning of fingers. A minimal transform is required given that the subject fingers were placed in the scanning apparatus in a similar orientation each time, leading primarily to a simple translation transformation. Therefore, as will be seen later, the magnitude of rotational and scaling transformations needed in an attempt to align volume data sets provided a measure of match.

In the registration process, a voxel-by-voxel matching algorithm was used to maximize the mutual information between the two image volumes being registered. Ordered pairs of control points were manually placed on apparently identical structures that could be identified in both the 3D data sets in order to establish initial correspondence. The number of control points for the registration was at least 4 (with at

least 1 point out of plane) and the transformation used was 3D translation, rotation and scaling. The software MIAMI-Fuse© iteratively moves the control points in the homologous image and interpolates all the other pixels, tests for change in the mutual information using optimizer and then the homologous image volume is mapped onto its reference volume.[7,8] In Figure 2.2, a 2D image of central portion of middle finger is shown as checker-board (3x8) pattern of alternating reference image and its registered homologous image (marked as R, H respectively).

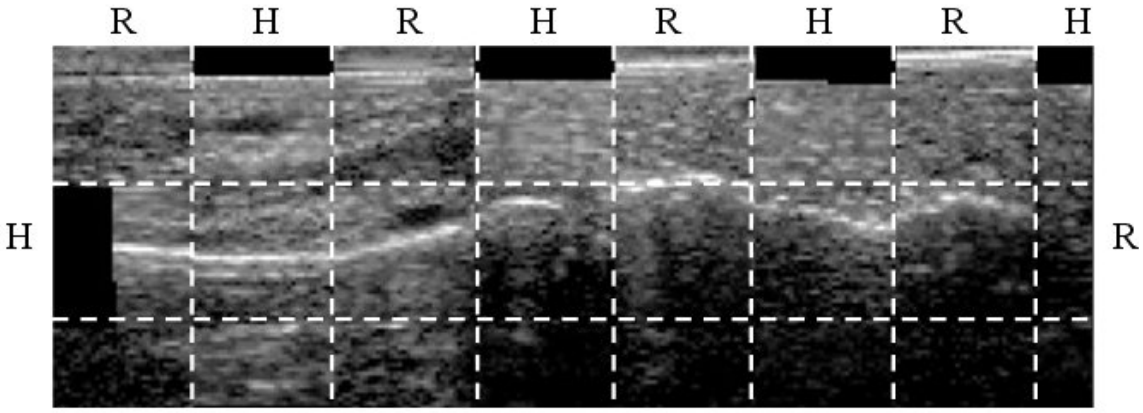

Figure 2.2: 2D composite image of the central portion of the middle finger shown in a 3x8 checkerboard pattern of rectangular blocks, alternatively from the reference image and its registered homologous image, marked on respective blocks as R and H. The continuity of the finger structures at different echo signal levels in some areas can be seen. Note that the bottom and right hand side of the image has been cropped as they extended beyond the region of interest.

2.2.2 Visual matching of images in Reader study

For the reader study, a group of individuals that included two expert musculoskeletal radiologists and two relative novices (physicists with backgrounds in ultrasound imaging who were trained for this study by the senior musculoskeletal radiologist) were selected. Readers performed 1-to-1 matching of pairs of 3D data sets using visualization and analysis software, ImageJ, developed at the National Institute of Health.[11] The readers went through the pair of stacks of 2D images to locate the corresponding structures. Matching of datasets was based on certain criteria defined by the senior radiologist and numerical scores were assigned according to a grading scale (described below). Some of the finger structures that were chosen by the senior radiologist for matching included the bone contour, volar plate thickness at the distal

interphalangeal joint, flexor tendon thickness, curvature and insertion point onto the bone, length of the distal phalange and the overall tissue appearance including regions with distinctive echogenicity and shadowing (see Figure 2.3). In the training session (where separate sets of data were used that had no bearing on the final outcome), 5 pairs of 3D US images were given to each reader individually who was asked to record similarities or dissimilarities in the finger anatomy. For an identical match, the structures in all three fingers have to lay in the same location in the two image volumes.

Once trained, readers performed the same matching procedure on all 36 pairs of datasets. These datasets were divided into two groups, 18 pairs from the same individual and another 18 pairs from different individuals. Each reader was offered the 36 pairs in a randomized fashion without the reader knowing that there were an equal number of matched pairs and mismatched pairs. The readers reviewed the image pairs across 2 or 3 sessions to limit fatigue. The results were recorded based on a 1-5 grading scale (5 – Highly likely match, 4 – Likely match, 3 – Inconclusive, 2 – Unlikely match and 1 - Highly unlikely match).

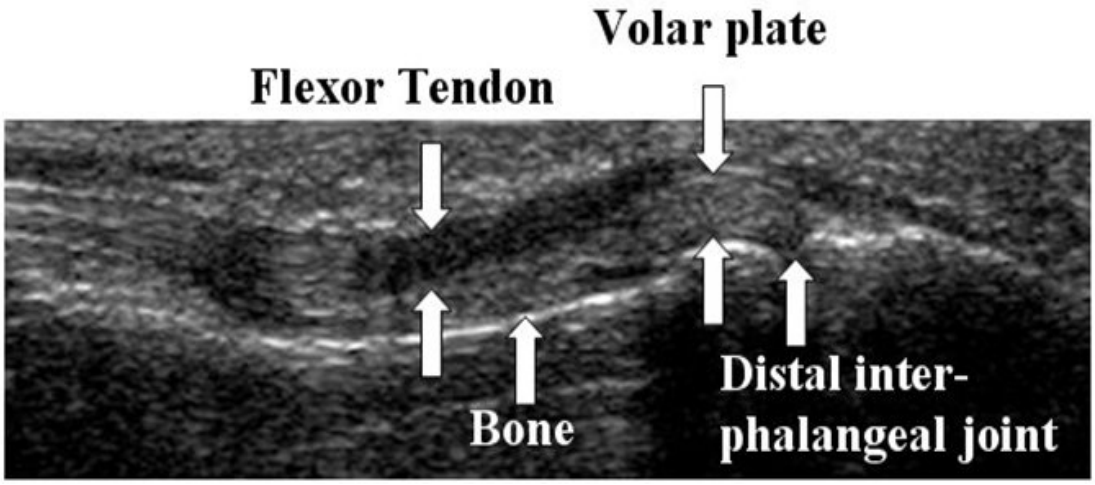

Figure 2.3: Primary internal finger structures employed in the visual matching study.

2.2.3 Cardiac-gated Doppler study

This study was performed to determine the possibility of using the US to evaluate the vascular patterns and record the variation in the blood flow with physical exercise as

a surrogate for stress level changes resulting in the blood flow modification. High levels of stress indicated by increase in the Doppler detected blood volume could mean the individual is not acting out of his or her own free accord. Potentially, the power Doppler data on finger could be used as a biometric identifier by matching the vascular pattern.

We examined the variation of detected blood volume (using Color Pixel Density – CPD) with exercise using Power Doppler US imaging of finger. The subject performed an exercise routine (jogging in place for 1-2 minutes) that elevates the heart-rate by approximately 50% above the resting heart-rate. This exercise was chosen at a low risk level to raise the heart-rate of the subjects so that the peripheral blood flow would increase among a large fraction of subjects studied. After elevation of the heart-rate by approximately 50%, there was a decrease in the heart-rate before the scan (approximately 1 minute time delay in re-coupling the subject for the US scan) and during the scan (2 minutes duration). Thirty-one Doppler scan image pairs were collected from either hand of the 20 individuals scanned due to technical difficulties and time constraints.

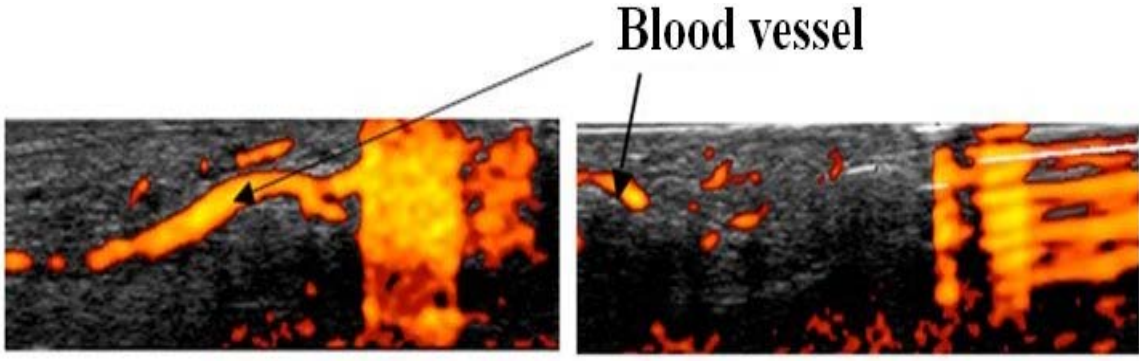

Figure 2.4: Power Doppler image of blood vessel in finger with flash artifact (left) and reverberation artifact (right).

Using US to image the vascular structure inside the finger gave another set of structures as a potential biometric for matching. In this study, we imaged the vascular pattern using power Doppler and measured various blood flow related quantities approximately. [12,13] This should not only indicate the vital status of an individual but also the person's physiologic status including anxiety level. Unlike the previous potential metrics, the blood flow varies substantially within an individual from time-to-time and also depends strongly on the US system capabilities and settings.

The power and color flow Doppler images can suffer from reverberations and other artificial motion artifacts, principally flash artifacts that must be eliminated for blood flow quantification as shown in Figure 2.4. The flash artifacts arise mainly due to

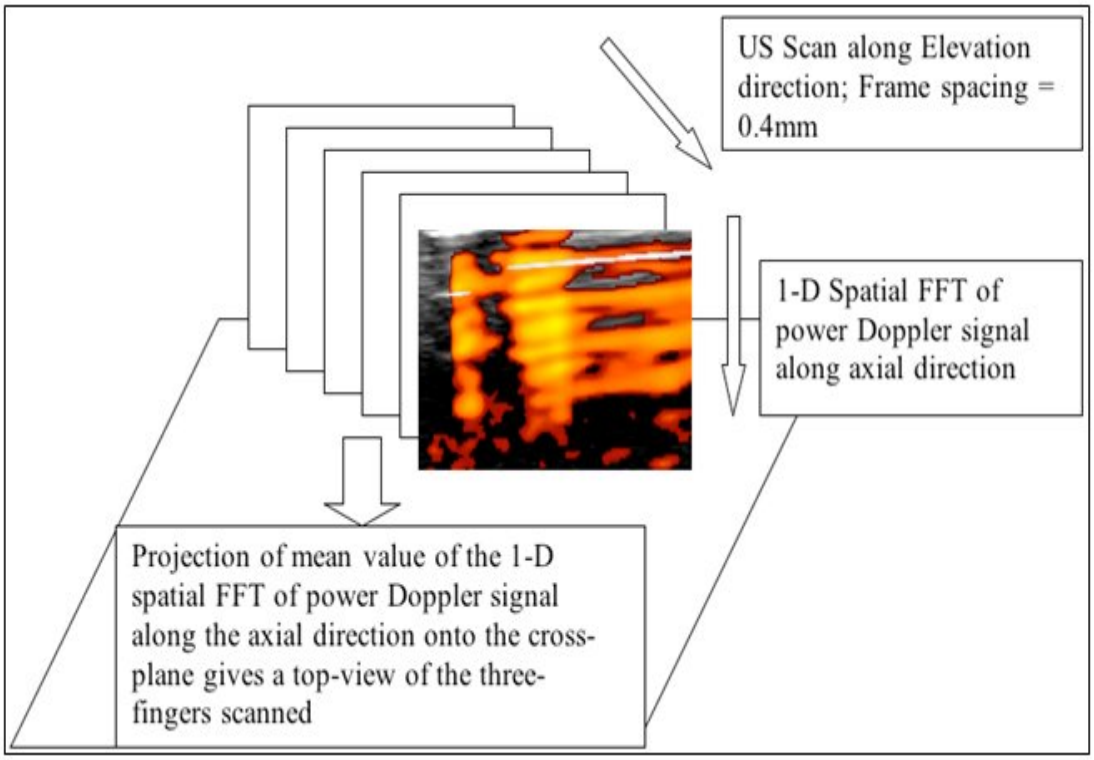

Figure 2.5: Schematic of projection of mean value of spatial 1-D FFT of power Doppler onto the cross-plane.

patient breathing motion during the scan. The reverberation artifact could be exacerbated by our use of the thin TPX membrane in between the scanner and the human tissue for convenience and positioning purposes (refer to Figure 2.1). Most of the artifacts seen in the power Doppler images had in common a certain spatial pattern of reverberations that repeats itself along the axial direction.

A boundary was traced manually to outline the three fingers and all the color data outside this outline were neglected. Taking a cross-section of the 3D grayscale image at mid-axial point did not give clear outer finger boundary, but the mean value of the spatial one-dimensional (1D) Fourier transform taken along the axial direction in the Doppler window of power Doppler data gave clear boundary. In Figure 2.5, a schematic outlining the calculation of spatial 1D Fourier transform of the Doppler data is shown. Figure 2.6

has the mean-value of spatial 1D Fourier transformed data in top-view with the finger outline marked for clarity.

The number of color pixels was summed within this finger boundary along the axial direction in each imaging plane. As flash and reverberation artifacts are expected to be of high amplitude and due to their repetitive nature along the axial direction, a threshold was set for the color pixel count in terms of percentage of total pixels along the axial direction. All color pixel values along the axial line that exceeded the threshold were neglected. This was evaluated for about 8 training sets of Doppler data in order to determine the threshold value. For power Doppler data shown in Figure 2.7(a), a threshold value of 25% removes artifacts as well as some amount of color data as shown in Figure 2.7(b), while 75% threshold allows almost all the artifacts to pass through as shown in Figure 2.7(d). A threshold value of 50% that blocked most of the artifacts

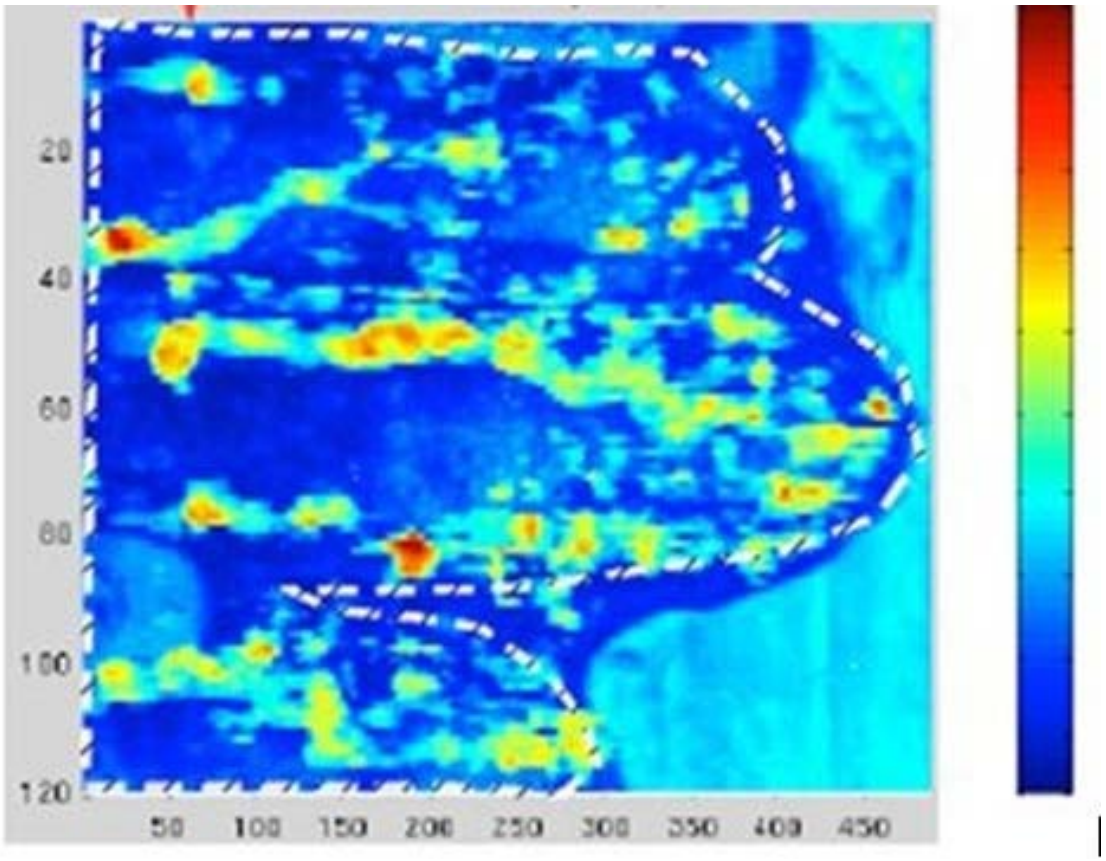

Figure 2.6: Mean value of the power of 1D spatial FFT of the power Doppler signal helps in identifying the finger boundary.

without cutting the blood flow as shown in Figure 2.7(c) was used for Doppler analysis of all the data. This threshold filter works for both the flash and reverberation artifact.

The color pixel density is obtained by summing the power Doppler signal in the post-threshold filtered 3D data and dividing by the volume of the selected ROI of finger. The color pixel density estimate acts as a measure of blood flow in the periphery and very high changes in it could be used as an indicator of high heart-rate or high stress. This could indicate that the individual may not be acting in free-will.

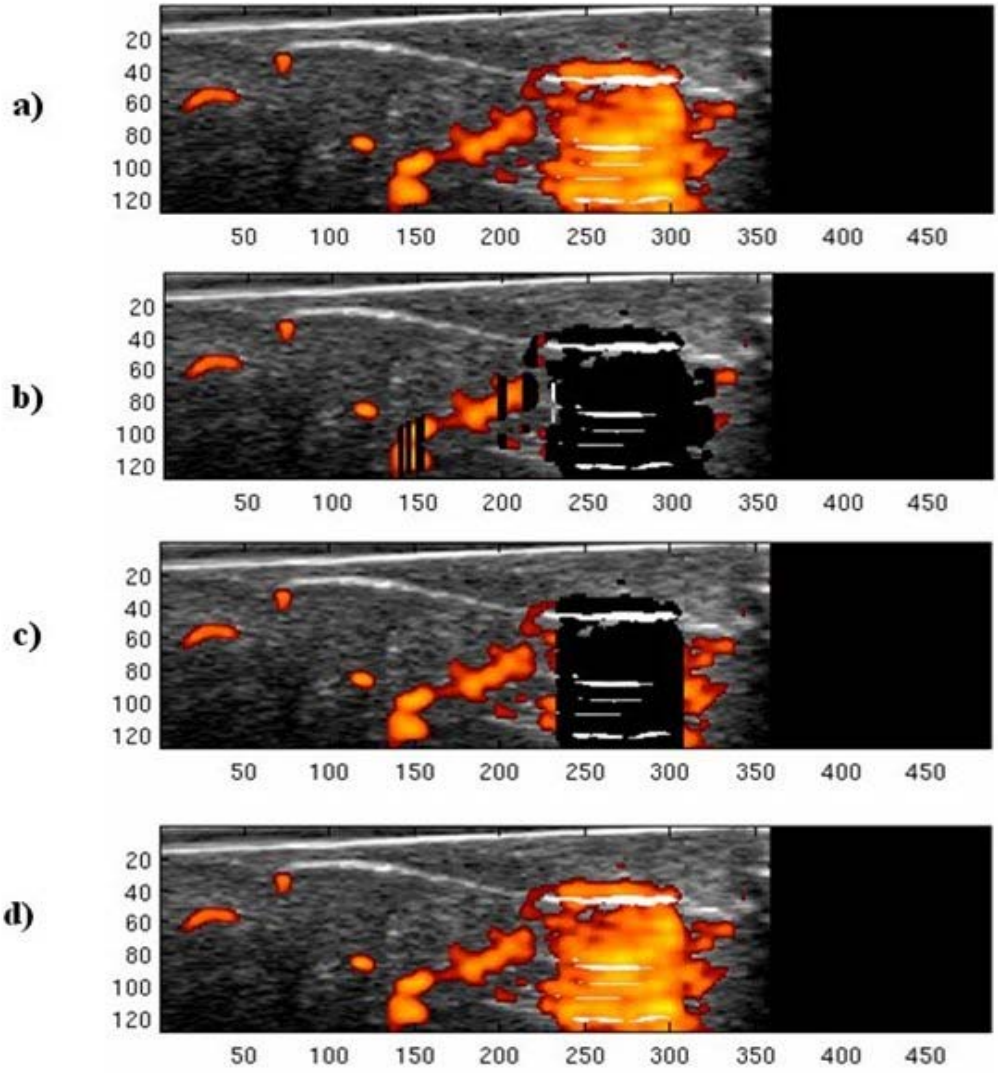

Figure 2.7: (a) Power Doppler image of finger that contains reverberation artifact (note that the region outside the finger outline was blacked out), b) after passing through an amplitude threshold filter of 25% that reduces both flash artifact and some amount of blood flow, c) after threshold filter of 50% that reduces flash artifact, and d) after threshold filter of 75% that allowed most of the artifacts to pass through. Notice that 50% threshold filter gives the best result.

2.3 Results

2.3.1 IVBaR on finger data

Upon registering pairs of image sets, a Rotational matrix (R) and Scaling matrix (S) were obtained that gives the amount of rotation and scaling along the 3 axes. The 3x3 R and S matrices were almost equal to the identity matrix with a small deviation for data from the same person while they differ from the identity matrix by a large margin for 2 different people. We defined the tolerance limit T, as the maximum allowed standard deviation of diagonal elements from unity and the non-diagonal elements from zero. For a successful match, the T value had to be a reasonable value for both the R&S matrices.

$$\sqrt{\sum_{i=1}^{3}(R_{ii}-1)^2} < T \;\&\; \sqrt{\sum_{i,j=1}^{3}(R_{ij})^2} < T, \; for\; i \neq j$$

$$\sqrt{\sum_{i=1}^{3}(S_{ii}-1)^2} < T \;\&\; \sqrt{\sum_{i,j=1}^{3}(S_{ij})^2} < T, \; for\; i \neq j$$

For T=0.1, the image-based registration met criteria for matching in all 15 out of 15 scans on the same individual and failed to meet those criteria in all of the 12 sets of finger scans from different subjects giving a sensitivity and specificity of 1.00 and 1.00, respectively. For a stricter tolerance level of T=0.05 on the same data sets, we obtained 14 right matches out of 15 scans of the same subject and 12 mismatches out of 12 scans from different subjects providing overall accuracy of 93% (sensitivity =0.93 and specificity =1.00) .

2.3.2 Reader Study

The results of reader study of all 36 image pairs from all four readers have been summarized in Figure 2.8 in the form of a scatter plot (a) and the corresponding Receiver Operator Characteristic (ROC) curve (b). The area under the ROC curve is high (A_z=0.96) signifying high accuracy for detecting matches and mismatches. [14,15]

The study by the two expert musculoskeletal radiologists yielded better results with A_z=1.00 than that by other readers. This A_z value is the same as for the previous image-based registration result with the tolerance limit T=0.1.

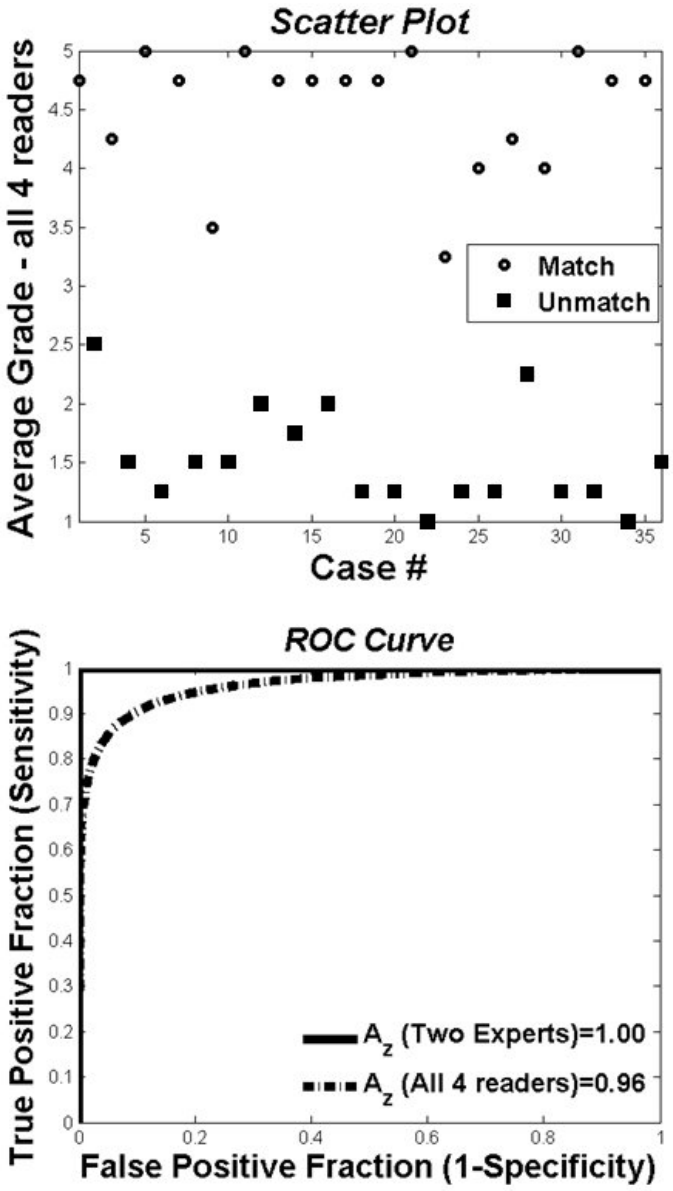

Figure 2.8: (a) Scatter plot of all 4 reader grades for matched with unmatched cases. (b) Corresponding receiver operating characteristic (ROC) curve shows the probability of matches with the probability of false alarm for 2 expert readers and all the 4 readers.

2.3.3 Doppler measurement of Physiologic changes

After making the correction for reverberation artifacts in the color pixel density of the power Doppler data on all subjects, the average fractional change in blood volume detected with exercise was +24% in all the 31 power Doppler scans that were collected. The average fractional change in blood volume detected was +43 % from among the remaining 19 Doppler scans, if the 5 scans where change was small and 9 scans where change was negative were excluded (reasons provided in Discussions & Conclusions). Figure 2.9 shows the percentage change in CPD with exercise.

2.4 Discussions and Conclusions

This finger study using 3D ultrasound illustrates the potential of using internal structures and vascularity of fingers and other biometrics for identification of individuals. The use of mutual information based image registration software for human identification

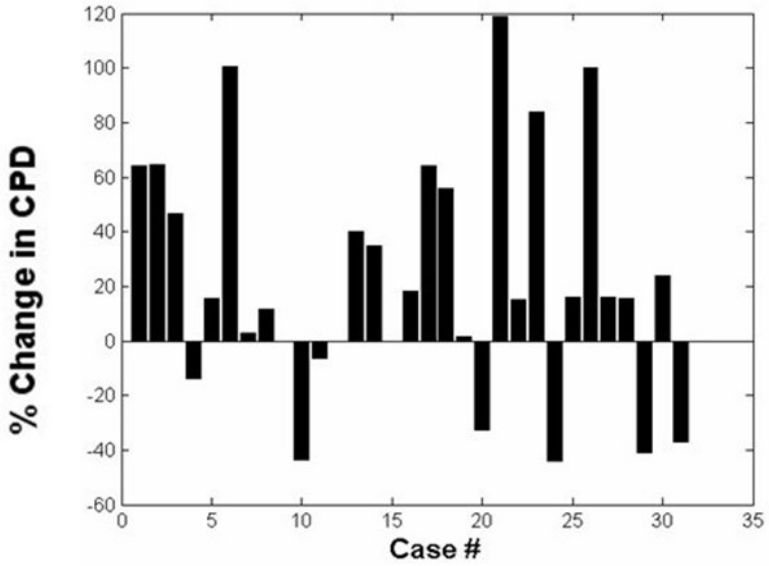

Figure 2.9: Percent change in color pixel density (CPD) with exercise in 31 cases.

was illustrated on grayscale US data. Future work should investigate the use of an overlap invariant measure like normalized mutual information and other matching functions as an absolute metric of match.[16] This might be obtained in conjunction with histogram equalization.

The human reader study accurately discriminated individuals from grayscale US images. The A_z value of 1.00 with two musculoskeletal radiologists and 0.96 with all four readers suggests that with modest confirming studies, these techniques could be used to supplement conventional techniques, particularly as very inexpensive US finger imaging is becoming possible. Subjective assessment of the volar plate, tendon thickness and attachment site, and bone contours enabled fingers from individuals to be matched. While anechoic joint fluid in the volar recess proximal to the volar plate may be present, this finding was not used for individual identification as joint effusions may change over time. Some of the structures investigated could change over time due to aging and osteoarthritis. Also some finger structures in people having joint disorders like rheumatoid arthritis would be more difficult to identify. The power Doppler imaging of human finger flow brought out the variation of the blood flow in an individual with time and stress. These potential variations must be controlled or accommodated in use of the blood flow in the finger as a supplemental biometric. Furthermore, such measurements were dependent on the US system capabilities and settings. Some of the challenges are addressed below.

2.4.1 Reasons for decrease in blood flow with exercise in some cases

Despite the short exercise routine, 5 out of 31 power Doppler scans detected a very low volume of blood flow. The blood flow could not be distinguished from the noise level and hence were neglected from this following analysis. The mean time required for repositioning from the end of exercise to the start of the Doppler US scan was about 1 minute during which the heart-rate and blood pressure fell by various amounts. Care was required to minimize this interval in order to control this source of error.

An important reason for decrease in the blood flow could be error in determining the Pulse Transit Time (PTT), i.e. the time interval for the detectable blood flow to peak at the finger after the R-wave in the ECG signal. This made us drop 7 cases where the color pixel density change was negative. With physical stress, anxiety, body temperature, metabolism etc, there is a shift in an individual's PTT to limbs.[17,18] As we performed cardiac-gated Doppler measurements at a fixed PTT (250 milliseconds) to reduce the

exam time, considerable error in timing the external trigger to the actual peak pulse arrival time might have resulted.[19] A better approach now available on some commercial ultrasound scanners is the color peak detect mode, which could be set to record the highest Doppler signal power over a cardiac cycle.

A pilot study was conducted to measure the variation of PTT on both left and right hands with changes in heart-rate caused by physical exercise and Figure 2.10 presents the results. The exercise routine used here (jogging up the stairs for 4 minutes) was harder than the one used for the finger study, but it highlights the fact that PTT changes considerably in an individual with physical exercise. The mean PTT in the middle and index fingers in the right and left hands of the volunteer changed from 246 to 189 milliseconds in this study.

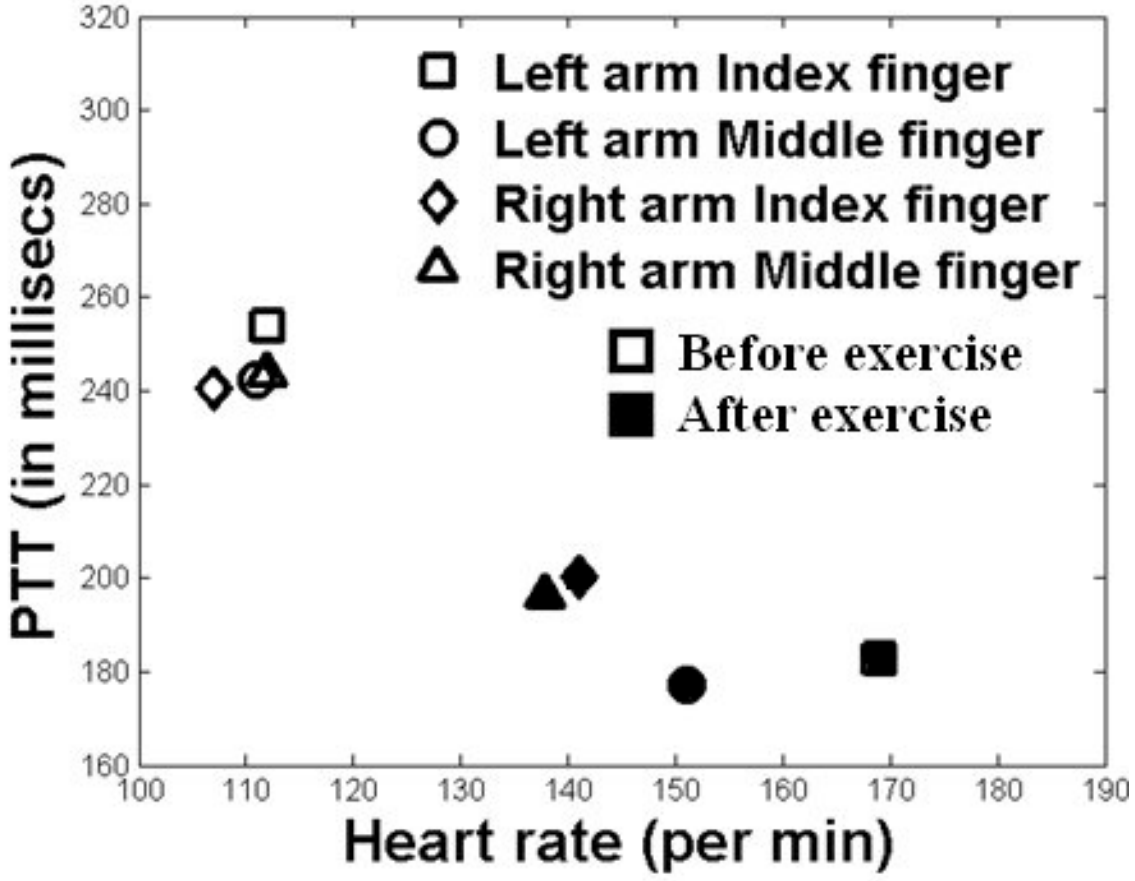

Figure 2.10: Variation of Pulse Transit Time (PTT) at finger (in milliseconds) with heart-rate (per minute) of a volunteer on the index and middle finger on the left and right hands.

In conclusion, 3D US scanning of the finger offer a novel biometric for human identification and basic physiologic status. This study illustrated identification of individuals by matching of their finger scans taken at different times when compared with scans of other individuals. This matching was accomplished by an objective, semi-automated algorithm based on the mutual information metric and by a human reader visual study. More development is required to make such imaging a reliable, high speed tool for detecting an individual from among millions. The technique is close to utility in some applications with reasonable assurance that an individual is the one in question, such as in high value cell phone security, particularly as an adjunct to fingerprint analysis that can be misinterpreted easily. The color Doppler study highlights issues with blood flow variation in an individual that need to be addressed for using blood flow as a potential biometric marker.

2.5 Acknowledgements

I would like to thank Drs. Jon A Jacobson, Michel De Maeseneer and Zhi Yang for serving as readers. I would also like to thank Timothy D Johnson for discussions on statistics which aided this work. This work was supported in part by NIH grants PO1 CA87634, R01 CA91713 and by NIST Cooperative Agreement No. 2001-00-4392 through CrossMatch Technologies Inc.

2.6 References

1 S Pankanti, S Prabhakar, AK Jain, “On the Individuality of fingerprints,” Proc. IEEE Computer Society Conf. Computer Vision and Pattern Recognition 1:805–812, 2001.

2 AK Jain, L Hong, S Pankanti, “An identity-authentication system using fingerprints,” Proc. IEEE 85(9): 1365–1388, 1997.

3 ML Giger, H Al-Hallaq, Z Huo, C Moran, DE Wolverton, CW Chan, W Zhong, “Computerized analysis of lesions in US images of the breast,” Academic Radiology 6(11): 665–674, 1999.

4 B Sahiner, HP Chan, MA Roubidoux, MA Helvie, LM Hadjiiski, A Ramachandran, C Paramagul, GL LeCarpentier, A Nees, C Blane “Computerized characterization of breast masses on three-dimensional ultrasound volumes,” Med. Phys. 31:744–754, 2004.

5 RM Golub, RE Parsons, B Sigel, EJ Feleppa, J Justin, HA Zaren, M Rorke, J Sokil-Melgar, H Kimitsuki, “Differentiation of Breast Tumors by Ultrasonic Tissue Characterization,” J Ultras. Med. 1993; 12(10): 601–608.

6 H Neemuchwala, AO Hero, S Zabuawala, PL Carson, “Image registration methods in high-dimensional space,” Intl J Imaging Sys Tech 16(5):130–145, 2006.

7 CR Meyer, JL Boes, B Kim, PH Bland, KR Zasadny, PV Kison, K Koral, KA Frey, RL Wahl, “Demonstration of accuracy and clinical versatility of mutual information for automatic multimodality image fusion using affine and thin-plate spline warped geometric deformations,” Med Image Anal 1(3):195–206, 1997.

8 H Park, PH Bland, KK Brock, CR Meyer, “Adaptive registration using local information measures,” Med Image Analysis 8:465–473, 2004.

9 R Entrekin, P Jackson, JR Jago, BA Porter, “Real time spatial compound imaging in breast ultrasound: technology and early clinical experience,” Medica Mundi 43(3): 35–43, 1999.

10 PT Bhatti, GL LeCarpentier, MA Roubidoux, JB Fowlkes, MA Helvie, PL Carson, “Discrimination of sonographically detected breast masses using frequency shift color Doppler imaging in combination with age and gray scale criteria,” J Ultras. Med 20(4): 343–350, 2001.

11 WS Rasband, ImageJ, U.S. National Institutes of Health, Bethesda, MD, USA. http://rsb.info.nih.gov/ij/, 1997–2007. Date accessed: Sep 1, 2007.

12 PL Carson, X Li, J Pallister, “Approximate Quantification of Detected Fractional Blood Volume in the Breast by 3D Color Flow and Doppler Signal Amplitude Imaging,” Proc. of IEEE Int’l Ultrasonic Symposium Cat. #93CH3301-9:1023–1026, 1993.

13 JM Rubin, RS Adler, JB Fowlkes, S Spratt, JE Pallister, JF Chen, PL Carson, “Fractional Moving Blood Volume Estimation Using Doppler Power Imaging,” Radiology 197(1):183–190, 1995.

14 JA Hanley, BJ McNeil, “The meaning and use of the area under a Receiver Operating Characteristic curve,” Radiology 143: 29–36, 1982.

15 JA Hanley, BJ McNeil, “A method for comparing the areas under the Receiver Operating Characteristic cases derived from the same cases,” Radiology 148:839–843, 1983.

16 C Studholme, DJG Hill, DJ Hawkes, “An overlap invariant entropy measure of 3D medical image alignment,” Pattern Recognition 32:71–86, 1999.

17 J Furedy, A Szabo, F Peronnet, “Effects of psychological challengers on heart rate, T-wave amplitude and pulse-transit time,” Intl. J Psychophysiology 22:173–183, 1996.

18 JE Naschitz, R Itzhak, “Assessment of cardiovascular reactivity by fractal and recurrence quantification analysis of heart-rate and pulse transit time,” J Human Hypertension 17:111–118, 2003.

19 M Nitzan, B Khanokh, Y Slovik, “The difference in pulse transit time to the toe and finger measured by photo-plethysmography,” Physiological Measurement 23:85–93, 2002.

CHAPTER 3 SPATIAL REGISTRATION OF TEMPORALLY SEPARATED WHOLE BREAST 3D ULTRASOUND IMAGES

3.1 Introduction

Mammography is the accepted technique for breast screening aimed at detecting cancer at early stages. However, exposure to radiation, low positive predictive values and low sensitivity in dense breasts are concerns.[1, 2, 3] Contrast enhanced magnetic resonance imaging (MRI) is very useful, but it would be helpful to have non invasive, less expensive and time-consuming procedures.[4] Physical palpation is used to study the breast qualitatively for size, shape, firmness or location of mass. Despite the utility of clinical breast examination or palpation, it has been shown to be dependent on the examiner, interpreter and other factors that could be relatively inaccurate.[5] US is used frequently to evaluate breast masses (mainly mammographic soft tissue densities as opposed to focal and clustered calcifications) as well as changes in the breast structure.[6, 7] US has been mainly useful in its ability to differentiate simple cysts from solid masses[8, 9, 10] notably in mammographically dense breasts.[11, 12, 13, 14] Breast US scans are currently performed free hand by radiologists and technologists using US systems providing real time two dimensional (2D) images with relatively small field of view. Conventional US imaging is performed freehand in a different geometry than mammography that can make it difficult to correlate lesions in the two modalities. Studies have shown that at least 10% of the time, lesions found in the US images does not correspond with those in the mammograms.[15]

Currently, for tracking response to breast cancer therapy, qualitative and coarse quantitative changes are detected using palpation as the primary method. This is

supplemented in some cases by visual comparison of images during the course of therapy. Even more accuracy and precision is required for treatment trials where early prediction of response is attempted. In patients undergoing therapy for malignant tumors, it can be vitally important to gauge the effectiveness of the therapy when there are questions regarding appropriate follow-up therapy. According to a study on change in tumor volume measured using MRI, volume change estimation could possibly aid in evaluating response to chemotherapy and may act as a detection and diagnostic tool in the future. [16] As for US tracking, breast tumor boundaries have been typically poorly defined in image volumes after the onset of chemo or radiation therapy.[17] A small study on chemotherapy showed that it may induce inflammatory or fibrotic changes in the tumor and standard methods of assessing tumor size are only moderately successful.[18, 19]

Spatial registration that aligns temporally separated image volumes should aid in visual and automated detection and characterization of changes in volumetric images that are now available in several modalities. [20, 21] We suggest that 3D US registration of periodic screening studies may become highly useful in detecting and discriminating malignant changes. Manual registration for evaluation of large sets of image volumes may be extremely time-consuming and subject to substantial user variability depending on skill, patience and experience. Automated or semi-automated registration of two image volumes taken at different times was performed primarily to spatially align the two in the same coordinate system in order to allow better comparison and visualization of changes.[22] This is becoming an effective tool in diagnostics, therapy planning, image-guided surgery and treatment assessment.[23, 24, 25] Registration helps in correcting for slight changes in scan positioning during subsequent studies of the patient and resolves ambiguities in positioning and actual location of some of the structures. This may help in detecting subtle changes that may go unnoticed in unregistered scans.

There are many different techniques to compute the geometric transformations that map the coordinates of corresponding points between two image volumes. The transformation model can be a simple rotate-translate model that is applicable for a rigid site, e.g. human skull. A more general linear transform is the affine transform that includes rotations, translations, shearing and scaling. There are many situations where affine registration techniques are not sufficient to achieve alignment of anatomy. Hence,

a non-rigid deformable model is needed to accurately represent the transformation. Some of the commonly used non-rigid models are based on parameterization, including general diffeomorphism (e.g. fluid model), spline based methods (e.g. B-spline and thin plate spline (TPS)), Fourier based methods (e.g. Statistical parametric mapping) etc.

In the 'Demons' algorithm based on fluid model, the image entities or 'demons' push according to local characteristics of the image in a way similar to that proposed by Maxwell in solving for Gibbs free energy in thermodynamics.[26] This algorithm, which is remarkably fast, uses the optical flow equation to determine the 'demons' force at each pixel. When the gradient on the reference image is low, the model may not be efficient. The strength of the force that gets adjusted in the iterative process has been refined in subsequent studies.[27, 28] Some of the salient features of this model include the use of gradient information from a moving image in order to deform it to a static reference image. At the same time, good understanding of the regularization is critical to obtain a useful deformation field.

B-splines are piecewise polynomial of order *n* with compact support and continuous $(n-1)^{th}$ derivative. Due to compact local support, B-splines can be used to model localized deformations and have advantages of reduced complexity and low computation time.[29] The displacement at any point is given by the weighted sum of basis functions defined over a limited region. The mapping function in a B-spline based transformation is modeled based on translations of a regularly spaced grid of control points. In another spline based model - TPS, the transformation parameters are determined by minimizing the bending energy of a thin, hypothetical 3D metal plate with edges clamped at infinity.[30] The spline coefficients are calculated by the least squares method. In the TPS based deformation model, control points are iteratively moved to maximize the similarity metric between the two image volumes. TPS can be used even if the control points are irregularly spaced, and changing the position of one control point changes the deformation of the overall image. Using more control points reduces this influence but leads to higher computation cost.[31, 32] Selection of a few control points results in a rough match whereas selection of a larger number of control points result in large local oscillations in the deformation model. Both these spline based methods suffer because the ideal number of spline parameters (number of control points) is an unknown.

In order to maintain the focus of this preliminary study on clinical application of image registration, we have applied a single non-rigid deformation model based on TPS.

Earlier registration work was applied to small volumes of tissue usually containing a central mass such as a tumor. In this study, we aim to evaluate the accuracy of a more difficult problem, image-based spatial registration of compressed, nearly whole breast image volumes. Our 3D US system has been augmented with a motorized transducer carriage above a special compression plate developed in order to improve the coverage over the whole breast.[33, 34, 35, 36, 37, 38]

US imaging, along with other coherent imaging systems, suffers from speckle noise caused by interference effects between overlapping echoes from randomly distributed structure scatterers that are too small to be resolved. Speckle degrades the signal to noise ratio of the image and this could lead to reduced performance in registration compared with most other imaging modalities.[22] Registration of whole breast US studies to each other is somewhat difficult due to noisy images, artifacts, heterogeneity and high mobility of breast structures under mammographic-style compression. Hence, some of the US studies were performed in the same session with patient repositioning to assess image registration accuracy under nearly ideal conditions. The accuracy was estimated by evaluation of displacement of visually selected corresponding points (referred as “fiducials”) in the two image volumes by registration. For increased accuracy in tumor change evaluation, three studies on each malignant tumor case (prior, during and after chemotherapy) were performed.

When the registration is based primarily on the mass or on tissue structures surrounding the mass, a non-rigid transform could map the boundaries in the reference image to the boundaries in the homologous image.[39, 40] This transform has information about the size change and could be used for estimation of volume change. Using IVBaR and the radiologist identified tumor region in the pre-chemotherapy image volume, we have devised a new method of automated estimation of tumor volume.

Malignant masses have often been associated with increased vasculature in comparison to benign lesions.[41, 42] Studies in the past have shown that the efficacy of US for discriminating breast masses is improved by adding the information from color flow Doppler imaging to the B-mode grayscale information than just from B-mode

imaging. [43, 44] In this study, color flow Doppler scans were performed at each time point to not only quantify the blood flow in and around the lesion, [45] but also to validate IVBaR of the 3D grayscale information in these color flow image volumes by the resulting alignment of the Doppler-imaged blood vessels that were not used in the registration. Previous studies have used information from major blood vessels in Doppler US for fusing with MRI or Computed Tomography (CT) images.[46, 47]

The aims were to perform and assess the following:

IVBaR of automated US in the mammographic geometry: IVBaR under minimal change of ABU scans was performed before and after repositioning for assessment of registration accuracy.

Tumor volume change estimation: Estimation of chemotherapy induced tumor volume change was performed using IVBaR and validated.

Independent validation using Doppler imaging: Color flow Doppler US imaging was performed on selected subjects with sufficient blood flow to provide an independent measure of the accuracy of B-mode image registration.

3.2 Methods and Materials

Human studies were conducted at the University of Michigan Comprehensive Cancer Center. An Internal Review Board approved all procedures and informed consents were obtained from patients.

3.2.1 Patient Distribution

Subjects selected for this study included 10 women who were scheduled to undergo chemotherapy based on the previously confirmed presence of cancer and 14 women with suspicious/unknown masses who were scheduled for biopsy with mean age of 46±9 years. The mean time difference between pre- and post-chemotherapy scans was 115±14 days. Amongst 10 tumor cases, only 7 were chosen for tumor volume estimation based on tumor visibility as discussed in section II.F. The Doppler study was performed on 8 patients (5 scheduled for biopsy of a suspicious mass and 3 scheduled for

chemotherapy) who had detectable blood flow (see section II.G) with mean age of 49±8 years. A subset of patients were repositioned and rescanned for the registration accuracy tests.

3.2.2 Setup

All US scans were performed with a Logiq-9 US system (General Electric Healthcare, Waukesha, WI), modified to acquire individual B-mode or color Doppler images on input trigger pulses. Images were obtained using a 10L linear array transducer at 10MHz central frequency for grayscale imaging in most cases and in some cases with an M12L transducer at the same frequency using a maximum number of 8 transmit focal zones. Doppler imaging was performed at a central frequency of 6.6 MHz (pulse repetition frequency in the range of 0.6–0.9 kHz depending on flash artifacts).

Each patient scanning session began with a radiologist performing a 3D freehand US scan across the breast to confirm the region of interest and to look for blood flow. Volumetric US data were obtained and stored in the cine loop buffer of the US system by manually sweeping the US transducer across the volume of interest. The patient was then positioned as in Figure 3.1, with her breast between the top compression paddle, a TPX plate (poly-methyl pentene), and the bottom supporting plate. A biocompatible mild adhesive spray (Got2b glued spiking spray, Advanced Research Laboratories, Costa Mesa, CA) stabilized the compressed breast while providing reasonable acoustic coupling between the top plate and breast. The patient was seated comfortably throughout the scan to minimize motion artifacts.

The automated whole breast US scanning assembly consisted of a two-axis US transducer positioning system above the top compression plate, as in Figure 3.1. The US transducer was placed in a holder that was attached to computer-controlled positioning system. Spring-loaded vertical motion of the holder allowed the transducer to follow the slightly curved surface of the compression plate. All ABU scans were performed in the cranial-caudal (CC) position with prior assessment of location of the mass and information including pathology and conventional mammograms. A 3D grayscale image volume was obtained by translating the transducer in the elevational direction by 12 to 13

cm. Proper coupling between the transducer and the TPX plate was achieved with water for CC views and coupling gel for others. In order to reduce the air-gap between the breast periphery and the plate, a viscous, bubble-free US gel (LithoClear, Sonotech Inc., Bellingham, WA) was applied. The 3D US volumes were acquired as a parallel stack of 2D US images taken with elevation separation of 0.4 mm and axial/lateral voxel dimension of 0.1 to 0.15 mm depending on the depth of imaging. Imaging a test object using the M12L transducer through the TPX plate in order to determine the line spread function (LSF) revealed that the elevational, lateral and axial full width half maximum (FWHM) resolutions were approximately 1.0, 0.4 and 0.2 mm.[35] These methods and the effect of using a compression plate for US scanning were addressed.[36] The US system trigger rate was set at 5Hz resulting in a transducer translation rate of 2mm/sec. One to three parallel 39 mm wide automated B-mode US sweeps were performed as needed to cover the entire breast, depending on its shape and size under compression and to the extent allowed by the achieved acoustic coupling. Sweeps overlapped by 1 cm. Other hardware and software interfaces developed to perform automated scanning, which included computer triggering of the Logiq-9 system for data acquisition, were discussed elsewhere.[33]

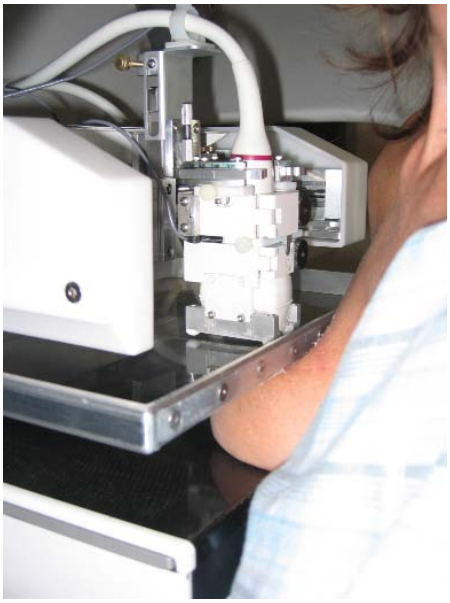

Figure 3.1: View of the breast under partial compression by mammography-style compression plates with the patient slightly rotated away in order to show the apparatus. Here, the transducer holder was spring-loaded in a frame attached to the paddle and moves above the compression plate with the transducer following the paddle surface. Notice that the transducer holder can be rotated about a vertical axis for scans at angles not parallel to the chest wall.

The region of interest (ROI) was identified in the automated grayscale scans to guide a cardiac-gated Doppler scan that was performed over the ROI in a single sweep of the US transducer. This study was performed on patients with cancers or with undiagnosed suspicious masses having sufficient blood flow to be visible in the freehand US Doppler scan performed by the radiologist. The Logiq-9 image acquisition was triggered at the peak of the R-wave in the ECG to allow blood flow to peak at the breast after an appropriate time delay of 165 milliseconds, based on a pilot study of four healthy volunteers. After that the transducer was translated to its next location by the computer-controlled positioning system. A 50 ms time delay was then implemented to let the transducer positioning assembly stabilize and to minimize flash artifacts in the Doppler image before arming the ECG trigger. The process was then repeated for the length of the scan. A Doppler image volume with color information covered approximately 4x4x4 cm^3.

In order to evaluate reproducibility, a subset of patients were taken out of compression and given a break, and all the above positioning and scans were repeated within 30 minutes in the same session.

3.2.3 Image acquisition

A total of 19 3D ABU grayscale scan pairs were acquired in 10 women consisting of 9 pre- and mid-chemotherapy scan pairs, 5 mid- and post-chemotherapy scan pairs and 5 pre- and post-chemotherapy scan pairs. For reproducibility evaluation of image volume by registration in the simplest relevant cases, repositioning and recompressing the breast in the same session within 30 minutes, 10 pairs of grayscale ABU volumes were acquired.

In addition, to evaluate the effects of compression on vascularity measures, automated 3D cardiac-gated Doppler US scans were collected at multiple compressions of the breast in the same session in selected subjects with detectable blood flow (3 patients undergoing chemotherapy and 5 with a suspicious/unknown mass). The initial Doppler scan was taken at near mammographic compression and the subsequent scans were taken either at the same, relaxed or additional compression as acceptable to the patient. Each Doppler acquisition took less than 4 minutes.

3.2.4 Image pre-processing

After image acquisition along the slightly curved surface of the compression plate, image data from each sweep was aligned rapidly with that of its neighboring sweep using a 1D cross-correlation technique along the elevation direction in the overlap region of 100x389x383 voxels or about 10x39x153 mm^3. This helped in obtaining a self-consistent, single image volume covering most of the breast, typically of size 700x389x383 voxels or about 70x39x153 mm^3 for a typical two transducer sweeps. Due to the instability in the transducer holder and stepping motion, a mean misalignment of 1±0.8 mm was detected along the elevation direction between two adjacent sweeps and corrected in all 19 ABU image volume pairs.

Doppler image volumes were acquired by a single sweep of the US transducer over the ROI surrounding the tumor. Every automated 3D color flow image volume was converted into two processed image volumes before registration. First, the grayscale portion of the color flow image was retained while the color portion was zeroed out (referred to as Doppler image G or DI-G). Secondly, in every automated 3D color flow image volume, the color portion of each Doppler image was altered to a uniform color while the grayscale portion was zeroed out (referred to as Doppler image C or DI-C). The color portion of the reference Doppler volume set was replaced by uniform red color and that of the final volume set by uniform green. The utility for these two image types is described in section 3.2.7.

3.2.5 IVBaR of Automated US in mammography geometry

Registration was performed semi-automatically and with limited user interaction using the well-studied MIAMI Fuse© software developed at the University of Michigan. This algorithm maximizes a similarity measure, the classical Shannon mutual information (MI).[22, 48] Registration of two US image volumes depends on the available MI in the image volumes, which in turn depends on the amount of true structural information such as specular reflectors and changes in volumetric scatterers as well as shadowing, other artifacts and deformation of local tissue.

As a first step of registration, a 3D full-affine transformation was performed to take into account changes that are global in nature between the two image volumes including translation, rotation, scaling, and shear.[49, 50] Ordered pairs of N_c control points were manually selected at presumed corresponding locations in the two 3D volumes to establish initial correspondence. In the full-affine transform, a mean N_c of 4 pairs of points (not all in the same plane) was selected. The algorithm utilizes the Nelder/Mead downhill simplex optimization by iteratively moving the positions of the control points in the homologous image volume with an affine transform. All other voxels were moved and interpolated with the same transform until the MI was maximized.

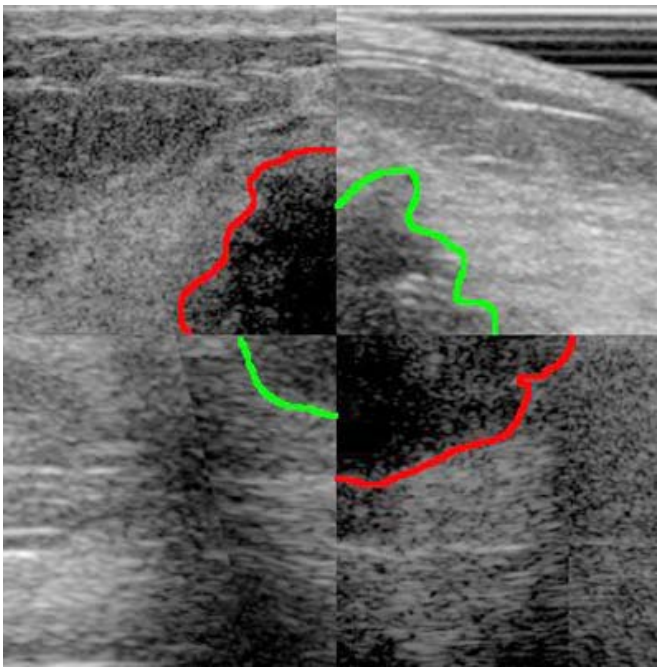

Figure 3.2: Checkerboard (2x2) pattern of a registered pair of a pre-chemotherapy image (top left & bottom right squares) and a post-chemotherapy image (top right & bottom left squares). The hypo-echoic boundaries are drawn for convenience (red for pre-chemotherapy image and green for post-chemotherapy image). The mean registration error was 8.4±2.6 mm. It can be seen that the tumor had shrunk in size with therapy from spatial alignment of these images by registration. Other reasons could include changes due to differences in compression forces, thickness as well as differences in positioning within range of normal mammographic repositioning.

The non-rigid TPS-based transformation was then performed in order to accommodate elastic deformations of the breast and local changes in the tissues. This needed at least five control points in each 3D image volume pair. The locations of control points in the homologous image volume were moved incrementally by the algorithm and the locations of other voxels were interpolated using TPS. The algorithm maximizes MI

as above.[51, 52, 53] The TPS mapping has 3*Nc* degrees of freedom and was globally defined everywhere. The computational time was dependent on the size of the reference image volume and *Nc*. In non-rigid transforms, additional set(s) of control point pairs were manually selected in the grayscale U.S. image volume, here with mean *Nc* of 15. In performing the transformations in the sequence of rigid, affine followed by non-rigid, the data volumes were down-sampled in a coarse-to-fine approach, referred to as a multiresolution optimization scheme. This strategy assured a smooth global to local deformation and also that the control points did not fall into local minima, keeping the registration process efficient, robust and less time consuming.[54, 55]

As an example, in Figure 3.2, a 2D composite image consisting of registered pair of pre- and post-chemotherapy images is shown with a rough hypoechoic boundary. The larger tumor in the quadrants from the pretreatment exam shows that the tumor had reduced in size with therapy. Registration aligned the two image sets in the same coordinate system, thus making comparisons easier.

Manual selection of fiducial points was a time-consuming procedure that was also prone to inaccuracy. In the absence of a "gold standard", this constituted a direct way to estimate registration error *in vivo* without exterior or interior placed landmarks that were impractical in breast imaging. In this preliminary study, a senior radiologist performed the manual selection of fiducials as identical, point-defining structures including branching ducts, vessels, glandular and connective tissue patterns in the unregistered reference and homologous image volumes. The registration transformation applied to this set of fiducials in the reference image volume gave the location of these reference fiducials in the homologous data space. The mean Euclidean distance between these transformed fiducial points and their corresponding points selected earlier in the homologous image volume gave the mean registration error (MRE). Note that the MRE was dependent on the radiologist's positioning and distribution of the fiducials in both the image volumes and hence was dependent on the radiologist's skill and patience. Our estimation of MRE includes the image registration error as well as error in hand-picking fiducials.

Also measured was the mean pixel displacement (MPD), which was defined as the Euclidean displacement of every pixel in the US image volume due to registration

transformation. Note that this automated measure was not a measure of registration accuracy but overall motion of pixels due to transformation.

3.2.6 Automated estimation of the tumor volume in one exam from the previously segmented tumor using IVBaR in ABU image volumes

For automated estimation of tumor volume in the post-chemotherapy ABU image volumes, the tumor in the pre-chemotherapy image volume was hand-segmented by the radiologist using in-house segmentation software programmed in MatLab®. For validation purposes, the tumor volume in the post-chemotherapy image volume was also hand-segmented by the radiologist. Using IVBaR and the radiologist identified tumor region in the pre-chemotherapy scan, we designed a new method of automated estimation of tumor volume in subsequent studies as outlined below.

Typically, boundaries of breast tumors in US image volumes are even more poorly defined after the onset of chemotherapy.[19] An assumption in this study was that the only tissues to change in the chemotherapy were those of the tumor and the boundaries of the tumor. The automated estimation of tumor volume of the later scan involved these steps:

1. Pre-chemotherapy image volumes were registered with later scan (mid- or post-chemotherapy) image volume.
2. Radiologist hand-segmented the tumor region in both image volumes by setting intensity of tumor regions to zero (process of “masking”).
3. The transformation used in step 1 was applied to the pre-chemotherapy image volume in step 2 to obtain the automated tumor region in the image space of the later scan.
4. The automated tumor volume of later scan was obtained by summation of pixels in automated tumor region in step 3.
5. Radiologist’s estimation of the tumor volume of later scan was obtained by summation of manual segmentation of tumor region, which was then compared with that of step 4.

Shown in Figure 3.3 are 2D images from the transformed pre-chemotherapy tumor volume and the corresponding image from hand-segmented post-chemotherapy tumor volume. In this case, the volume estimate from the registration-based method was within 91% of the radiologist's measurement of tumor volume.

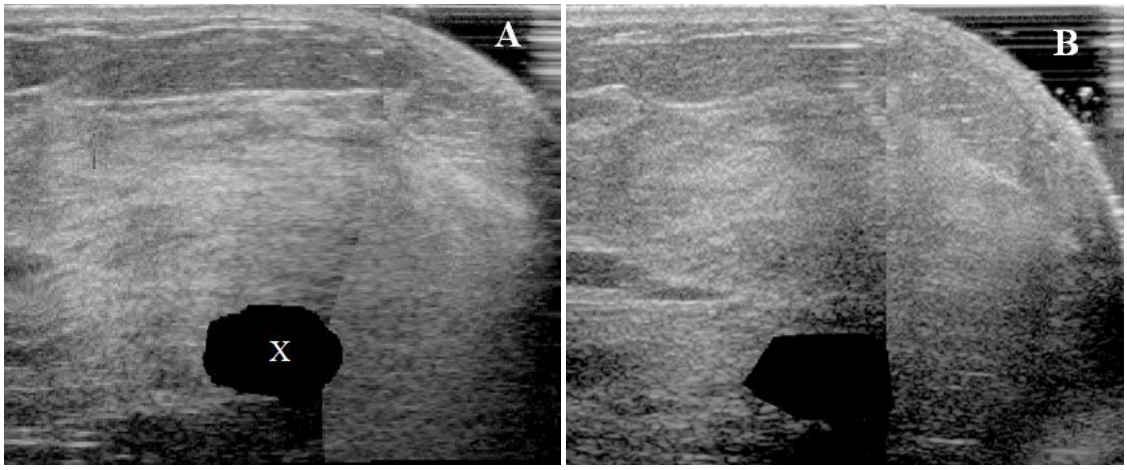

Figure 3.3: (a) Slice from pre-chemotherapy image volume mapped into the space of post-chemotherapy image volume. The blacked out region (marked as "X") was obtained by applying the transformation of the pre- to post-chemotherapy registration to the hand-segmented pre-chemotherapy tumor volume. (b) The corresponding slice in the hand-segmented post-chemotherapy image volume for validation.

3.2.7 Independent validation of IVBaR using Doppler imaging

In the 3D color flow Doppler image volume, summation of the number of color pixels gave a value which, ignoring attenuation effects, was related to the volume of relatively fast moving blood. As blood vessels were widely distributed throughout and hence reflect the deformations of the breast, the movement of blood vessels was used as a surrogate to the movement of muscle, fat tissue, glandular tissue, mammary glands, ducts and breast masses. Doppler reproducibility studies under similar breast compression and identical system settings were performed in the same session in order to study the overlap of blood vessels using image registration. Various color flow Doppler quantities were also estimated as mentioned in an earlier study.[45] Comparing the spatial overlap of color flow pixels between the Doppler image volume pairs before and after registration, 3 independent and automated measures for validation of B-mode registration were identified in the final aim of this study.

All US system settings were identical between studies on the same individual since Doppler signals are very sensitive to system settings. Color Doppler artifacts were removed and the overlap regions in corresponding color vessel segments in the two registered image volumes were identified and cropped. Three methods were identified for independent validation of B-mode image volume registration using the Doppler image volume:

a) Blood vessel overlap ratio in the region surrounding the mass

b) Automated separation of the centerlines of blood vessels and

c) Manual separation of radiologist selected landmarks

In method a), non-rigid registration of the two Doppler image volumes was performed. As the first of two steps in registering Doppler image volumes, the original grayscale portion of the Doppler image volume DI-G1 was registered to its later counterpart DI-G2. The resulting transformation was applied to the color-information only DI-C1 image volume, and the registered color image (DI-C) pair was displayed one on top of the other in the same coordinate system. This display shows in red the original DI-C1 image volume, in green the registered DI-C2 image volume, and in yellow the overlap region. In this cardiac-gated Doppler study, even with identical system settings as well as breast compression, there were differences in the region of blood vessel imaged in US depending on the time-varying physiological conditions of the subject.

As one automated, relative measure of registration accuracy, the Blood Vessel Overlap (BVO) was defined as the Doppler intersect volume in yellow divided by the smaller of the two Doppler volumes that is red plus yellow or green plus yellow. This was chosen to give a scale of 0 to 1 in all cases and BVO of 0.5 when the segments were of the same size and overlap by half. This measure was evaluated for 8 patients at either equal to or at ~±10% of equal compression levels as measured by plate separation. In addition, changes in blood volume were evaluated at varying compression levels.[56]

Figure 3.4 illustrates the use of BVO in color flow data as a method to quantify relative registration error, which is independent of the grayscale data used in the registration process. Breast compression thicknesses were 7.0 and 7.5 cm, and volumes of color flow pixels were measured as 880 and 1220 cc giving a fractional change in color

pixel density (CPD) of 0.4 and change in BVO from 0.51 before registration to 0.74 after registration.

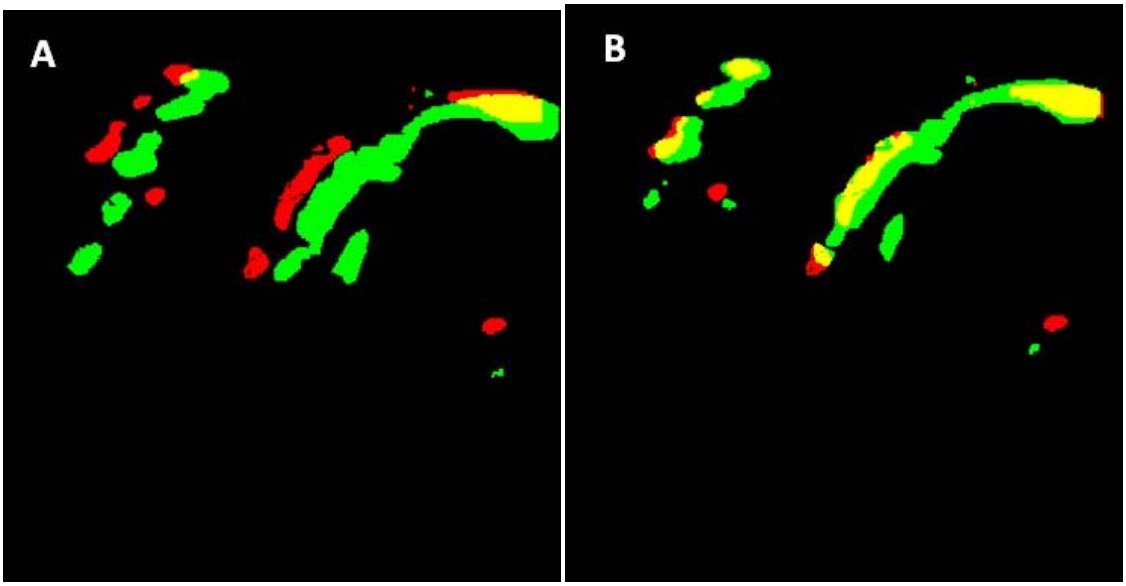

Figure 3.4: Unregistered pair (A) and registered pair (B) in a slice of 3D Doppler color image volumes with grayscale portion blacked out. Red was the color of blood flow under moderate breast compression; green under relaxed compression and yellow was the overlap region. Notice the increase in flow with relaxation and also increase in yellow region with registration. The registration was performed on the grayscale portion of the image volume (not shown here). Refer Figure 3.5 and Figure 3.6.

In method b), registration accuracy could be obtained from the displacement of the vessel segments from each other in the registered image volume pair. The appearance of a color pixel in a Doppler image volume depends on Doppler US system settings including PRF, WF and grayscale-color balance. In a real time 2D Doppler US image, portions of the blood vessel segment were not always seen; the diameter appeared to fluctuate with the cardiac cycle and with subtle variations in attenuation by overlying tissues as the view was changed slightly under identical Doppler settings in the US system. The length of the displayed vessel segment varied even more substantially, and if not tightly curved, contained little measurable information about vessel position along the direction of the vessel. A curved line along the vessel's geometric center could best represent the position of the blood vessel segment in the 3D Doppler image set, but the information on the location of the curve at any one point was only in the two dimensions normal to the vessel segment at that point. Measurement in 3D of the normal displacement between the two renderings of the vessel gave the registration error at that location in two of the three dimensions.

Centerline Separation Value (CSV) was defined as the perpendicular distance between the centers of blood vessels measured in the 3D image volume. CSV of blood vessels is based on a curved line passing through the geometric center of the vessels. As totally automatable and independent of the image information used in registration, the CSV is a good alternate indicator of registration error. MRE is based on a few observer-

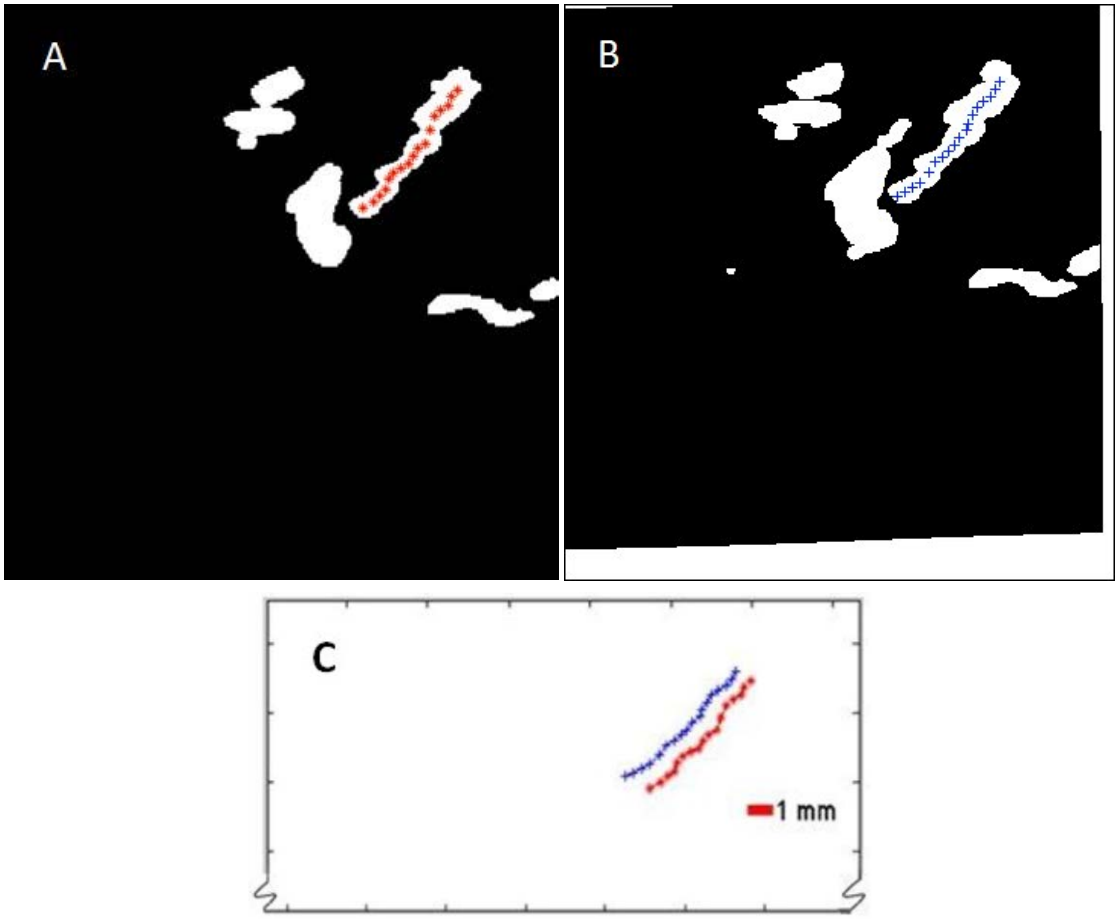

Figure 3.5: 2D automated centerline extraction algorithm has identified points along the centerline on the reference image mask (A) and the registered homologous image mask (B). (C) Lines of pluses and stars are the centerlines of blood vessel from A & B, respectively. The CSV was estimated to be the mean length of separation between these two line segments. In this compression-relaxation study, CSV was estimated to be 1.0±0.4 mm while the reference MRE obtained from registration of the corresponding DI-G grayscale image volume pair was 0.8±0.4 mm.

identified points on the structures in grayscale image volume. In order to match the reader study procedure and for convenience in programming, the fitting to the centers of the vessels was performed only within individual 2D images of the 3D Doppler image

volume along the maximum length of the vessel. This distance is the registration error vector component in one of the three dimensions in space. Thus, for assumed isotropic error, CSV_{3D} should yield a value that is approximately $\sqrt{3}$ (1.73) times CSV. If performed in a full 3D fit, CSV_{3D} would give a more accurate 2D estimate of registration error.

In our software, the semi-automated extraction of the centerline needed 2 inputs from the user – start and end point of the blood vessel segment. The algorithm worked as follows. The lengths of line segments within the blood vessel passing through the starting point at 0^0, 45^0, 90^0 and 135^0 were measured in the image plane. The midpoint of the line segment with minimum length among the four was marked as the geometric center of a small region of the blood vessel around that point. Along the line segment of maximum length, another point at a distance *d* from the location of the previous point was identified as the next center point. The process of identification of center points was repeated until the end point was reached. A value of d=4 pixels was used. As a technique demonstration, two test cases were evaluated with one at equal breast compression and the other at reduced compression, taken in the same session. An example of the method shown in Figure 3.5 is a masked Doppler image volume pair acquired before and after relaxation of compression along with the points on the centerline.

In the method c), presence of special features such as branches in the blood vessels in the Doppler image volumes could provide identifiable homologous points, which were more valuable than lines, for 3D estimate of registration error. The mean separation of the radiologist identified Doppler fiducial (DF) point yields DF separation value (DFSV) that could be compared with the reference grayscale MRE. In order to demonstrate the technique in this study, 2 cases were selected with sufficient visibility identifiable blood flow patterns, one pair at equal compression levels and the other pair at different compressions. Again an example of this method was shown. Figure 3.6 A and B shows the original 2D Doppler image pairs of a region around the tumor acquired at equal breast compression, separated by repositioning, in the same session. Shown in Figure 3.6C and D are the registered 2D Doppler image pair with DF points along the center of twisting blood vessel segments or bifurcations.

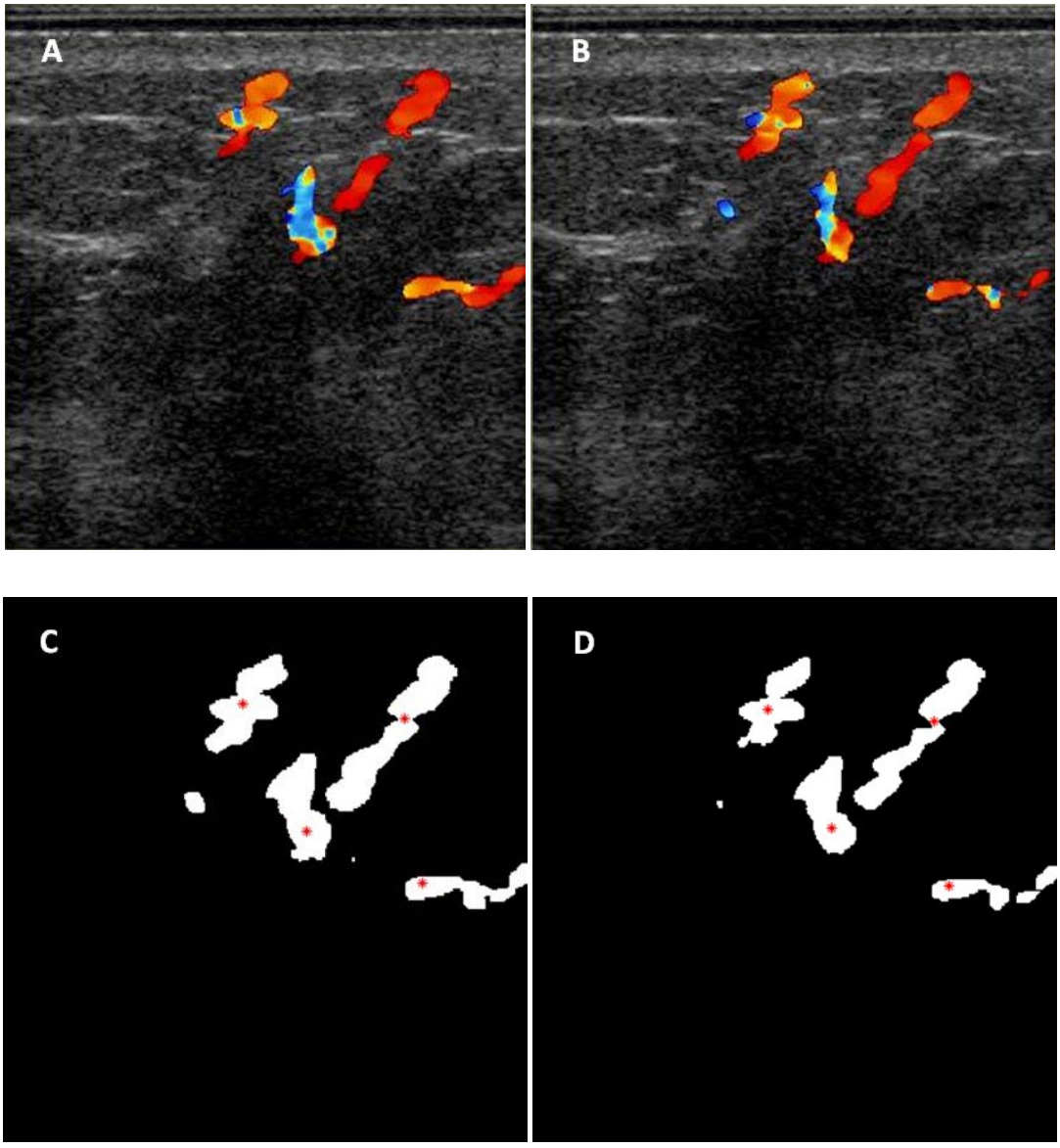

Figure 3.6: A patient with invasive ductal carcinoma showing hypo-echoic, irregular shaped mass on the left breast scanned before chemotherapy. A & B: Doppler image pair showing blood flow around the tumor scanned at equal breast compressions in the same session within 30 minutes. C & D: Registered DI-G image pairs of reference and homologous image volumes respectively. Radiologist identified Doppler fiducial (DF) points on twisting blood vessel segment are shown for reference as gray-colored stars. Separation between 17 of the DF pairs was 0.3±0.3 mm compared with an MRE of 0.2±0.2 mm from fiducials on the grayscale image volumes.

3.3 Results and Summary

Registration transformations that yielded an MRE less than 10 mm were considered as successful registrations.

3.3.1 IVBaR on reproducibility cases

Registration was successful on 9 of 10 ABU reproducibility studies with MRE±SD = 3.2±1.2 mm (maximum = 5.5 mm). One out of ten registrations of reproducibility study cases failed with MRE±SD = 22.4±9.3 mm due to external skin marks from an earlier surgical procedure that made repetition of mammography-style compression very difficult and registration unsuccessful.

3.3.2 IVBaR on chemotherapy cases

Among the 10 subjects undergoing chemotherapy, 5 were evaluated at all three time points along chemotherapy of which only 3 were evaluated in the same view (CC) resulting in 3 pairs each of pre-mid; mid-post and pre-post combinations. Results on the 17 image volume pairs on chemotherapy cases (Table 3.1) includes the successful registration on 5 of 7 pre- to mid-, 4 of 5 mid- to post- and 3 of 5 pre- to post-chemotherapy scans with an overall MRE±SD = 5.2±2.0 mm (maximum = 9.2 mm). In Figure 3.7(A), a rectangular grid of deformation in the US imaging plane is shown for a successful registration with MRE of 4.5±2.1 mm. Figure 3.7(B) is the corresponding B-mode image from registering the mid- to post-chemotherapy image volumes. An indistinct hypo-echoic mass is present at the center bottom of the 2D image shown roughly by a white colored oval. Shown in Figure 3.8 is the displacement of fiducial markers in transformation of a pre-chemotherapy to post-chemotherapy B-mode ABU image volume.

Among these tumor cases, 3 cases were registered successfully at all stages of chemotherapy and had lower MRE than most of the other registered cases. This might explain the slightly low registration errors as well as pixel displacement in the 3 pre- to post-chemotherapy image volume registration (refer the last row in Table 3.1). Tissue

deformability, phase aberrations and refraction artifacts due to in-homogeneities are large in the human breast leading to high registration errors. Reasons for inability to register some of the US scans include necessary changes in compression thickness and force possibly due to patient weight loss and also positioning differences within the range of normal mammographic repositioning. The 5 unsuccessfully registered image volume pairs of chemotherapy cases have MRE±SD of 30.8±18.4 mm.

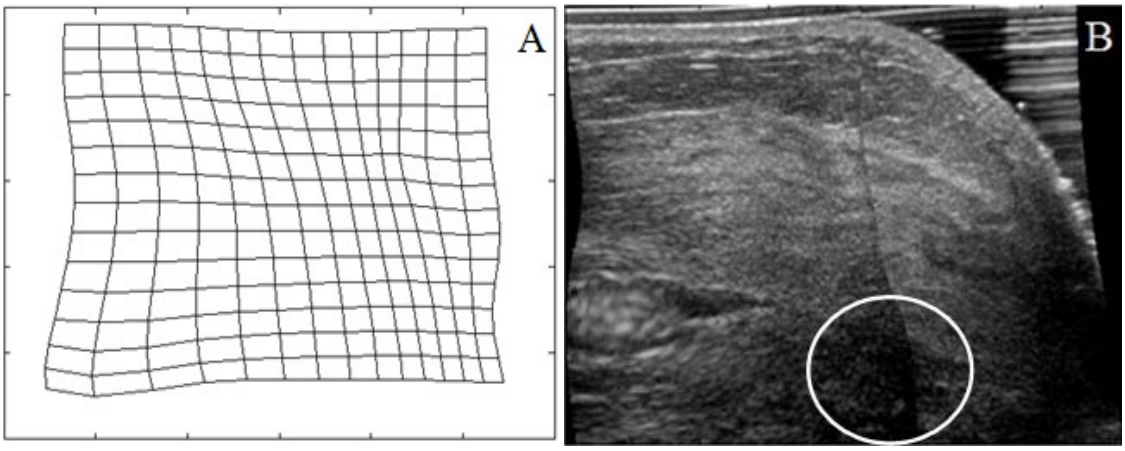

Figure 3.7: (A) Rectangular grid of deformation in the US image plane of a successful registration with MRE = 4.5±2.1 mm and (B) the corresponding slice in the mid- to post-chemotherapy registered image volume with indistinct hypo-echoic mass at the center bottom identified roughly by the white oval.

Table 3.1: Description of various types of scans with the number of successful registrations. The mean, standard deviation and maximum registration errors and pixel displacement of registered 3D US grayscale image volumes in the study population going through chemotherapy was shown. 12 out of 17 longitudinal scans and overall 21 out of 27 3D ABU grayscale scan pairs were registered with the MRE = 5.2±2 mm and 4.3±1.7 mm, respectively. Corresponding mean pixel displacements are 12±2.6 mm and 9.9±2.4 mm.

Type of scan	#Registered/ #Total	Registration error (mm)			Pixel Displacement (mm)		
		Mean	SD	Max	Mean	SD	Max
Reproducibility	9 / 10	3.2	1.2	5.5	7.2	2.1	13.4
Pre- to mid-chemotherapy	5 / 7	4.8	1.7	7.9	13.7	3.4	24.8
Mid- to post-chemotherapy	4 / 5	5.5	2.5	9.2	10.5	1.9	15.6
Pre- to post-chemotherapy	3 / 5	5.3	1.9	8.1	11.1	2.3	16.8

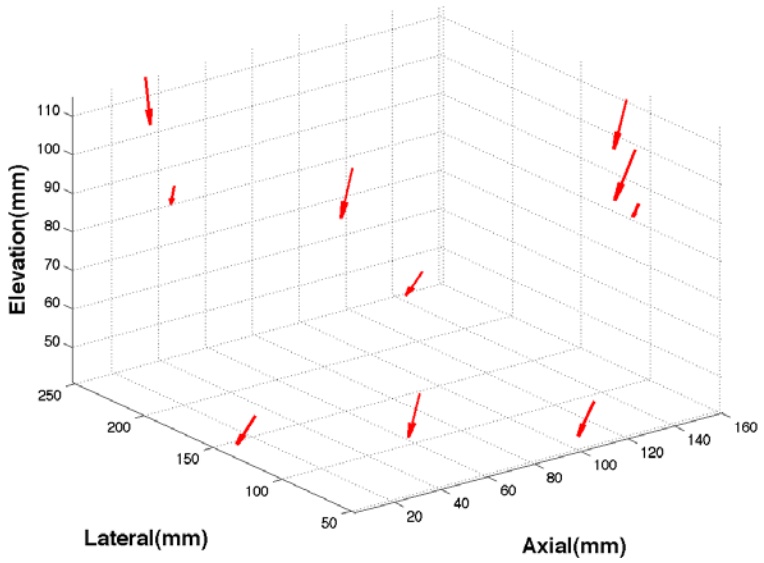

Figure 3.8: Movement of fiducial markers on target post-chemotherapy image volume to align with the reference pre-chemotherapy image volume with MRE = 5.5±1.5 mm (maximum = 13.2 mm), as estimated by automated registration. (Size of arrows doubled in order to view arrow-heads better).

3.3.3 Tumor volume estimation

Using the transformation map obtained in registering the original pre- to later (mid- or post-) chemotherapy grayscale image volumes, later scan-chemotherapy tumor volume was obtained using registration method. Due to unsuccessful registration, partial tumor visibility, dominating shadowing artifacts and multi-focal tumors, only 7 out of 10 cases were selected for the automated tumor volume estimation. In the 7 cases evaluated, the radiologist estimation of tumor volume in pre-chemotherapy scan ranged from 0.2 – 9.93 cc (mean =3.2 cc). In the later scan, radiologist estimation of tumor volume ranged from 0.1 cc – 2.1 cc (mean = 1.3 cc) as compared to the registration-based automated tumor volume estimate that ranged from 0.1 cc – 2.2 cc (mean = 1.5 cc), as shown in Figure 3.9. The correlation coefficient between these estimates was 0.9876 ($P<0.0001$). The mean percentage change in ratio of tumor volumes from the tested method and manual method was 86±8%. Thus, prior knowledge of the boundary of the lesion in the reference image volume and successful registration allow the volume of the lesion in the homologous image volume to be obtained with reasonable accuracy. Furthermore, the

longest linear tumor dimension from the margins in automated and hand-scans were within 20±13 % of those from the pathology, where the tumor specimen was often distorted from its shape *in vivo*. The main advantage of such automated tumor volume estimation was the reduced necessity of manually identifying the tumor boundary in subsequent scans. This saved the radiologist's time and perhaps gave a more accurate fractional volume change.

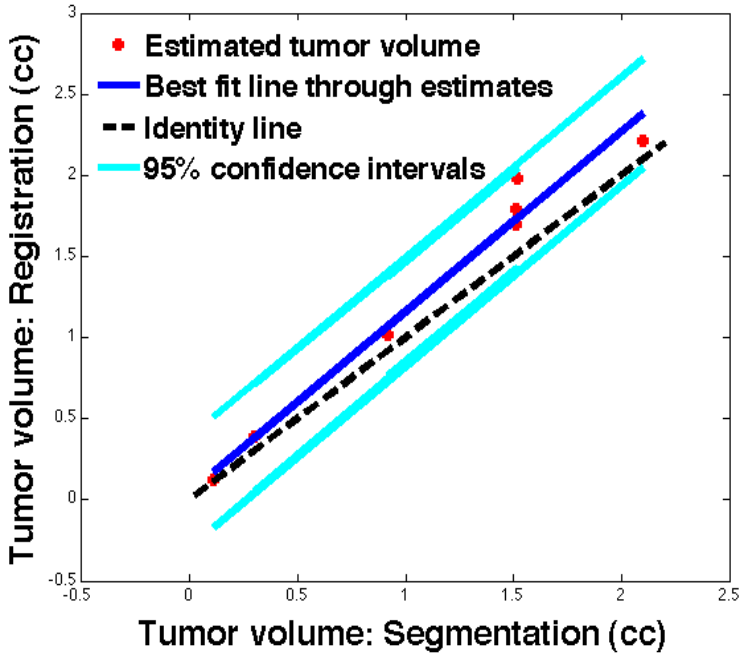

Figure 3.9: Post-chemotherapy tumor volume as estimated by automated registration in comparison with that of the radiologist hand-segmentation in 7 cases. The reference line (y=1.11x+0.05) derived by least squares method was shown along with 95% confidence interval lines. The black dotted line was the identity line shown for reference.

3.3.4 Doppler imaging

The color flow Doppler image pairs were acquired on a small region surrounding the lesion at multiple compressions on 3 patients undergoing chemotherapy and 5 patients with suspicious/unknown masses using identical Doppler settings. From the Doppler studies, the detectable vascularity or color pixel density (CPD) was estimated to change by +1.5%, -9% and +86% respectively for equal compression reproducibility, for 7% increased compression and for 9% relaxation of breast compression. In relaxation of breasts that were under compression, an initial rush of blood suggested that the steady state was not reached in a time frame of 1-2 minutes and further investigation was needed.

For reproducibility and changing compression cases, fractional change in CPD measured as a function of fractional change in plate separation distance is shown in Figure 3.10. For additional compressions below 10% of the original compression level, the resulting decrease in CPD gave a linear best-fit estimate of 1.4x+0.5 where x=percentage change in plate separation for increasing compression (x<0). Relaxations up to 15% resulted in a strong increase of CPD, recorded after the initial rush of blood flow, giving a 2nd order polynomial fit to the change in CPD of $0.4x^2+0.1x-0.9$, for x>0.

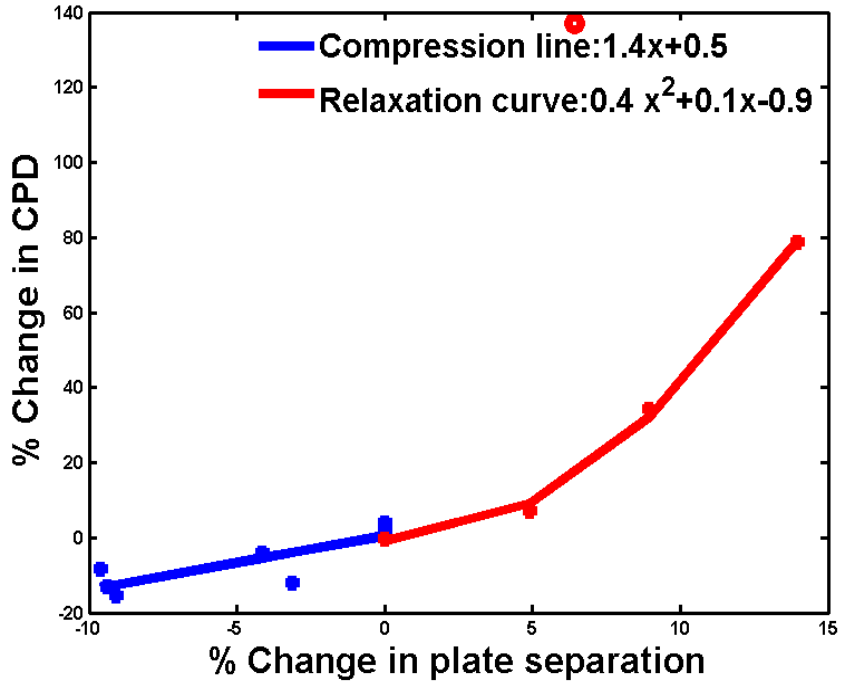

Figure 3.10: Percentage change in detected vascularity (CPD) given as a function of percentage change (x) in breast compression or plate separation for 8 patients. Doppler measurements were performed after subject had been under compression for the 10 minutes duration of other scans, approximately. Additional compression beyond that for the pulsatility resulted in a drop in blood flow giving a linear fit to CPD change: 1.4x+1.5. Relaxations below 15% resulted in a sudden increase in CPD may suggest that measurements be acquired after a brief relaxation period to avoid the non-steady-state rush of blood from the measured region. Ignoring the obvious outlier (open circle), CPD changed in non-linear manner (refer to text).

3.3.5 Doppler Registration accuracy

Table 3.2 indicates that applying the transform obtained via grayscale registration to the color pixels of the Doppler images produces an increase in BVO, showing that the blood vessels, tissues and other structures overlay better spatially after registration.

Increase in BVO was nominal (31%) when registering image volumes acquired at the same compression level, as there was little misalignment between scans. On the other hand, the increase in BVO (213% and 88%) was high in cases with unequal breast compression levels, indicating that there was considerable shift of tissue structures with changing compression. Also summarized in 3rd column in Table 3.2, the MRE is substantially lower in registrations of image volumes acquired with changing breast compression than that with the pre- to post-chemotherapy scans (refer 3rd column in Table 3.1). In these 15 Doppler image volume pairs, BVO increased from 0.32 to 0.59 or about +84% with IVBaR for various compression levels.

Table 3.2: Table showing the various study groups of population that underwent the different amounts of compression. Note that #C denotes number of patient undergoing chemotherapy and #M denotes number of patients with suspicious or unknown mass who were also scheduled to undergo biopsy. The third and fourth columns give the mean registration error (mm) in registering the grayscale portion of the Doppler image volume (DI-G pair) and the corresponding mean CSV (mm) of registered image volume pair. The fifth column gives the change in BVO with registration.

Doppler study type	#Scan pairs on #patients	MRE (mm)	CSV (mm)	Change in BVO
Reproducibility	4 on 3C	0.6±0.4	0.7±0.3	0.59 to 0.77 (+31%)
More compression	7 on 2C,5M	1.2±0.5	1.8±0.6	0.15 to 0.47 (+213%)
Less compression	4 on 1C,1M	1.6±0.9	1.8±0.8	0.33 to 0.62 (+88%)

In the *centerline separation method*, all the cases shown in Table 3.2 are evaluated with equal, increased and relaxed breast compression. In these 15 Doppler image volume pairs, the mean MRE and mean standard deviation were estimated to be 1.1±0.6 mm while the corresponding mean CSV was 1.5±0.6 mm. In a breast relaxation study shown in Figure 3.5, a CSV of 1.0±0.4 mm is obtained from 289 points along the centerlines of 13 blood vessel segments. This is comparable to the reference MRE of 0.8±0.4 mm from registration of DI-G grayscale image volume pair. In the same subject, equal breast compression Doppler image volume pair acquired in the same session yielded a CSV of 0.3±0.1 mm from 299 points along the centerlines of 13 blood vessel segments that is comparable to the reference MRE of 0.2±0.2 mm.

In the *radiologist identified fiducial method* of evaluating registration accuracy on 2 test cases, 17 fiducial points were identified on the color flow pairs acquired in the

same session with equal compression as shown in Figure 3.6 and the DFSV of 0.3±0.3 mm is comparable with the reference grayscale MRE of 0.2±0.2 mm from grayscale image volume. In another Doppler image volume pair with 7% relaxation in breast compression, the DFSV value obtained using 30 fiducial points was 1.3±0.5 mm *vs.* the reference grayscale MRE of 0.8±0.4 mm from registration of DI-G grayscale image volumes.

3.4 Discussions and Conclusions

In the majority of pre- and post-chemotherapy ABU scans, it was possible to spatially align the two temporally separated image volumes with a modest alignment error sufficiently small enough to aid identification of tumor remains after half or all of the neoadjuvant chemotherapy treatment. Breast image volume pairs acquired in the same session were registered in order to obtain a baseline registration study with minimal internal change. Almost all the registration on pairs involving immediate repositioning of the breast cases was successful, with registration error within a few millimeters. Furthermore, in this study, automated US scans have fixed slice separation (e.g., 0.4 mm) and thus eliminated the approximation involved in estimating the tumor volume in hand-scans. It can be seen from BVO, grayscale MRE and Doppler MRE in reproducibility and change of compression color flow Doppler studies that spatial registration does align the image volumes. This alignment appears to be enough that it should help with the often difficult identification of the residual tumor location in post-treatment cases with full or substantial regression.

While MIAMI Fuse© is a very versatile algorithm for multimodality registration, it is computationally intensive, limiting the number of control points by working on the entire image volume. Deformations with high spatial frequencies may not be fully recovered. Also, registrations could be improved with better placement of initial control points or by adding control points within the ROI. More work is needed in finding the optimal number of control points for 3D US image volume of a given quality. Clinical registration is expected to become faster with better optimization of algorithms and faster computers. Spatial compounding or alternate registration methods may improve

registration results achieved in this study.[57] Spatial compound imaging, which is now available in many US systems, increases signal-to-noise ratio by using multiple scan directions and reduces shadowing, motion and refraction artifacts.[58] Median filtering and speckle reduction imaging available in the Logic9 system could also improve registration accuracy.[59,60] Great care should be taken with image processing techniques as the images may look unfamiliar to clinicians. Thus for practical considerations, it may be therefore be necessary to retain original image and use the processed image as secondary source of information.[61]

Measuring the accuracy of clinical registrations was a very challenging task in the absence of a "gold standard". For such evaluations, multiple observers may be required to mark fiducials as well as the boundary of the tumor. Even though a multi-reader study would bring out statistically significant results along with inter-reader and intra-reader variability comparisons, this could not be performed in this preliminary study and could be a part of a larger clinical trial. A breast phantom with tissues and structures similar to that in breast and which can mimic the chemotherapy induced changes in a breast mass was fairly difficult to make.[62] Numerical models have been tested, but it was outside the scope of this study.

Estimation of tumor volume change is considered as a good tool for assessing effectiveness of therapy. Conventionally, the single longest linear dimension was considered as a measure of the tumor size. In some studies, the 3 longest orthogonal linear dimensions are considered as a measure of the tumor volume. The effectiveness of therapy was classified as a complete or partial responder depending on the change in these 1 or 3 linear dimensions. The methodology used in this manuscript was to estimate the actual tumor volume change using image registration, having measured the initial tumor volume. IVBaR applied on a tumor segmented pre-chemotherapy image volume provides a means to track the remaining tumor tissues and residues in the post-chemotherapy image volume and also to determine change in tumor volume automatically. This has been compared with the radiologist's hand segmented estimate of the post-chemotherapy tumor volume. In this process, the segmented tumor region in pre-chemotherapy image volume does not contribute towards the registration. Upon the successful application of this procedure to a larger clinical study, this could have clinical

impact by minimal use of radiologist's time in identifying tumor region in subsequent scans.

Using Doppler image volumes, three independent indicators of accuracy of the registrations of B-mode image volumes (blood vessel overlap, centerline extraction and radiologist identification of fiducial features) have been explored. The first two of these three measures are automated and minimally dependent on the observer. Among these measures, CSV of blood vessels is based on a best fit curved line passing through the geometric center of the blood vessels and hence should be less noisy indicator of registration error than MRE and DFSV which are based on a few points on the structures in the grayscale image volumes and blood vessels in the Doppler image volumes, respectively. These methods can be applied to any other easily segmented objects in image volumes from any imaging modality, as those segmented features were not critical for the registration. Doppler scans covered a smaller ROI of breast, generally centered under the compression plate when compared with the whole breast B-mode image volume. This could have contributed to a lower MRE in Doppler image volumes. The Doppler vascularity metric, CPD, can be measured relatively consistently over the range of compressions changes from -10% to +15% of the compression initially judged by the patient as acceptable for a series of scans of up to 10 minutes.

The cardiac-gated Doppler US study was performed assuming that there was a uniform time delay since the onset of R-wave for blood flow to peak at the breast for all patients and this could be changed. There are various factors that contribute to this time delay including stress-level, emotions, heart rate, and age, etc. Newer US systems have a peak-detect Doppler mode that takes Doppler scan at various time points during a cardiac cycle allowing for post-processing to detect the peak blood flow in the breast. During the Doppler scan, the patients had been under mammographic-compression for a few minutes (as long as it took for getting good coupling in the breast through the compression plate) and this could have contributed towards low blood flow in some subjects. In the future work, care will have to be taken to relax compression for an adequate time period before modest recompression in the Doppler portion of the US study.

3.5 Acknowledgements

I would like to thank Sakina Zabuawala and Zhi Yang for help with quantitative Doppler measurements and in developing software tool for hand segmentation of tumor region, respectively. This work was supported in part by U.S. Public Health Service grants PO1 CA87634 and RO1 CA91713 (a partnership with GE Global Research).

3.6 References

1 DB Kopans, “The positive predictive value of mammography,” Am. J. Roentgenol 158, 521–526 , 1992.

2 WA Berg, JD Blume, JB Cormack, EB Mendelson, D Lehrer, M Bohm-Velez, ED Pisano, RA Jong, WP Evans, MJ Morton, MC Mahoney, LH Larsen, RG Barr, DM Farria, HS Marques, K Boparai, “Combined screening with ultrasound and mammography vs mammography alone in women at elevated risk of breast cancer,” J. Am. Med. Assoc. 299(18), 2151–2163, 2008.

3 WA Berg, “Rationale for a trial of screening breast ultrasound: American College of Radiology Imaging Network (ACRIN) 6666,” Am. J. Radiol. 180, 1225–1228, 2003.

4 AR Padhani, JE Husband, “Dynamic contrast-enhanced MRI studies in oncology with an emphasis on quantification, validation and human studies,” Clinical Radiol. 56, 607–620, 2001.

5 MB Barton, R Harris, SW Fletcher, “Does this person have Breast Cancer? The screening clinical breast examination: Should it be done? How?,” J. Am. Med. Assoc. 282(13), 1270–1280, 1999.

6 VP Jackson, “The role of US in breast imaging,” Radiology 177(2), 305–311, 1990.

7 SM Durfee, DLG Selland, DN Smith, SC Lester, CM Kaelin, JE Meyer, “Sonographic evaluation of clinically palpable breast cancers invisible on mammography,” The Breast Journal 6, 247–51, 2000.

8 LW Bassett, C Kimme-Smith, “Breast sonography,” Am. J. Roentgenol. 156, 449–455, 1991.

9 SV Hilton, GR Leopold, LK Olson, SA Willson, “Real-time breast sonography: application in 300 consecutive patients,” Am. J. Roentgenol. 147, 479–486, 1986.

10 VP Jackson, “The current role of US in breast imaging,” Radiol. Clin. North Am. 33, 1167–1170, 1995.

11 TM Kolb, J Lichy, JH Newhouse, “Occult cancer in women with dense breasts: Detection with screening US- Diagnostic yield and tumour characteristics,” Radiology 207, 191–9, 1998.

12 KJW Taylor, C Merritt, C Piccoli, “Ultrasound as a complement to mammography and breast examination to characterize breast masses,” Ultrasound Med. Biol. 28(1), 19–26, 2002.

13 HA Moss, PD Britton, CDR Flower, AH Freeman, DJ Lomas, RML Warren, “How reliable is modern breast imaging in differentiating benign from malignant breast lesions in the symptomatic population?,” Clin. Radiol. 54, 676–682, 1999.

14 AT Stavros, D Thickman, CL Rapp, MA Dennis, SH Parker, GA Sisney, “Solid breast nodules: Use of sonography to distinguish between benign and malignant lesions,” Radiology 196, 123–134, 1995.

15 FW Conway, CW Hayes, WH Brewer, “Occult Breast masses: Use of a mammographic localization grid for US evaluation,” Radiology 181,143–146, 1991.

16 SC Partridge, JE Gibbs, Y Lu, “MRI measurements of breast tumor volume predict response to neoadjuvant chemotherapy and recurrence-free survival,” Am. J. Roentgenol 184, 1774–1781, 2005.

17 MA Roubidoux, GL Le Carpentier, JB Fowles, B Bartz, D Pai, SP Gordon, AF Schott, TD Johnson, PL Carson, “Sonographic evaluation of early-stage breast cancers that undergo neoadjuvant chemotherapy,” J. Ultras. Med. 24, 885–895, 2005.

18 AB Chagpar, LP Middleton, AA Sahin, P Dempsey, AU Buzdar, AN Mirza, FC Ames, GV Babiera, BW Feing, KK Hunt, HM Kuerer, F Meric-Bernstam, MI Ross, SE Singletary, “Accuracy of physical examination, ultrasonography, and mammography in predicting residual pathologic tumor size in patients treated with neoadjuvant chemotherapy,” Ann. Surg. 243, 257–64, 2006.

19 T Nakamura, T Fukutomi, H Tsuda, S Akashi-Tanaka, K Matsuo, C Shimizu, K Miyakawa, "Changes in finds of mammography, ultrasonography and contrast-induced computed tomography of three histological complete responders with primary breast cancer before and after neoadjuvant chemotherapy: case reports," Jpn. J. Clin. Oncol. 30, 453–457, 2000.
20 LS Brown, "A Survey of Image Registration Techniques," ACM Computing Surveys 24(4), 325–356, 1992.
21 B Zitova, J Flusser, "Image registration methods: a survey," Image and Vision Computing 21, 977–1000, 2003.
22 CR Meyer, JL Boes, B Kim, PH Bland, GL LeCarpentier, JB Fowlkes, MA Roubidoux, PL Carson, "Semiautomatic Registration of Volumetric Ultrasound Scans," Ultrasound Med. Biol. 25(3), 339–347, 1999.
23 PJ Edwards, DLG Hill, JA Little, DJ Hawkes, "A three-component deformation model for image-guided surgery," Med. Image Anal. 2(4), 355–367, 1998.
24 JG Rosenman, EP Miller, G Tracton, TJ Cullip, "Image registration: An essential part of radiation therapy treatment planning," Int. J. Radiat. Oncol. Biol. Phys. 40(1), 197–205, 1998.
25 J Weese, GP Penney, P Desmedt, TM Buzug, DLG Hill, "Voxel based 2D/3D registration of fluoroscopy images and CT scans for image guided surgery," IEEE Trans. Information Tech Biomedicine 1(4), 284–293, 1997.
26 JP Thirion, "Image matching as a diffusion process: an analogy with Maxwell's demons," Med. Image Anal. 2(3), 243–260, 1998.
27 X Pennec, P Cachier, N Ayache, "Understanding the Demon's algorithm: 3D non-rigid registration by gradient descent," Proceedings of MICCAI, LNCS (Springer, Berlin/Heidelberg, 1999) Vol. 1679, pp. 597–606.
28 H Wang, L Dong, J O'Daniel, R Mohan, AS Garden, KK Ang, DA Kuban, M Bonnen, JY Chang, R Cheung, "Validation of accelerated 'demons' algorithm for deformable image registration in radiation therapy," Phys. Med. Biol. 50(12), 2887–2905, 2005.
29 R Kashani, M Hub, JM Balter, ML Kessler, L Dong, L Zhang, L Xing, Y Xie, D Hawkes, JA Schnabel, J McClelland, S Joshi, Q Chen, W Lu, "Objective assessment of deformable image registration in radiotherapy: A multi-institution study," Med. Phys. 35(12), 5944–5953, 2008.
30 FL Bookstein, "Principal Warps: Thin-plate splines and decompositions of deformation," IEEE Trans. Pattern Anal. Mach. Intell. 11(6), 567–585, 1989.
31 ML Kessler, "Image registration and data fusion in radiation therapy," British J Radiol. 79, S99–S108, 2006.
32 M Holden, "A Review of Geometric Transformations for Nonrigid Body Registration," IEEE Trans. Med. Imaging 27(1), 111–128, 2008.
33 A Kapur, PL Carson, J Eberhard, "Combination of digital mammography with semi-automated 3D breast ultrasound," Technol. Cancer Res. Treat. 3(4), 325–334, 2004.
34 G Narayanasamy, GL LeCarpentier, S Zabuawala, JB Fowlkes, M Roubidoux, S Sinha, PL Carson, "Non-rigid registration of three-dimensional(3D) grayscale and Doppler ultrasound breast images," Proceedings of IEEE Engineering in Medicine and Biology Society (Lyon, France, 2007), pp. 91–94.
35 RC Booi, JF Krücker, MM Goodsitt, M O'donnell, A Kapur, GL Lecarpentier, MA Roubidoux, JB Fowlkes, PL Carson, "Evaluating thin compression paddles for Mammographically compatible ultrasound," Ultrasound Med. Biol. 33(3), 472–482, 2007.
36 SP Sinha, MM Goodsitt, MA Roubidoux, RC Booi, GL LeCarpentier, CR Lashbrook, KE Thomenius, CL Chalek, PL Carson, "Automated Ultrasound Scanning on a Dual-Modality Breast Imaging System," J. Ultrasound Med. 26, 645–655, 2007.

37 G Narayanasamy, JB Fowlkes, OD Kripfgans, JA Jacobson, M De Maeseneer, RM Schmidt, PL Carson, “Ultrasound of the finger for human identification using biometrics,” Ultras. Med. Biol. 34(3), 392–399, 2008.
38 PL Carson, GL LeCarpentier, MA Roubidoux, RQ Erkamp, JB Fowlkes, MM Goodsitt, “Physics and Technology of Ultrasound Breast Imaging Including Automated 3D,” in A Karellas and ML Giger, eds, 2004 Syllabus, Advances in Breast Imaging: Physics, Technology, and Clinical Applications, RSNA Categorical Course in Diagnostic Radiology Physics, RSNA, 223–232, 2004.
39 CR Meyer, JL Boes, B Kim, PH Bland, KR Zasadny, PV Kison, K Koral, KA Frey, RL Wahl, “Demonstration of accuracy and clinical versatility of mutual information for automatic multimodality image fusion using affine and thin plate spline warped geometric deformations,” Med. Image Anal. 1(3), 195–206, 1997.
40 J. Krücker and Ph. D. Thesis, Applied Physics Program (University of Michigan, pp. 45, 2003.
41 J Folkman, “Tumor angiogenesis: Therapeutic implications,” New Engl. J. Med. 285, 1182–1186, 1971.
42 G Bergers, LE Benjamin, “Angiogenesis: Tumorigenesis and the angiogenic switch,” Nature Reviews Cancer 3, 401–410, 2003.
43 PT Bhatti, GL LeCarpentier, MA Roubidoux, JB Fowlkes, MA Helvie, PL Carson, “Discrimination of sonographically detected breast masses using frequency shift color Doppler imaging in combination with age and gray scale criteria,” J. Ultrasound Med. 20, 343–350, 2001.
44 GL LeCarpentier, MA Roubidoux, JB Fowlkes, JF Krücker, KA Hunt, C Paramagul, TD Johnson, NJ Thorson, KD Engle, PL Carson, “Suspicious Breast Lesions: Assessment of 3D Doppler US Indexes for Classification in a Test Population and Fourfold Cross-Validation Scheme,” Radiology 249, 463–470, 2008.
45 PL Carson, JB Fowlkes, MA Roubidoux, AP Moskalik, A Govil, D Normolle, GL LeCarpentier, S Nattakom, MR Helvie, JM Rubin, “3-D color Doppler image quantification of breast masses,” Ultrasound Med. Biol. 24, 945–952, 1998.
46 BC Porter, DJ Rubens, JG Strang, J Smith, S Totterman, KJ Parker, “Three-dimensional registration and fusion of ultrasound and MRI using major vessels as fiducial markers,” IEEE Trans. Med. Imaging 20(4), 354–359, 2001.
47 ND Nanayakkara, B Chiu, A Samani, JD Spence, J Samarabandu, G Parraga, A Fenster, “Nonrigid registration of three-dimensional ultrasound and magnetic resonance images of the carotid arteries,” Med. Phys. 36(2), 373–385, 2009.
48 WM Wells III, P Viola, H Atsumi, S Nakajima, R Kikinis, “Multi-modal volume registration by maximization of mutual information,” Med. Image Anal. 1(1), 35–5, 1996.
49 PH Schönemann, “A generalized solution of the orthogonal procrustes problem,” Psychometrika 31, 1–10, 1966.
50 D Rueckert, LI Sonoda, C Hayes, DLG Hill, MO Leach, DJ Hawkes, “Nonrigid registration using free-form deformations: application to breast MR images,” IEEE Trans. Med. Imaging 18(8), 712–721, 1999.
51 H Johnson, G Christensen, “Landmark and Intensity-based, consistent thin plate spline image registration,” Information Proc. Med. Imag. 2082, 329–343, 2001.
52 FL Bookstein, Morphometric Tools for Landmark Data (Cambridge University Press, Cambridge, U.K., 1991).
53 FL Bookstein, “Shape and information in medical images: a decade of morphometric synthesis,” Computer Vision and Image Understanding 66, 97–118, 1997.
54 R Shekhar, V Zagrodsky, “Mutual Information-based rigid and non-rigid registration of ultrasound volumes,” IEEE Trans. Med. Imaging 21(1), 9–22, 2002.

55 JPW Pluim, JBA Maintz, MA Viergever, “Mutual information matching in multiresolution contexts,” Image Vision Computing 19, 45–52, 2001.
56 SA Carp, T Kauffman, Q Fang, E Rafferty, R Moore, D Kopans, D Boas, “Compression-induced changes in the physiological state of the breast as observed through frequency domain photon migration measurements,” J. Biomed. Opt. 11(6), 064016-1 – 064016-6, 2006.
57 JF Krücker, CR Meyer, GL LeCarpentier, JB Fowlkes, PL Carson, “3D spatial compounding of ultrasound images using image-based non-rigid registration,” Ultrasound Med. Biol. 26(9), 1475–1488, 2000.
58 A Moskalik, PL Carson, CR Meyer, JB Fowlkes, JM Rubin, MA Roubidoux, “Registration of three-dimensional compound ultrasound scans of the breast for refraction and motion correction,” Ultrasound Med. Biol. 21(6), 769–778, 1995.
59 RN Czerwinski, DL Jones, WD O'Brien Jr, “Ultrasound speckle reduction by directional median filtering,” Proceedings of International Conference on Image Processing (Washington D.C., USA, 1995), Vol. 1, pp. 358–361.
60 A Milkowski, Y Li, D. Becker, SO Ishrak, “Speckle reduction imaging” Technical white paper- General Electric Health care (Ultrasound). Last accessed on July 9, 2009. Available: http://www.gehealthcare.com/usen/ultrasound/education/docs/whitepaper_SRI.pdf
61 JF Krücker, GL Lecarpentier, JB Fowlkes, PL Carson, “Rapid elastic image registration for 3-D ultrasound,” IEEE Trans. Med. Imaging 21(11), 1384–1394, 2002.
62 G Narayanasamy, R Narayanan, JB Fowlkes, MA Roubidoux, PL Carson, “Segmentation-free estimation of volume changes in 3D ultrasound of breast phantom lesions,” Proceedings of SPIE Medical Imaging (San Diego, USA, 2007) Vol. 6510, pp. 651033.

CHAPTER 4 TUMOR VOLUME CHANGE ESTIMATION DURING NEOADJUVANT CHEMOTHERAPY USING IMAGE REGISTRATION OF AUTOMATED WHOLE BREAST ULTRASOUND

4.1 Introduction

Neoadjuvant chemotherapy is a drug treatment given to patients before surgery or radiation therapy with the aim of reducing the metastasis and tumor size. This treatment can lead to significant reduction in tumor size and impact the cosmetic outcomes of breast-conserving surgery.[1, 2, 3] Patients with complete response in neoadjuvant chemotherapy have increased overall survival rates as well as improved average disease-free survival.[4] Response of the primary breast tumor to neoadjuvant chemotherapy is a reliable prognostic factor and the response rate has been studied earlier.[5] Success rate in achieving a complete response was independent of the initial tumor volume.[6] According to a study on change in tumor volume measured using MRI, volume change estimation could possibly aid in evaluating response to chemotherapy and identification of local volumetric changes may act as a detection and diagnostic tool in the future.[7] Thus accurate treatment response determination is vital for better management of tumor patients.[8]

Neoadjuvant chemotherapy has been used in breast cancer, primarily for the purpose of down staging the tumor prior to surgical excision, and for evaluating response to chemotherapy. There are important clinical questions regarding the optimum number of chemotherapy cycles to achieve reduction in tumor bulk and the need for mastectomy

after neoadjuvant chemotherapy. These questions and others may be better answered if an imaging modality was identified which could accurately evaluate the patient's response to neoadjuvant chemotherapy. Tumor response to neoadjuvant chemotherapy is studied using mammography, radionuclide imaging, computed tomography (CT), MRI, ultrasound (US) imaging. A previous study performed at the University of Michigan showed that mammography was superior to clinical examination (79% as against 49%) in predicting complete pathologic response to neoadjuvant chemotherapy in locally advanced disease.[9,10] Based on this study at our institution, we evaluated ultrasound pre- and post- chemotherapy in order to make a recommendation for or against breast preservation.

Mammography is the accepted technique for breast screening aimed at detecting breast cancer at early stages. However, exposure to radiation, low positive predictive values and low sensitivity in dense breasts are concerns. [11,12,13] Contrast enhanced MRI is sensitive in detection of malignancy and evaluation of neoadjuvant chemotherapy,[14] but an alternate noninvasive, less expensive and shorter duration procedure would be desirable. US has been very useful in its ability to differentiate simple cysts from solid masses [15 , 16 , 17] and to distinguish mammographically occult cancers especially in mammographically dense breasts. [18 , 19 , 20 , 21] In screening exam, US along with mammography revealed 28% more cancers than mammography alone.[22] US is used frequently to evaluate breast masses (whether palpable or mammographic) as well as changes in the breast structure.[23,24] Currently, breast US scans are performed free hand by radiologists or technologists using two-dimensional (2D) real time US systems with a relatively small (4 – 6 cm wide) field of view in a different geometry than that of mammography, which can make it difficult to correlate lesions between the two modalities. Studies have shown that at least 10% of the time, lesions found in the US images does not correspond with those in the mammograms.[25]

In patients undergoing therapy for malignant breast tumors, it can be vitally important to gauge the effectiveness of the therapy for planning the course of follow-up therapy and therapy monitoring. Clinical breast examination (CBE) is used to study the breast qualitatively for lesion shape, size, location and firmness. However CBE is dependent on the examiner, and is less accurate than imaging.[26] CBE or palpation for

tumor response is less reliable as the examination may estimate response in cases where the tumor does not shrink in size and yet pain and discomfort have subsided. At the same time, imaging evaluation of residual disease after neoadjuvant chemotherapy could help in selecting the surgical procedure and identifying patients who are poor responders. For non-responders, alternate chemotherapy regimens or surgical treatments could be identified.

In the breast, tumor size has been shown to provide some information about the lethality and survival time which is independent of the method of detection.[27] Various available factors that affect tumor prognosis include tumor size, location of tumor, lymph node status, histological response to neoadjuvant chemotherapy, menopausal status, race, gender and phenotype.[28] While a complete response refers to disappearance of any known disease, a partial response refers to more than 50% reduction in measurable tumor size.[29] Conventionally, tumor volume is estimated by largest linear dimensions and sometimes from an ellipsoid formula expressed by height, width and depth. Even though these are inaccurate due to irregular tumor shape and size, the ellipsoid formula provides a quick and easily available estimate of volume. Estimating the volume of the lesion before or after treatment (including neoadjuvant chemotherapy of breast lesions) has been a challenge, mainly because of the ill-defined boundary surrounding these lesions. The notion of tumor volume itself is ambiguous as the tumor contains both normal cells (including connective tissue) as well as living or dead neoplastic cells from abnormal proliferation.[30] There is a tendency to estimate tumor size inaccurately due to poor differentiation between tumor and adjacent soft tissue. Even more accuracy and precision is appropriate for chemotherapy trials where early prediction of response is attempted. As for US tracking, breast tumor boundaries have been particularly poorly defined in image volumes after the onset of chemo or radiation therapy.[31] Studies on neoadjuvant chemotherapy show that it may induce inflammatory or fibrotic changes in the tumor and hence standard methods of assessing tumor size are only moderately successful.[32, 33, 34]

Visual comparisons of scan images have been used to assess qualitative changes during the course of neoadjuvant chemotherapy because of its importance in gauging the effectiveness of treatment in patients undergoing therapy for malignant tumors. Modern techniques such as image registration geometrically align the image volumes so that the

same structures are in the same relative locations. Thus the registered image volume pair will show all of the corresponding structures in the same slice, if the registration is perfect. This may help in detecting subtle changes that may go unnoticed in unregistered images. Manual registration for evaluation of large sets of image volumes may be extremely time-consuming and subject to substantial user variability depending on skill, patience and experience. Automated or semi-automated registration of two image volumes acquired at different time points or in different modalities is done primarily to spatially align the two in the same coordinate system in order to allow better comparison and visualization of changes.[35,36,37]

Registration relates the information in one image to that in the other image quantitatively by determining a one-to-one transformation between points in each image.[38] This helps in correcting for slight changes in sequential studies of the patient and resolves ambiguities in positioning and actual location of some of the structures. For these reasons, registration is becoming an effective tool in diagnostics, therapy planning, image-guided surgery and treatment assessment.[39,40,41]

There are many different registration techniques for computing the geometric transformations that map the coordinates of corresponding points between two image volumes. A simple rotate-translate transformation model is applicable for a rigid site, e.g. human skull. A more general rigid transform is the affine transform that includes rotations, translations, shearing and scaling. Such affine registration techniques are not sufficient to achieve alignment of anatomy in many situations and the localized elastic motion could be better described by a non-rigid transform.[42] Non-rigid transformation is becoming a valuable tool in medical image processing for various applications. Of particular interest in this study is the non-rigid registration of pairs of images acquired before and after therapy.

When the registration is based primarily on an abnormal mass and tissues in the surrounding region, a non-rigid transform could accurately represent the transformation of the boundary and could also be used for estimation of lesion volume change. [43, 44, 45, 46]

In this study, we aimed to evaluate the clinical utility of image registration of compressed whole breast image volumes. Scan image volumes were presented in a pseudo-random order with and without image volume based registration (IVBaR) to each

of the 3 breast radiologists for marking an ellipsoid around the tumor. Comparisons between the radiologist-defined tumor volumes on US image volumes with and without IVBaR were made using standard statistical tools. We propose that IVBaR would aid the radiologists in faster, better estimation of tumor volume. We suggest that spatial registration of the 3D US images of periodic screening studies may become highly useful in detecting and quantifying malignant changes.

4.2 Methods and Materials

Human studies were conducted at the University of Michigan Comprehensive Cancer Center. The Internal Review Board approved all procedures, and informed consents were obtained from patients. Subjects selected for this study included 10 women who were scheduled to undergo neoadjuvant chemotherapy based on the previously confirmed presence of cancer. Among the 10 tumor cases, only 6 with complete tumor visibility in both ultrasound image volumes were chosen for this reader study on tumor volume estimation by three breast radiologists. The mean age of patient was 51±10 years and the mean time difference between pre- and post-chemotherapy scan was 149±57 days. In this research system, ultrasound imaging missed about 1 cm of tissue near the chest wall. With our early experience in applying coupling gel, tissues around the breast periphery were often missed. At times, the ultrasound imaging could not penetrate to the back of the breast.

4.2.1 Equipment Setup, Image Acquisition & Procedures

All US scans were performed with a Logiq-9 US system (General Electric Healthcare, Waukesha, WI) using M12L linear array transducer. B-mode grayscale scanning was performed at a frequency setting of 10MHz using a maximum number of 8 transmit focal zones. Each session began with a radiologist performing a 3D freehand US scan across the breast to confirm the region of interest. All automated whole breast ultrasound (ABU) scans were performed with prior assessment of location of the mass and information including pathology and conventional mammograms. The patient was then positioned (Figure 4.1), with her breast between the top compression paddle, a TPX

plate (poly-methyl pentene), and the bottom supporting plate. The US transducer was positioned in a mechanical arm with the face of the transducer sliding just above the curved TPX plate. Proper coupling between the US transducer and the TPX plate was achieved with water for CC views and coupling gel for others. A viscous, bubble-free US gel (LithoClear, Sonotech Inc., Bellingham, WA) was applied on and around the breast in order to reduce the air-gap between the breast periphery and the plate. Furthermore, a biocompatible mild adhesive spray (Got2b glued spiking spray, Advanced Research Laboratories, Costa Mesa, CA) stabilized the compressed breast while providing reasonable acoustic coupling between the top plate and breast. The patient was seated comfortably throughout the scan to minimize motion artifacts.

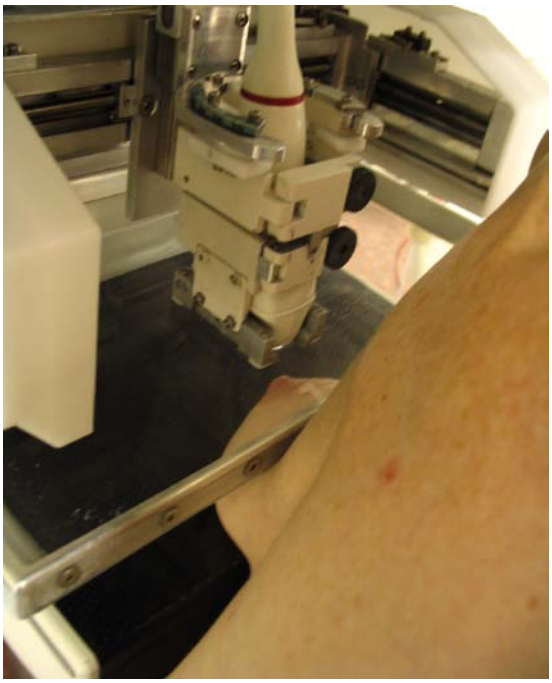

Figure 4.1: View of the breast under mammography-style compression with the automated ultrasound scanning apparatus. The transducer holder was spring-loaded in a frame attached to the paddle and moved on Teflon feet keeping the transducer lens just above the compression plate with the transducer following the paddle surface. The patient was rotated from a position of best coverage and the breast was not gelled to allow for better photography in this system where the protective cowling partially obstructs the view.

The translation motion of the transducer was performed in the elevational direction across the compressed breast (medial-lateral or lateral-medial in cranio-caudal views) under computer control. 3D grayscale US volumetric data was obtained from an elevational scan across 12 to 13 cm of compressed breast and stored in the cine loop buffer of the US system. The US system was modified to perform image acquisition by

input trigger sent from the computer. These methods and the effect of using a compression plate for US scanning were previously published.[47, 48, 49]

One to three parallel 39 mm wide automated B-mode US sweeps were performed as needed with 1 cm overlap to cover the entire breast, depending on the shape, size and to the extent allowed by the acoustic coupling. After image acquisition along the slightly curved surface of the compression plate, image data from each sweep was aligned rapidly with that of its neighboring sweep using a 1D cross-correlation technique along the elevation direction in the overlap region of about 10x40x153 mm^3. This helped in obtaining a self-consistent, single image volume covering most of the breast, typically of size 700x389x383 voxels or approximately 70x39x153 mm^3 for a typical two sweep scan.

Nearly whole breast US image volumes were collected on patients undergoing neoadjuvant chemotherapy at three time points: pre-, mid- and post-chemotherapy. In each case, the pre-chemotherapy image volume along with either the mid- or post-chemotherapy image volume were selected for the reader study, depending on the completeness of tumor coverage. If both mid- and post-chemotherapy image volumes were fully covered in a case, the post-chemotherapy image volume was selected for the reader study.

4.2.2 IVBaR on Chemotherapy cases

In this study on lesion volume estimation using IVBaR, we have attempted a non-rigid deformation model based on thin-plate spline (TPS). [50, 51] Miami-Fuse® software, developed by the Digital Image Processing Lab at the University of Michigan[52], uses a TPS based interpolant to maximize the image similarity measure, mutual information (MI).[22,36] This algorithm maximizes the similarity measure of Shannon MI[36,53,54,55] and is easy to use without the need for segmentation, edge enhancement etc.[43] The MI depends on the amount of shared true structural information such as specular reflectors and volumetric scatterers as well as shadowing, other artifacts and deformation of the tissues. Registration of two US image volumes depends in part on the available MI in the image volumes.

IVBaR involved a two-step procedure: i) Affine transformation and ii) Non-rigid transformation. The global alignment of the reference and the homologous image volumes was performed using 3D full affine transformation which included translation, rotation, scaling and shear.[56, 57] Ordered pairs of at least 4 and no more than 8 control points, with at least 1 out of plane, were manually selected at corresponding locations in the two 3D image volumes to establish initial correspondence. Automated assignment of control points were tested, but were not very successful because of the speckle noise, angle dependence of acoustic back scatter and large distortions of the breast. The algorithm utilizes a simplex optimization by iteratively moving the positions of the control points in the homologous image volume subject to maximizing the resulting MI between the two image volumes.[58] All other voxels were moved and interpolated using the above transform until the MI was maximized. The grayscale image value at each voxel location in the homologous image was computed by trilinear interpolation of its eight nearest neighbors.

There were many situations where affine registration techniques are not sufficient to achieve alignment of anatomy. Additional transformation was required for modeling local deformation of the breast that varied significantly across patients and with age. Using the rigid transformation as the initial estimate, a non-rigid transformation was performed by modeling the deformation of the reference image into the target image as an elastic physical process. [59, 60] Ordered pairs of N_c control points were manually selected at presumed corresponding locations in the two 3D volumes to establish initial correspondence. The locations of control points in the homologous image volume were moved incrementally by the algorithm and the locations of other voxels were interpolated using the TPS. [61, 62] The algorithm worked by iteratively moving the control points in the homologous image volume until MI was maximized.[63, 64, 65, 66] A multi-resolution approach was used in the registration process with a downsizing factor of 0.25–0.5 in all three axes. This strategy assured a smooth global to local deformation, reduced the chance of the control points falling into local minima, thus keeping the registration process robust and less time consuming.[67, 68] Note that the transformation model was dependent on the operators positioning and distribution of the fiducials in both the image volumes and was dependent on the operator's skill and patience.

4.2.3 Reader study

The three breast radiologists were presented with these images and a report:

- Pre-chemotherapy mammogram(s),
- Pre-chemotherapy US hand scan(s),
- Clinical findings report without tumor size information and
- Automated whole breast ultrasound (ABU) image volume of pre-chemotherapy along with mid- or post-chemotherapy ABU image volume, presented in a pseudo-random order with and without IVBaR.

After a mean gap of 46 days (maximum = 158 days), the reader repeated the reading with IVBaR. The outline of tasks performed independently by each of the three breast ultrasound radiologists is shown in Figure 4.2. The tumor boundary was marked by the reader by placement of a 3D ellipsoid around the region of interest (ROI), as shown in Figure 4.3. In general any ellipsoid is a unit sphere at the origin that has been scaled, rotated, and translated in three axes. Therefore, all ellipsoids can be specified by a subset

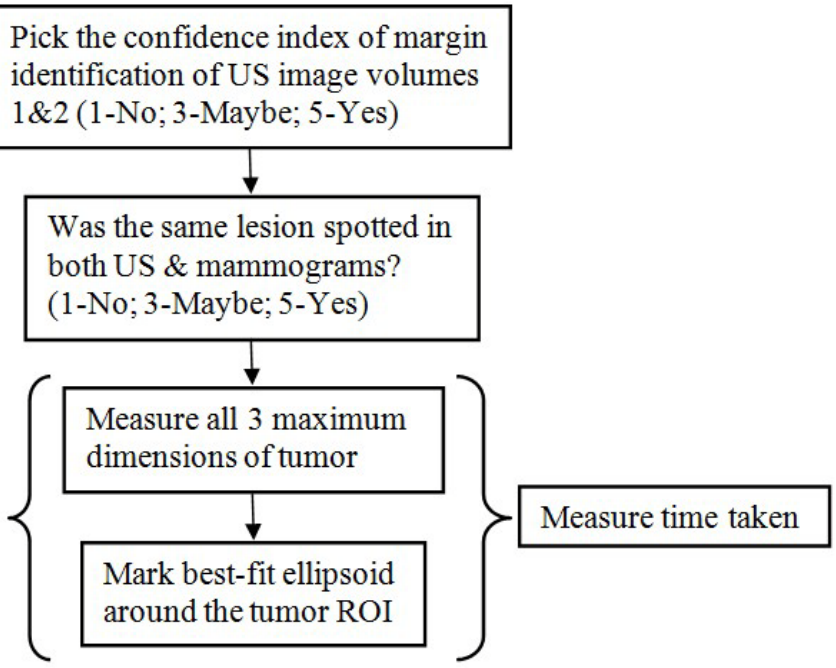

Figure 4.2: Block diagram showing outline of tasks performed in the reader study consisting of 3 breast radiologists. Apart from noting the confidence indices for indentifying the tumor boundary and similarity of lesion between ABU and mammogram, time taken to mark the boundary of tumor in ABU scan pairs (with or without image registration) was also recorded.

of the 4x4 transformation matrixes. Using Osirix© as the main visualization platform[69], a plug-in module was developed using VTK (Visualization Toolkit, Kitware Inc., Clifton Park, NY), to render a 4x4 transformation overlaid on the 3D ultrasound data as a semitransparent ellipsoid. This transform could be easily manipulated using standard VTK controls to give the user a quick method of producing ellipsoidal ROIs.

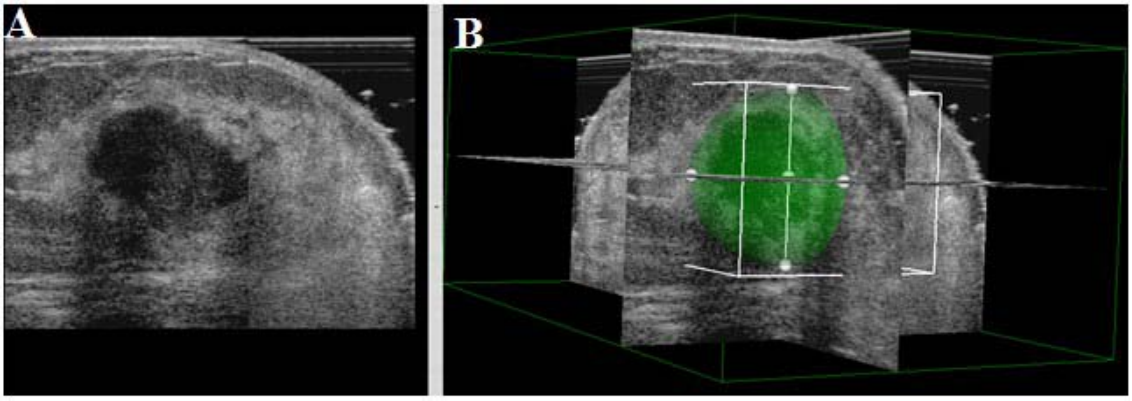

Figure 4.3: (A) Shown here is the 2D center slice of image volume with lobulated, nodular mass and calcifications. (B) Radiologist drawn best-fit ellipsoid shown in green color bound within white margins around the mass. Graphical user interface software was developed in our lab using VTK in Osirix©.

By overlaying the ellipsoids from the three readers, the core hypo-echoic region of the tumor could be identified from the intersection of the three ellipsoids while the outer zone of possible tumor tissue was identified from their union. The ratio of volume of intersection to volume of union was measured on every image volume pair with and without IVBaR. The total time taken to measure the 3 maximum, approximately orthogonal dimensions as well as to mark the tumor boundary was noted for each image volume. Regression analysis was performed on the volume of tumor as well as the time taken from all the readers.

4.3 Results

The three radiologists agreed on the complete visibility of the tumor region in 3D-US image volume pairs in the 6 patient cases. Identifying the tumor is impaired by accuracy in often very indistinct tumor margins, shadowing of the mass and ellipsoid is only an approximation as tumor can have extremely irregular geometric shape.

Shown in Figure 4.4 is an example 2D US image of a subject with a lobulated, nodular mass with calcifications and confirmed as cancer by biopsy. Shown in the top 3 images are the markings of tumor boundary at the center slice of the ellipsoids by the 3 readers while the bottom image shows all the 3 boundaries.

Comparing the use and non-use of IVBaR, the results were:

- A significant reduction in time taken to mark the tumor boundary averaged between readers from 8.2 min to 5.6 min ($p<0.03$)
- An insignificant increase in mean ratio of volumes of intersection to union of ellipsoids between readers from 0.13 to 0.18 across cases ($p<0.15$)
- An insignificant decrease in mean of standard deviation in measuring NFV_{ijs} between readers from 7.2 to 2.2 across cases ($p<0.2$)

  Vpre and Vpost refers to ellipsoid volume pre- and post-chemotherapy

  The fractional change in volume of i'th case by j'th reader in state, s=u for unregistered or r for registered is FV_{ijs} = (Vpost - Vpre)/Vpre

  Normalized fractional volume change = NFV_{ijs} = FV_{ijs} / (mean FV_{is} between readers)

4.4 Conclusion

IVBaR used to aid identification of breast tumor boundaries in 3D US image stacks has shown potential for clinical utility in terms of time needed to mark lesions in mid- or post-chemotherapy image volumes (Results 1). When viewing pairs of image stacks, there were insignificant reductions in the variances between readers in assessing the location of the post-chemotherapy lesion margins (Result 2) and the fractional tumor volume change (Result 3). A module based on VTK provided an easy way to place and manipulate ellipsoid around tumor.

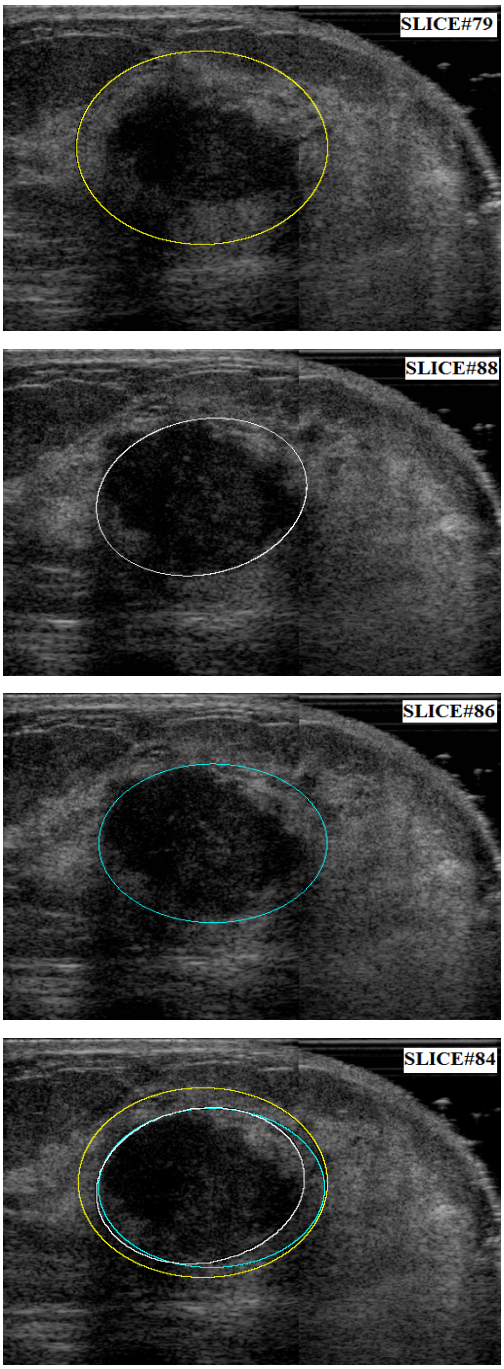

Figure 4.4: Lobulated nodular mass (Top 3) 2D US image of center-slice of US image volumes with ellipsoids marked around the tumor region by the 3 readers. (Bottom) 2D US image with all 3 tumor boundary markings in the center slice of the ellipsoid.

4.5 Acknowledgements

I would like to thank Drs. Marilyn Roubidoux, Jie Li and Annette Joe from the Department of Radiology, University of Michigan Health System for their time and effort as readers. I would also like to thank Aaron Moskalik for developing software for placement of 3D ellipsoid around the tumor boundary. This work was supported in part by U.S. Public Health Service grants PO1 CA87634 and RO1 CA91713 (a partnership with GE Global Research).

4.6 References

1 G Bonadonna, P Valagussa, C Brambilla, L Ferrari, A Moliterni, M Terenziani, M Zambetti, "Primary chemotherapy in operable breast cancer: Eight-year experience at the Milan Cancer Institute," J. Clin. Oncol. 16, 93–100, 1998.

2 B Fisher, A Brown, E Mamounas, S Wieand, A Robidoux, RG Margolese, AB Cruz Jr, ER Fisher, DL Wickerham, N Wolmark, A DeCillis, JL Hoehn, AW Lees, NV Dimitrov, "Effect of preoperative chemotherapy on local-regional disease in women with operable breast cancer: Findings from National Surgical Adjuvant Breast and Bowel Project B-18," J. Clin. Oncol. 15, 2483–2493, 1997.

3 SM Scholl, A Fourquet, B Asselain, JY Pierga, JR Vilcoq, JC Durand, T Dorval, T Palangié, M Jouve, P Beuzeboc, E Garcio-Giralt, RJ Salmon, A de la Rochefordière, F Campana, P Pouillart, "Neoadjuvant versus adjuvant chemotherapy in premenopausal patients with tumors considered too large for breast conserving surgery: Preliminary results of a randomized trial," Eur J Cancer 30, 645–652, 1994.

4 C Balu-Maestro, C Chapellier, A Bleuse, I Chanalet, C Chauvel and R Largillier, "Imaging in evaluation of response to neoadjuvant breast cancer treatment benefits of MRI," Breast Cancer Res Treat 72:145, 2002.

5 G von Minckwitz, SD Costa, W Eiermann, J Blohmer, AH Tulusan, C Jackisch, M Kaufmann, "Maximized reduction of primary breast tumor size using preoperative chemotherapy with doxorubicin and docetaxel," J. Clin. Oncology 17(7), 1999–2005, 1999.

6 K Shin, S Moon, J Suh, W Yang, "Tumor volume change as a predictor of chemotherapeutic response in osteosarcoma," Clinical Orthopedics and related research 376, 200–208, 2000.

7 SC Partridge, JE Gibbs, Y Lu, "MRI measurements of breast tumor volume predict response to neoadjuvant chemotherapy and recurrence-free survival," Am. J. Roentgenol 184, 1774–1781, 2005.

8 C Boetes, RD Mus, R Holland, JO Barentsz, SP Strijk, T Wobbes, JH Hendriks, SH Ruys, "Breast tumours: comparative accuracy of MR imaging relative to mammography and US for demonstrating extent," Radiology 197, 743–747, 1995.

9 MA Helvie, LK Joynt, RL Cody, LJ Pierce, DD Adler, SD Merajver, "Locally advanced breast carcinoma: accuracy of mammography versus clinical examination in the prediction of residual disease after chemotherapy," Radiology 198(2): 327–32, 1996.

10 L Pierce, D Adler, M Helvie, A Lichter, S Merajver, "The use of mammography in breast preservation in locally advanced breast cancer," Int. J. Radiation Oncology Biol. Physics 334: 571–7, 1996.

11 DB Kopans, "The positive predictive values of mammography," Am. J. Roentol. 158, 521–526, 1992.

12 WA Berg, JD Blume, JB Cormack, EB Mendelson, D Lehrer, M Bohm-Velez, ED Pisano, RA Jong, WP Evans, MJ Morton, MC Mahoney, LH Larsen, RG Barr, DM Farria, HS Marques, K Boparai, "Combined screening with ultrasound and mammography vs mammography alone in women at elevated risk of breast cancer," J. Am. Med. Assoc. 299(18), 2151–2163, 2008.

13 WA Berg, "Rationale for a trial of screening breast ultrasound," Am. J. Radiol. 180, 1225–1228, 2003.

14 AR Padhani, JE Husband, "Dynamic contrast-enhanced MRI studies in oncology with an emphasis on quantification, validation and human studies," Clinical Radiol. 56, 607–620, 2001.

15 LW Bassett, C Kimme-Smith, "Breast sonography," Am. J. Roentgenol. 156, 449–455, 1991.

16 SV Hilton, GR Leopold, LK Olson, SA Willson, “Real-time breast sonography: application in 300 consecutive patients,” Am. J. Roentgenol. 147, 479–486, 1986.
17 VP Jackson, “The current role of US in breast imaging,” Radiol. Clin. North Am. 33, 1167–1170, 1995.
18 TM Kolb, J Lichy, JH Newhouse, “Occult cancer in women with dense breasts: Detection with screening US- Diagnostic yield and tumour characteristics,” Radiology 207, 191–199, 1998.
19 KJW Taylor, C Merritt, C Piccoli, “Ultrasound as a complement to mammography and breast examination to characterize breast masses,” Ultras. Med. Biol. 28(1), 19–26, 2002.
20HA Moss, PD Britton, CDR Flower, AH Freeman, DJ Lomas, RML Warren, “How reliable is modern breast imaging in differentiating benign from malignant breast lesions in the symptomatic population?,” Clin. Radiol. 54, 676–682, 1999.
21 AT Stavros, D Thickman, CL Rapp, MA Dennis, SH Parker, GA Sisney, “Solid breast nodules: Use of sonography to distinguish between benign and malignant lesions,” Radiology 196, 123–134, 1995.
22 WA Berg, “Rationale for a trial of screening breast ultrasound: American college of radiology imaging network (acrin) 6666,” American Journal of Roentgenology, 180(5): p. 1225–1228, 2003.
23 VP Jackson, “The role of US in breast imaging,” Radiology 177, 3051, 1990.
24 SM Durfee, DLG Selland, DN Smith, SC Lester, CM Kaelin, JE Meyer, “Sonographic evaluation of clinically palpable breast cancers invisible on mammography,” The Breast Journal 6, 247–51, 2000.
25 FW Conway, CW Hayes, WH Brewer, “Occult Breast masses: Use of a mammographic localization grid for US evaluation,” Radiology 181,143–146, 1991.
26 MB Barton, R Harris, SW Fletcher, “Does this person have Breast Cancer? The screening clinical breast examination: Should it be done? How?,” J. Am. Med. Assoc. 282(13), 1270–1280, 1999.
27 JS Michaelson, M Silverstein, J Wyatt, G Weber, R Moore, E Halpern, DB Kopans, K Hughes, “Predicting the survival of patients with breast carcinoma using tumor size,” Cancer 95, 713–723, 2002.
28 CL Carter, C Allen, DE Henson, “Relation of tumor size, lymph node status, and survival in 24,740 breast cancer cases,” Cancer 63(1), 181–187, 1989.
29 AB Miller , B Hoogstraten, M Staquet, A Winkler, “Reporting results of cancer treatment,” Cancer 47, 207–214, 1981.
30 JV Watson, “What does “response” in cancer chemotherapy really mean?,” Br. Med. J., 283, 34–37, 1981.
31 MA Roubidoux, GL Le Carpentier, JB Fowles, B Bartz, D Pai, SP Gordon, AFSchott, TD Johnson, PL Carson, “Sonographic evaluation of early-stage breast cancers that undergo neoadjuvant chemotherapy,” J. Ultras. Med. 24, 885–895, 2005.
32 AB Chagpar, LP Middleton, AA Sahin, P Dempsey, AU Buzdar, AN Mirza, FC Ames, GV Babiera, BW Feing, KK Hunt, HM Kuerer, F Meric-Bernstam, MI Ross, SE Singletary, “Accuracy of physical examination, ultrasonography, and mammography in predicting residual pathologic tumor size in patients treated with neoadjuvant chemotherapy,” Ann. Surg. 243, 257–64, 2006.
33 T Nakamura, T Fukutomi, H Tsuda, S Akashi-Tanaka, K Matsuo, C Shimizu, K Miyakawa, “Changes in finds of mammography, ultrasonography and contrast-induced computed tomography of three histological complete responders with primary breast cancer before and after neoadjuvant chemotherapy: case reports,” Jpn. J. Clin. Oncol. 30, 453–457, 2000.
34 P Bellia, M Costantinia, C Malaspinaa, A Magistrellia, G LaTorreb, L Bonomoa, “MRI accuracy in residual disease evaluation in breast cancer patients treated with neoadjuvant chemotherapy,” Clin. Rad. 61(11), 946–953, 2006.

35 CR Meyer, JL Boes, B Kim, PH Bland, GL LeCarpentier, JB Fowlkes, MA Roubidoux, PL Carson, “Semiautomatic Registration of Volumetric Ultrasound Scans,” Ultras. Med. Biol. 25(3), 339–347, 1999.
36 CR Meyer, JL Boes, B Kim, PH Bland, KR Zasadny, PV Kison, K Koral, KA Frey, RL Wahl, “Demonstration of accuracy and clinical versatility of mutual information for automatic multimodality image fusion using affine and thin-plate spline warped geometric deformations,” Med Image Anal 1:195–206, 1997.
37 PL Carson, GL LeCarpentier, MA Roubidoux, RQ Erkamp, JB Fowlkes, MM Goodsitt, Physics and Technology of Ultrasound Breast Imaging Including Automated 3D, in, A Karellas and ML Giger, eds, 2004 Syllabus, Advances in Breast Imaging: Physics, Technology, and Clinical Applications, RSNA Categorical Course in Diagnostic Radiology Physics, RSNA, 223–232, 2004.
38 CR Maurer, JM Fitzpatrick, “A review of medical image registration,” Proc. Interactive Image-guided Neurosurgery, 17–44, 1993.
39 PJ Edwards, DLG Hill, JA Little, DJ Hawkes, “A three-component deformation model for image-guided surgery,” Med. Image Anal. 2(4), 355–367, 1998.
40 JG Rosenman, EP Miller, G Tracton, TJ Cullip, “Image registration: An essential part of radiation therapy treatment planning,” Int. J. Radiat. Oncol. Biol. Phys. 40(1), 197–205, 1998.
41 J Weese, GP Penney, P Desmedt, TM Buzug, DLG Hill, “Voxel based 2D/3D registration of fluoroscopy images and CT scans for image guided surgery,” IEEE Trans. Information Tech Biomedicine 1(4), 284–293, 1997.
42 ERE Denton, LI Sonoda, D Rueckert, SC Rankin, C Hayes, MO Leach, DLG Hills, DJ Hawkes, “Comparison and evaluation of rigid, affine, and non-rigid registration of breast MR images,” J. Computer Assisted Tomography 23(5), 800–805, 1999.
43 CR Meyer, JL Boes, B Kim, PH Bland, KR Zasadny, PV Kison, K Koral, KA Frey, RL Wahl, “Demonstration of accuracy and clinical versatility of mutual information for automatic multimodality image fusion using affine and thin plate spline warped geometric deformations,” Med. Image Anal. 1(3), 195–206, 1997.
44 J. Krücker, Ph.D Thesis (pp. 45), Applied Physics Program, University of Michigan, 2003.
45 J-P. Thirion, G Calmon, “Deformation analysis to detect and quantify active lesions in 3D medical image sequences,” IEEE Trans. Med. Img. 18(5), 429–441, 1999.
46 G Narayanasamy, GL LeCarpentier, MA Roubidoux, JB Fowlkes, PL Carson, “Spatial registration of temporally separated whole breast 3D ultrasound images,” Med Phys 36(9), 4288–4300, 2009.
47 SP Sinha, MM Goodsitt, MA Roubidoux, RC Booi, GL LeCarpentier, CR Lashbrook, KE Thomenius, CL Chalek, PL Carson, “Automated Ultrasound Scanning on a Dual-Modality Breast Imaging System,” J. Ultrasound Med. 26, 645–655, 2007.
48 G Narayanasamy, JB Fowlkes, OD Kripfgans, JA Jacobson, M. De Maeseneer, R. M. Schmidt, P. L. Carson, “Ultrasound of the finger for human identification using biometrics,” Ultras. Med. Biol. 34(3), 392–399, 2008.
49 PL Carson, GL LeCarpentier, MA Roubidoux, RQ Erkamp, JB Fowlkes, MM Goodsitt, “Physics and Technology of Ultrasound Breast Imaging Including Automated 3D,” in A Karellas and ML Giger, eds, 2004 Syllabus, Advances in Breast Imaging: Physics, Technology, and Clinical Applications, RSNA Categorical Course in Diagnostic Radiology Physics, RSNA, 223–232 in 2004.
50 LS Brown, “A Survey of Image Registration Techniques,” ACM Computing Surveys 24(4), 325–356, 1992.
51 B Zitova, J. Flusser, “Image registration methods: a survey,” Image and Vision Computing 21, 977–1000, 2003.

52 http://www.dipl.rad.med.umich.edu/
53 PA Viola, “Alignment by maximization of mutual information,” Ph.D. dissertation, Massachusetts Inst. Technol., Cambridge, MA, 1995.
54 A Collignon, F Maes, D Delaere, D Vandermeulen, P Suetens, G Marchal, “Automated multimodality image registration using information theory,” Proc. Information Processing in Medical Imaging (1995), 263–274 (1995).
55 A Moskalik, PL Carson, CR Meyer, JB Fowlkes, JM Rubin, MA Roubidoux, “Registration of 3D compound ultrasound scans of the breast for refraction and motion correction,” Ultras. Med. Biol. 21(6), 769–778, 1995.
56 PH Schönemann, “A generalized solution of the orthogonal procrustes problem,” Psychometrika 31, 1–10 (1966).
57 D Rueckert, LI Sonoda, C Hayes, DLG Hill, MO Leach, DJ Hawkes, “Nonrigid registration using free-form deformations: application to breast MR images,” IEEE Trans. Med. Imaging 18(8), 712–721, 1999.
58 WH Press, SA Teukolsky, WT Vetterling, BP Flannery, “Numerical Recipes in C-The Art of Scientific Computing,” Second Edition, Cambridge University Press, Cambridge (1992)
59 R Bajcsy, S Kovacic, “Multiresolution elastic matching,” Computer Vision, Graphics and Image Processing, 46, 1–20, 1989.
60 C Davatzikos, “Spatial transformation and registration of brain images using elastically deformable models,” Comput. Vis. Image Understand., 66, 207–222, 1997.
61 H Park, PH Bland, KK Brock, CR Meyer, “Adaptive registration using local information measures” Med Image Analysis 8, 465–473, 2004.
62 G Xiao, JM Brady, JA Noble, M Burcher, R English, “Nonrigid Registration of 3-D Free-Hand Ultrasound Images of the Breast,” IEEE Trans Med Imaging, 21(4): 405–412, 2002.
63 HH Johnson, G Christensen, “Landmark and Intensity-based, consistent thin plate spline image registration,” IPMI 2082, 329–343, 2001.
64 FL Bookstein, “Morphometric Tools for Landmark Data” Cambridge University Press, Cambridge, 1991.
65 FL Bookstein, “Shape and information in medical images: a decade of morphometric synthesis” Computer Vision and Image Understanding 66, 97–118, 1997.
66 W Wells, P Viola, H Atsumi, S Nakajima, R Kikinis, “Multi-modal volume registration by maximization of mutual information,” Med. Image Anal. 1(1), 35–51, 1996.
67 R Shekhar, V Zagrodsky, “Mutual Information-based rigid and non-rigid registration of ultrasound volumes,” IEEE Trans. Med. Imaging 21(1), 9–22, 2002.
68 JPW Pluim, JBA Maintz, MA Viergever, “Mutual information matching in multiresolution contexts,” Image Vision Computing 19, 45–52, 2001.
69 http://www.osirix-viewer.com/

CHAPTER 5 ESTIMATION OF VOLUME CHANGES IN IDENTIFIED BREAST LESION PHANTOMS WITHOUT SEGMENTATION

5.1 Introduction

Breast ultrasound (US) scans are currently performed free hand by radiologists or technologists using two-dimensional (2D) real time systems. Physical palpation is used to study the breast qualitatively for lesion shape, size, location and firmness. Furthermore, depending on the technique employed, these methods are sensitive to machine settings and dependent on both the observer and interpreter.[1] Visual comparisons of scan images have been used to assess qualitative changes during the course of treatment because of its importance in gauging the effectiveness of treatment in patients undergoing therapy for malignant tumors. Estimating the volume of lesion before or after treatment (including chemotherapy of breast lesions) has been a challenge mainly because of the ill-defined boundary surrounding these lesions. There are many treatment procedures that alter a lesion from its original shape and size.

In this study, we propose to estimate lesion volume change by utilizing information associated with the structure surrounding the lesion i.e., outside the identified region of interest (ROI) using an Image Volume Based Registration (IVBaR) technique. The IVBaR algorithm used here involves a statistical technique that has been shown to work very well in spatial alignment of the image volumes.[2] The spatially aligned images can be visualized in the same coordinate system, facilitating easier comparison. Miami-Fuse© software uses an interpolant based on a thin plate spline method to maximize the similarity between the images via maximization of mutual information.[3] The three-

dimensional (3D) image volume acquired at time T1 is transformed to the 3D image volume acquired at time T2 (e.g., post-treatment) by registration. The volume estimation from the transformation parameters involves the calculation of a Jacobian (described later) and comparisons to the known volumes have been made.

5.2 Methods and Materials

5.2.1 Setup

The urethane breast biopsy phantom (Model: ATS BB-1 phantom, ATS Laboratories, CT 06608, USA) used for the studies has uniform echogenicity throughout, except at places where cystic and solid-like tissue-mimicking target structures are present. This phantom will be referred to as the less structured phantom. In order to add more cyst-like structures, polyacrylamide gel of different shapes and sizes was injected in the original phantom at various positions resulting in a phantom that will be referred to as the more structured phantom. Polyacrylamide gel was prepared from bis-acrylamide 30% solution (Sigma-Aldrich, MO 63103, USA) diluted to 7.5% with de-ionized water and degassed before adding 10% ammonium per-sulphate and tetra-methylenediamine. In order to increase available structures even further, a similar procedure was repeated on the pork loin tissue. A balloon catheter (outer diameter of 6 French size or 2 mm) was inserted into each of these three phantoms. Known volumes of saline were injected into the catheter to mimic lesions of varying sizes. The phantom was scanned by US with the balloon volumes ranging from 0.5 to 2.5 cc in 0.5 cc increments. The system settings and all other parameters were maintained throughout this study.

The phantom was then positioned in the 3D US scanning assembly between compression paddles, over which a GE M12L linear array (General Electric Medical Systems, Milwaukee, WI) was translated by a two axis positioning system.[4] The top compression paddle is a TPX plate (made of 4-methylpentene-1 based polyolefin) of 2.5 mm thickness used for imaging the breast with the same geometry as mammography, as seen in Figure 5.1. Imaging properties for the compression plate and the associated US system are described elsewhere.[5,6] Scans were performed in cranial-caudal (CC) view by

translating the transducer in the elevation direction across the phantom (medial-lateral or lateral-medial) and acquiring 2D images at 0.4 mm frame spacing. Coupling between the transducer and the paddle was achieved with water as the coupling agent. To prevent slippage and provide bubble-free coupling between the paddle and the phantom, the gap was filled with a bubble-free ultrasound gel (LithoClear, Sonotech, Bellingham, WA). These methods and other hardware and software interfaces were developed to perform automated scanning and to send triggers to a GE Logiq-9 system for data acquisition.[7,8]

Scanning was performed on the GE Logiq9 using M12L linear array (General Electric Medical Systems, Milwaukee, WI) with a transmission frequency of 10MHz for grayscale and compound imaging. The seven angles used for compounding were ±6°, ±9° and ±12° along with the reference image at 0°.

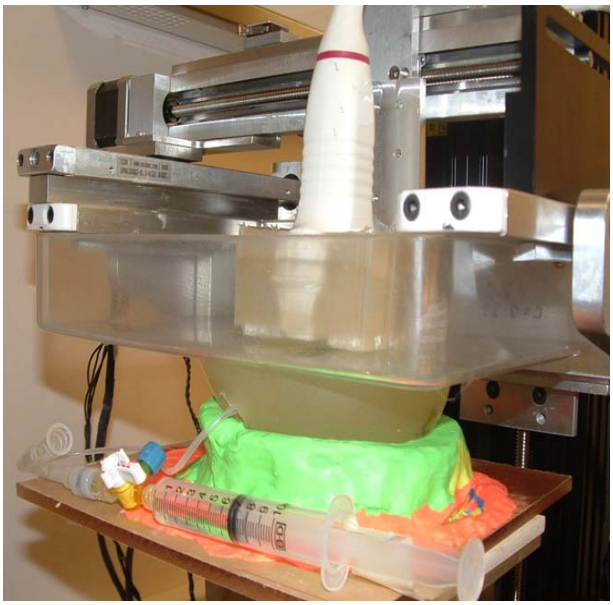

Figure 5.1: Experimental setup – Breast phantom with balloon catheter (and syringe) being scanned via a thin TPX plate using GE Logiq 9's M12L linear probe inserted in its holder on top of the two-axis probe positioning system.

5.2.2 IVBaR on phantom data

Registration performed using MIAMI-Fuse®, works by maximizing the similarity measure of Shannon mutual information (MI).[9,10] The procedure adopted is to draw an ROI that encompasses the lesion from the reference image and remove the contribution

of the lesion from the registration by setting the pixel intensity value within the ROI to 0. The 3D image with a catheter volume of 1.5 cc was identified as the reference image and a hypo-echoic ROI which encompassed the catheter along with its boundary were zeroed out, as shown in Figure 5.2. The 3D US images with 0.5 cc, 1.0 cc, 2.0 cc and 2.5 cc of injected saline volume were used as target 3D image (referred later as homologous 3D image). The reference 3D image was registered with each one of the target 3D images.

IVBaR involved a two step procedure. The global alignment of the reference and the homologous 3D images were performed using a 3D full affine transformation which included translation, rotation, scaling and shear. Ordered pairs of at least 4 and no more than 8 control points (with at least 1 out of plane) were manually selected at corresponding locations in the two 3D images to establish initial correspondence. In the second step, a 3D rectangular grid of control points was placed outside the selected ROI in the reference image in order to track the location shifts just outside the ROI. Non-rigid

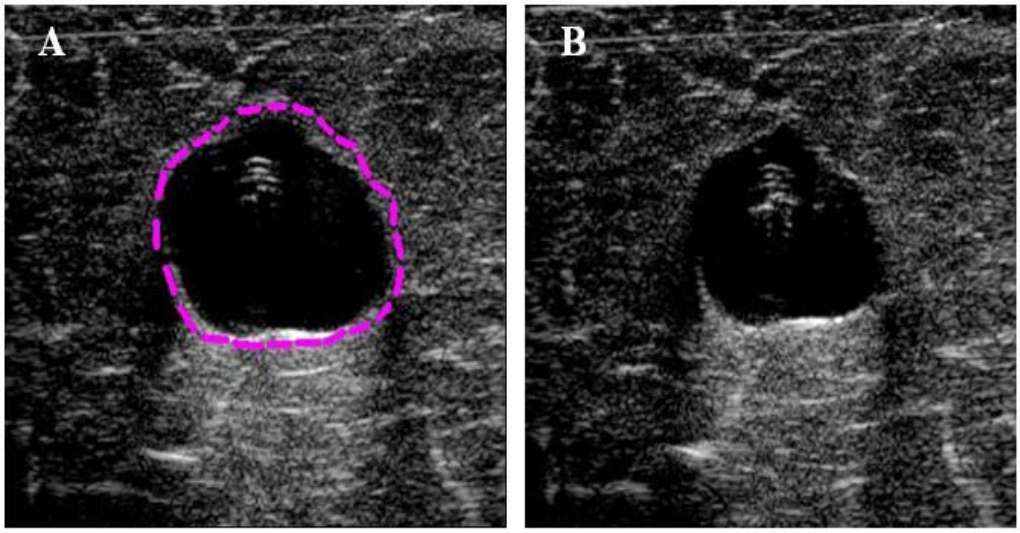

Figure 5.2: 2D US images of the pork loin tissue with balloon catheter containing saline of volumes 1.5 cc (left) and 1.0 cc (right). Notice the hypo-echoic boundary marked roughly using the ROI in the reference image on the left. The information within the ROI is not used in the registration process. Manually selected control points outside the ROI in reference 3D image and at corresponding locations in the homologous 3D image tracked the movement of surrounding tissue.

warping registration was performed to take into account local deformations using thin plate spline (TPS) interpolation of region surrounding the control points. [11] The algorithm works by iteratively moving the control points in the homologous image 3D image using the Nelder/Mead downhill simplex optimization until MI is maximized. [12, 13] The

computational time depended on the size of reference 3D image and the number of control points (N_c). The size of a typical 3D image was 350x350x150 pixels and the mean number of control points N_c needed was 50. A downsizing factor in all three axes of 0.25–0.5 was also employed during the registration process, referred to as the multi-resolution approach.[14]

5.2.3 Volume estimation

At a given point, the Jacobian of a function provides important information about its behavior near that location.[15,16] In 3D space, the absolute value of the Jacobian determinant (also called the "Jacobian" for short) gives the volume change factor. Thus, values of $|J|>1$ would mean volume expansion and $0<|J|<1$ would mean volume shrinkage. Using the transformation parameters of spatial image registration, the Jacobian of the transformation was calculated, as described in the block diagram in Figure 5.3.

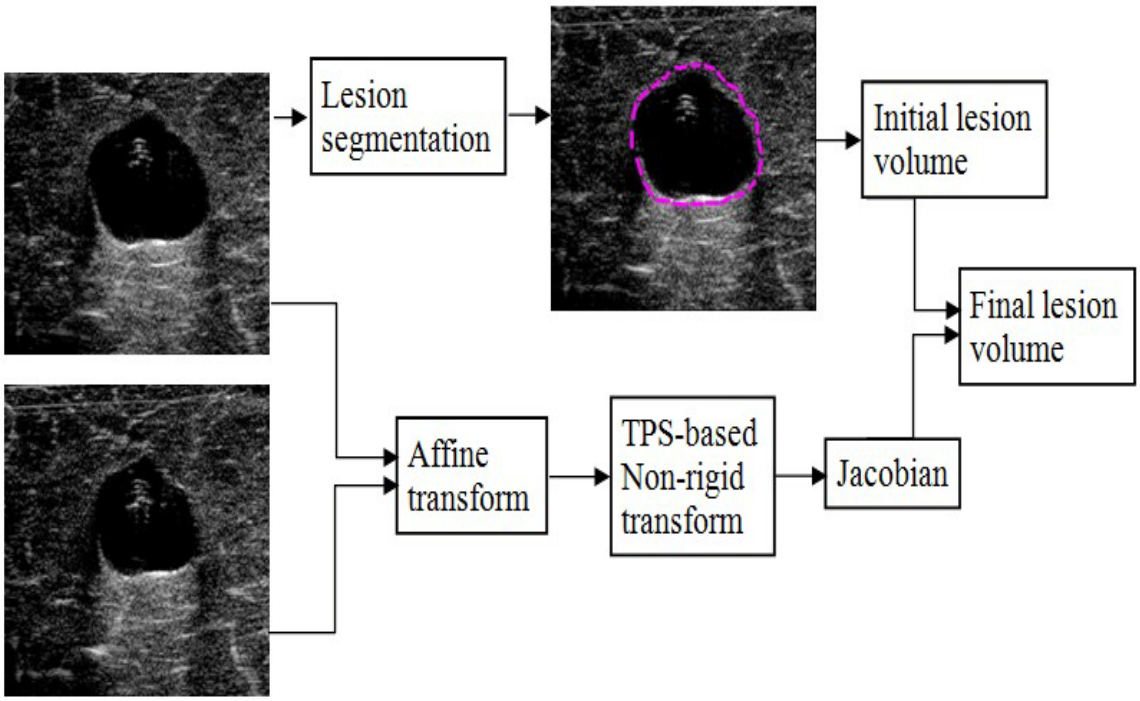

Figure 5.3: Block diagram of Jacobian based lesion volume estimation based on 3D-ultrasound automated image registration.

For transformation f: $f = a_0 + a_1 x + a_2 y + a_3 z + \sum_{i=1}^{n+m} w_i U(|P_i - (x, y, z)|)$

where a_is are the affine coefficients, w_i is the TPS weights, P_i is the reference control points and U(r) =|r| is the TPS basis function in 3D.

The Jacobian at (i, j, k) is given by the determinant:

$$J_{ijk} = \det(\nabla_{i,j,k} f) = \begin{vmatrix} \frac{\partial f_x}{\partial x} & \frac{\partial f_y}{\partial x} & \frac{\partial f_z}{\partial x} \\ \frac{\partial f_x}{\partial y} & \frac{\partial f_y}{\partial y} & \frac{\partial f_z}{\partial y} \\ \frac{\partial f_x}{\partial z} & \frac{\partial f_y}{\partial z} & \frac{\partial f_z}{\partial z} \end{vmatrix}$$

The local volume change estimate in a small region around location (i,j,k) is given by $\delta V'_{ijk} = J_{ijk} \delta V_{ijk}$ where $\delta V'$ is the new voxel volume and δV is the original voxel volume. The final volume estimate is given by: $V' = \sum_{i,j,k \in R} J_{ijk} \delta V_{ijk}$

The initial volume is estimated by summing up the area under the ROI and multiplying by the frame spacing (0.4 mm). The final volume is estimated by multiplying the initial volume with the summed value of the Jacobian of the transformation. A 2D image of the Jacobian is shown in Figure 5.4 along with the deformation grid.

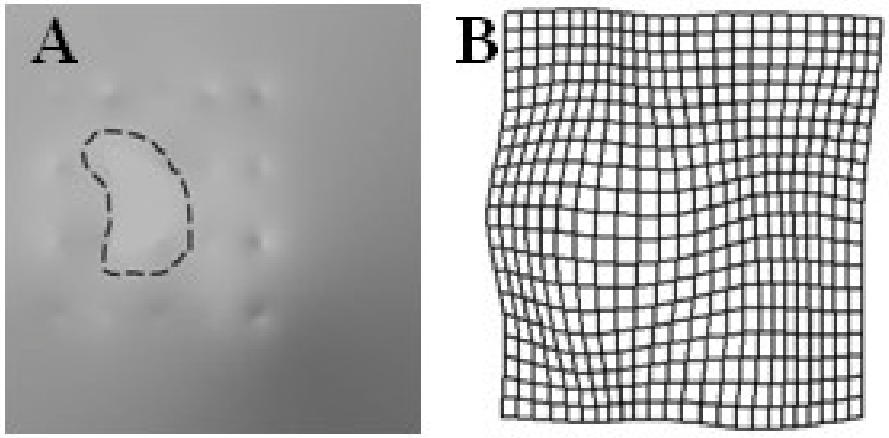

Figure 5.4: (A) 2D Jacobian image of the non-rigid transformation of 1.5 cc lesion mapped onto 2.0 cc lesion. The volume expansion of the catheter mimicking lesion gives a bright region within ROI (shown by the dotted line). This resulted in the movement of surrounding tissues away from the ROI. Notice the intensity fluctuations of the Jacobian image near the control point locations. These fluctuations do not affect the final volume estimate as they are outside the ROI. (B) Shown here is the 2D grid plot of a similar non-rigid transformation.

5.3 Results and Conclusions

IVBaR of 3D grayscale US data of the less structured phantom gave an underestimate of volume change by 79% and an overestimate of the volume by a constant offset of 0.87 cc. In this study, the constant offset volume is defined as the deviation of the best fit estimated volume from the gold standard. In a pilot study, it was found that the offset varies with the reference ROI boundary. A better estimate of the initial volume resulted in a better estimate of the final volume with the constant offset going to 0. In the more structured tissue mimicking phantom results, the volume change estimate was an underestimate of the actual value by 8% with a constant offset of 0.93 cc. In the pork loin tissue phantom results, the estimated volume followed the actual volume closely with a marginal 9% overestimate with a constant offset of 0.28 cc. The estimated and actual changes of volume from the reference image (1.5 cc balloon catheter volume) for the less structured, more structured phantom and pork loin tissue are shown in Figure 5.5 along with correlation coefficient. As IVBaR uses information content and the speckle pattern

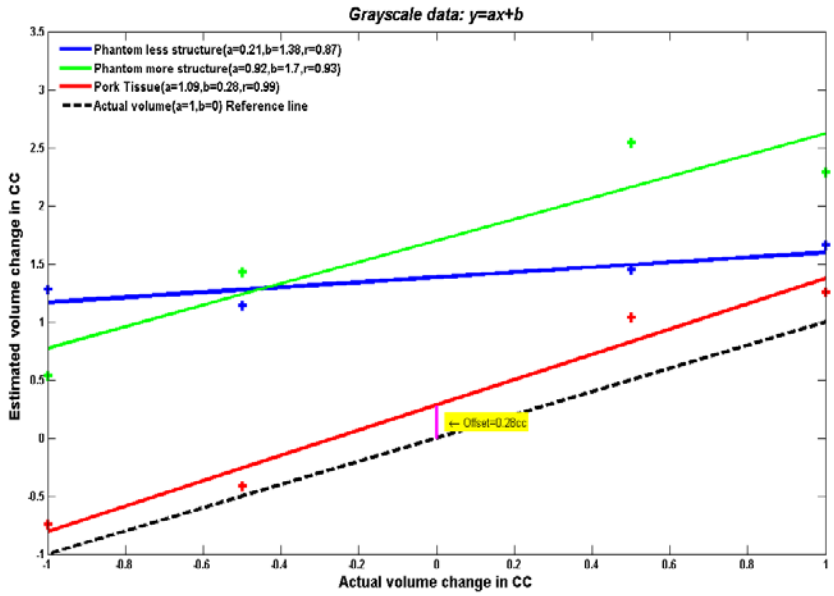

Figure 5.5: Volume estimation by registration of grayscale US 3D image of the less structured phantom, more structured phantom and pork loin tissue. Pork tissue gave accurate estimation at 9% overestimate of volume change with a constant offset of 0.28 cc; more structured phantom gave an 8% underestimate of volume change with a constant offset of 1.7 cc and the less structured phantom gave a large 79% underestimate of volume change with a constant offset of 1.38 cc. Note the Pearson's correlation coefficient (r) for volume estimation of each phantom.

based on the structures, the lack of structures in the two breast phantoms might explain the relatively poor results compared to that for the pork loin. Thus having more structures helps in volume estimation of the lesion via registration.

Volume change was also estimated using the compounded US image data for the same set of phantoms and volumes. Compared with normal B-mode grayscale image volumes, the offset has decreased and the correlation coefficient increased in compound imaging for all the phantoms tested. Figure 5.6 shows the compound and B-mode imaging comparison for the pork loin tissue phantom.

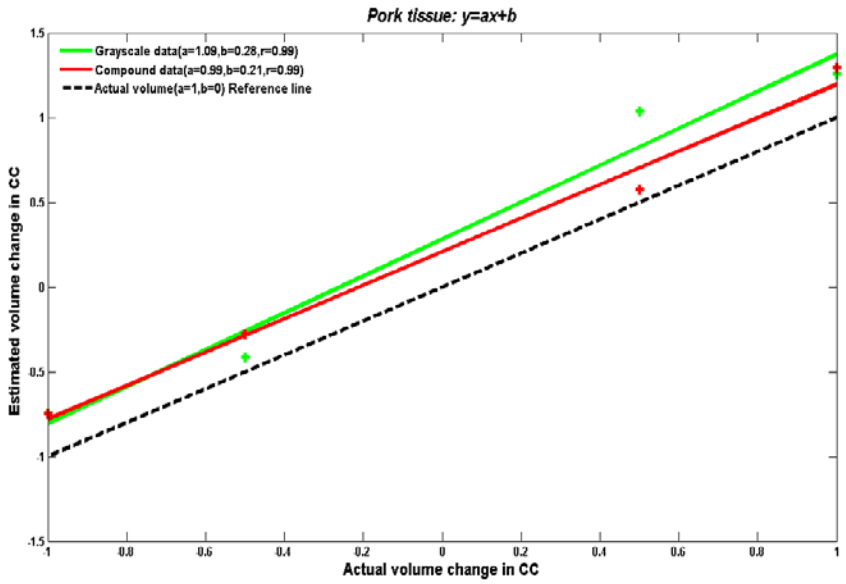

Figure 5.6: Comparing the volume estimation from compounded and grayscale image data of the pork loin tissue phantom. Grayscale image data gave a 9% overestimate of volume change with a constant offset of 0.28 cc while compounded image data gave a marginal 1% underestimate of volume change estimate with a constant offset of 0.21 cc. The Pearson's correlation coefficient (r) for volume estimation is 0.99 for both grayscale and compound 3D images of pork phantom.

In a comparison study between B-mode and compound imaging, the joint histogram plot (scale: 0 to 255) of IVBaR from the pork loin tissue phantom is shown in Figure 5.7(a) and (b), respectively. The joint histogram which is formed only from those parts of the image that overlap with one another shows improved alignment with spatial compound imaging. Thus spatial compounding increases the information content in image volume over B-mode imaging. The volume estimation of the catheter in the pork loin tissue phantom is shown along with the 95% confidence levels in Figure 5.8,

showing that the estimated volume change line is not significantly different from that of the gold standard injected liquid volume in the balloon catheter.

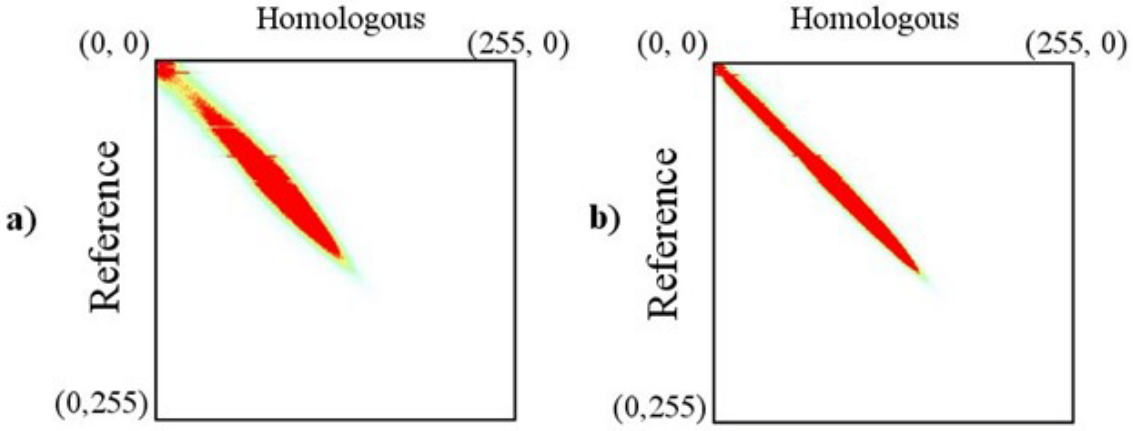

Figure 5.7: Histograms of the transformation of the grayscale image data (a) and the compounded image data (b) for the more structured phantom. The compound view with less speckles helps in registration.

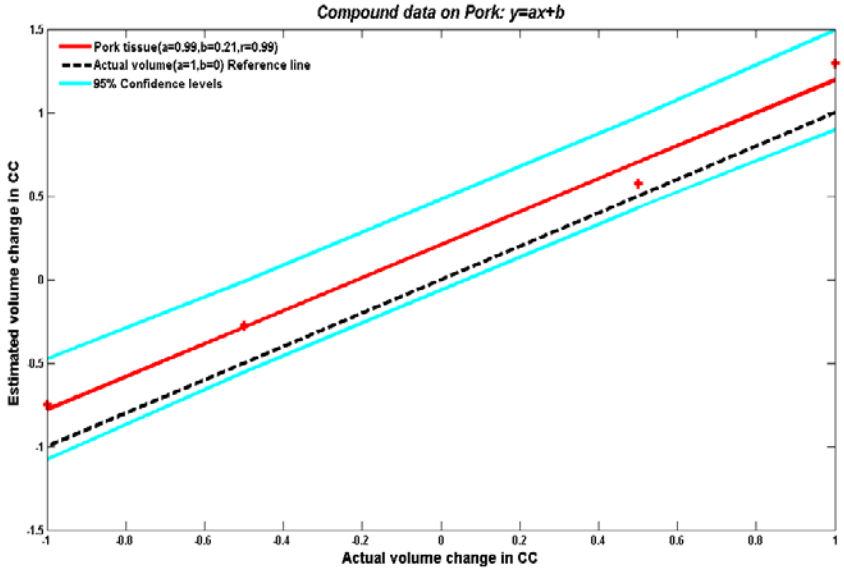

Figure 5.8: Volume estimation on the pork loin tissue phantom from compounded 3D US images compared with the reference volume has 1% underestimate of change and a constant offset of 0.21 cc. Note that the 95% confidence levels are drawn here for reference with the volume estimate.

5.4 Acknowledgements

I would like to thank Ramkrishnan Narayanan for developing software tools. This work was supported in part by U.S. Public Health Service grants PO1 CA87634 and RO1 CA91713 (a partnership with GE Global Research).

5.5 References

1 K Lewit, C Liebenson, “Palpation-problem and implications,” J. Manipulative physiol. Ther. 16(9); 586–590, 1999.

2 PL Carson, G LeCarpentier, MA Roubidoux, RQ Erkamp, JB Fowlkes, MM Goodsitt, Physics and Technology of Ultrasound Breast Imaging Including Automated 3D, in, A Karellas and ML Giger, eds, 2004 Syllabus, Advances in Breast Imaging: Physics, Technology, and Clinical Applications, RSNA Categorical Course in Diagnostic Radiology Physics, RSNA, 2004, 223–232.

3 CR Meyer, JL Boes, B Kim, PH Bland, KR Zasadny, PV Kison, K Koral, KA Frey, RL Wahl, “Demonstration of accuracy and clinical versatility of mutual information for automatic multimodality image fusion using affine and thin-plate spline warped geometric deformations,” Med Image Anal 1997;1:195–206.

4 A Kapur, PL Carson, J Eberhard, MM Goodsitt, K Thomenius, M Lokhandwalla, D Buckley, MA Roubidoux, MA Helvie, RC Booi, GL LeCarpentier, RQ Erkamp, HP Chan, JB Fowlkes, JA Thomas, CE Landberg, “Combination of digital mammography with semi-automated 3D breast ultrasound,” Technol. Cancer Res Treat 3(4):325–334, 2004.

5 RC Booi, JF Krücker, MM Goodsitt, M O’donnell, A Kapur, GL Lecarpentier, MA Roubidoux, JB Fowlkes, PL Carson, “Evaluating thin compression paddles for Mammographically compatible ultrasound,” Ultrasound in Med. & Biol., 33(3): 472–482, 2007.

6 SP Sinha, MM Goodsitt, MA Roubidoux, RC Booi, GL LeCarpentier, CR Lashbrook, KE Thomenius, CL Chalek, PL Carson,"Automated Ultrasound Scanning on a Dual Modality Breast Imaging System," Journal of Ultrasound in Medicine, 26(5), 645:655, 2007.

7 G Narayanasamy, JB Fowlkes, OD Kripfgans, JA Jacobson, M De Maeseneer, RM Schmidt, PL Carson, “Ultrasound of the finger for human identification using biometrics,” Ultras. Med. Biol. 34(3), 392–399, 2008.

8 G Narayanasamy, G LeCarpentier, M Roubidoux, J Fowlkes, AF Schott, PL Carson, "Spatial Registration of Temporally Separated Whole Breast 3D Ultrasound Images," Medical Physics Vol. 36(9), pp. 4288–4300, Sep 2009.

9 CR Meyer, JL Boes, B Kim, PH Bland, GL LeCarpentier, JB Fowlkes, MA Roubidoux, PL Carson, “Semiautomatic Registration of Volumetric Ultrasound Scans,” Ultrasound in Med. & Biol., 25(3): 339–347, 1999.

10 A Moskalik, PL Carson, CR Meyer, JB Fowlkes, JM Rubin, MA Roubidoux, “Registration of 3D compound ultrasound scans of the breast for refraction and motion correction,” Ultrasound in Medicine and Biology, 21(6): 769–778, 1995.

11 FL Bookstein, “Shape and information in medical images: a decade of morphometric synthesis,” Computer Vision and Image Understanding 66, 97–118, 1997.

12 FL Bookstein, “Morphometric Tools for Landmark Data,” Cambridge University Press, Cambridge. 1991.

13 H Park, PH Bland, KK Brock, CR Meyer, “Adaptive registration using local information measures,” Med Image Analysis 8, 465–473, 2004.

14 R Shekhar, V Zagrodsky, “Mutual Information-based rigid and non-rigid registration of ultrasound volumes,” IEEE Trans. Med. Imaging 21(1), 9–22, 2002.

15 X Pennec, JP Thirion, “A Framework for Uncertainty and Validation of 3-D Registration Methods Based on Points and Frames,” Intl J Computer Vision 25(3), 203–229, 1997.

16 S Sarkar, R Narayanan, H Park, B Ma, PH Bland, CR Meyer, “Quantitative growth measurement of lesions in hepatic interval CT exams,” Proceedings SPIE Medical Imaging Vol. 6914, pp. 69141G-1–69141G-10.

CHAPTER 6 FIRSTHAND APPLICATION OF NON-RIGID TRANSFORMATION IN CLINICAL ENVIRONMENT: CORRECTION OF THE ELECTROMAGNETIC FIELD DISTORTION IN A CT SCANNER ENVIRONMENT

6.1 Introduction

Image guided surgery (IGS) displays the patient anatomy information as well as the location and orientation of the medical tool with respect to the target organ in the human body. Patient information could be in the form of pre-operative CT or MRI image or a real-time ultrasound or fluoroscopy. Real-time tracking of the medical tool inside patient's body had greatly benefited many medical procedures including minimally invasive surgery (MIS). MIS procedures performed through a small opening in the body provides for reduced patient discomfort, healing time, risk etc. IGS based on tracking system has seen many developments over the last few years. IGS has proven to be useful in various clinical applications including endoscopic navigation of ear, nose, throat (ENT)[1, 2], image guided spine surgery[3,4], ultrasound calibration[5], hybrid tracking system[6], catheter tracking [7] as well as kinematical and biomechanical studies of joints [8, 9] Electromagnetically (EM) tracked ultrasound (US) probes found utility in laparoscopy for extracting tumor location and boundary[10], although distortion to the EM field was shown to be larger from a 3D US probe than a 2D US probe.[11] Modern medical tracking systems use either optical or electromagnetic tracking systems (EMTS) and make the procedure safer, simpler, more accurate, and faster. The usefulness of one such tracking system is

dependent on accuracy and stability of localizing a medical tool relative to the target anatomy in the clinical environment.

Optical tracking systems have proven to have high standards of accuracy in the past, but the line-of-sight requirements between the navigating tool and the sensor unit that limit its usage in the clinical environment.[12] Earlier work by Traxtal, a manufacturer of tracking instruments, dealt with studying the accuracy of EM tracked needles using optical tracking system (OTS).[13] Other studies in the past have shown the intra-operative precision and stability by combining OTS and EMTS.[14, 15] EMTS was based on externally generated EM field produced by a field generator and line-of-sight requirements or changes in work flow were not needed. When an EM sensor was placed in the field, it induced an electrical signal in the sensor which was measured by the tracking system. From the known characteristic properties of the EM field (or a physical model of the magnetic field), the position and orientation of the sensor was estimated. Positions can be identified even within the patient's body as the EM field penetrates the human or animal body undisturbed. Miniature EM sensors placed at the tip of non-rigid medical or surgical tools (including needles, catheters etc) were used in tool tracking.

The accuracy of an EMTS under undistorted operating conditions cannot determine the inter-operative performance in a clinical environment. Any disturbance in the EM field could lead to inaccurate readings of both the position and orientation of the EM sensor. Under realistic operating conditions, intra-operative precision of position and orientation of sensors was hindered by the presence of ferromagnetic or conducting metals, surgical instruments, operating table, stray fields from power lines in the vicinity etc.[16, 17, 18] The degree of distortion depends on the tracking system, operating environment as well as the sensor used for characterization. EMTS was determined to be more sensitive to perturbations from materials near the EM field emitter than near the sensor.[2] In the clinical environment, it was not always possible to remove some of the known sources of distortions, mainly when they constitute a part of the IGS or MIS. The distortion mapping of the EM field was studied to understand the positional error and this served as the motivation for this study.

Accuracy and mapping errors of tracking systems were studied with specific ways of quantifying error.[19, 20, 21] Most of these studies did not take into account the

dependence of accuracy of sensor position on the orientation of sensor. A study on medical applications of tracking using position/orientation polynomial fitting was one of the first few papers to consider orientation as well as spatial dependence of errors in position.[22] Recently, a few studies have identified novel ways of dealing with the error estimation in 6 degrees of freedom (DOF) space.[23, 24, 25] Apart from sensor orientation, accuracy also depends on gross patient motion (including respiratory motion), organ deformation, and transformation procedure apart from the metal distortion artifact.

The purpose of this study was to examine the EM field distortion pattern and the positional accuracy of EMTS using EM sensors placed along a few different orientations in a Computed Tomography (CT) scanner environment. 3D rigid body transformation (RT) was used between the "gold standard" positioning system and EMTS estimated positions of sensors followed by non-rigid transformations to correct for any non-rigid EM field distortion. This had helped in characterizing the field curvature and provided a better understanding of the error in estimating positional accuracy along a few sensor orientations in the CT scanner environment.[26, 27, 28, 29] The dependence of positional accuracy on the position of sensor within the field-of-view (FOV) of the EMTS as well as the sensor orientation was studied. Dependence of positional error with the distance from field generator was also studied. Furthermore, changes in distortion due to the presence of ultrasound (US) system in the vicinity of Aurora field generator were estimated in the CT scanner environment.

6.2 Materials and Methods

In this study, we evaluate the second generation Aurora™ (Northern Digital Inc. (NDI), Waterloo, ON, Canada) EMTS in a simulated reproducible CT scanner environment. The characteristic measurement volume for Aurora system was a cube of volume 50cm x 50cm x 50cm projected normal to the face of the field generator with an approximate offset of 5 cm from the face of the field generator. The root mean square (RMS) position and orientation accuracies were 0.9 mm and 0.3^0, respectively within the cube volume in a metal-free environment, as quoted in the manufacturer's specifications.[30] The sensor was placed within the cube characteristic volume of the

tracking system for estimation of position and orientation. For tracking purposes, we used the five degrees of freedom (5DOF) NDI sensor coils embedded inside MagTrax needle (Traxtal Technologies, Bellaire, TX, USA) with a physical offset of 7 mm from the needle tip. A system control unit processes the sensor signals and calculates the position and orientation of the sensors at a maximum measurement rate of 40 Hz and also communicates to the host computer via a RS-232 interface. The standard software provided by NDI for data acquisition was ToolViewer, which displays position and orientation data for each sensor in real-time. All measurements were made on a Brilliance 16-slice CT scanner (Philips Medical Systems, Cleveland, OH).

In order to evaluate the accuracy of the Aurora system, the "gold standard" sensor location coordinates were measured using a positioning system. A three-axis robotic positioning system was custom-built with BiSlide assembly driven by computer controlled NEMA34 stepper motor and VXM-3 stepper motor controller (Velmex Inc., Bloomfield, NY) that provided the "gold-standard" of sensor position. The lead screw accuracy for the positioning system was 0.038 mm over a travel distance of 25 cm and straight line accuracy of 0.038 mm over the entire travel distance.[31] A backlash compensation mechanism was integrated into the positioning system in order to compensate for positioning differences when travelling along positive or negative directions. A cube shaped sensor holder (side 2 cm) was custom built with eight 5DOF sensors, one each along the ±X, ±Y, ±Z and one along two of the four body diagonals. These eight sensors were set at a fixed offset of 3 mm from the cube center. In order to minimize the metallic distortion, a sensor holder made of acrylic glass or polymethyl methacrylate (PMMA) was mounted onto a 1 m long arm of the positioning system made of poly-vinyl chloride (PVC). Calibration of the eight sensors inside the holder was performed in a metal-free undistorted environment using the NDI 6D Architect Aurora software.

Aurora field generator was positioned beside the CT table with its center at a height of 35 cm above the table and 60 cm from the face of the CT gantry, as shown in Figure 6.1. Axial view of the coordinate system is shown in Figure 6.2 with +X vertical axis running from the center of FOV pointing to the ground, +Y horizontal towards the CT gantry and –Z axis pointing towards the FOV in front of the Aurora system.

Characterizing the EM field distortion starts with gathering large quantities of measurements and comparing them to the reference measurements. Raster scan was performed within the FOV volume of 30cm x 30cm x 30cm positioned at the center of the cube volume of 50cm x 50cm x 50cm and 30cm in front of the face of Aurora. A

Figure 6.1: Setup of the CT scanner environment with a) NDI Aurora field generator besides the b) three-axis positioning system that raster scans the c) EM sensor holder. Also shown in the figure was the d) CT gantry and e) CT table.

spatial sampling resolution of 2.5 cm in all three axes yielded 2197 locations with the FOV for the sensor holder. The sample resolution was considered adequate to represent the overall error distribution with a reasonable data acquisition time based on previous work.[26, 27, 29] Control of the three-axis positioning system and data collection was performed using a Matlab® based interface. For measuring the static accuracy of the sensor position and orientation, these measurements were acquired at zero velocity.[15] At every location, the positioning system stopped for over 100 milliseconds and Aurora system collected 20 readings of position and orientation of each of the eight sensors. The

mean, standard deviation of these 20 position and orientation readings were relayed by

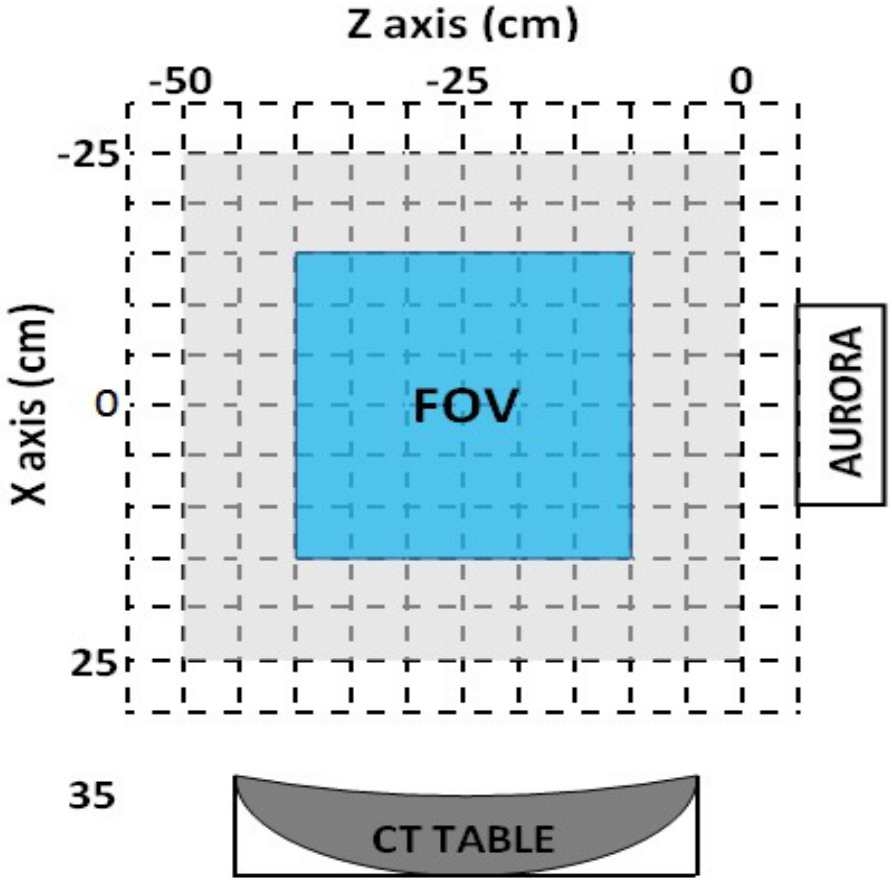

Figure 6.2: Axial view of the experimental setup and the coordinate system along XZ plane at Y=0. Center of volumetric scan was positioned 35 cm above the CT table, 25 cm in front of the Aurora system (with an additional 5 cm offset) and 60 cm away from the CT gantry. Volume of FOV was 30cm x 30cm x 30cm.

Aurora along with the location of sensor holder from the three-axis positioning system to the Matlab® based interface in the host computer.

A software package was developed for data processing, field characterization including distortion curvature mapping, rigid body and non-rigid transformations, and error estimation as well as orientation measurement. This package also has the capability to compensate for the distortion in EM field using a non-rigid warping model discussed below. This can be used either for compensation of EM field distortion or to estimate systematic distortion of a particular Aurora unit.

Orientation data was represented using quaternions which represent rotation in 3D space around an arbitrary axis. Quaternions provided a uniform and rotation independent

description of all possible orientations.[32] The use of quaternions reduces the approximations and number of computations involved in a 3D rotation or interpolation and avoids the gimbal lock issue with Euler angles.[33, 34] In this study, orientation data was collected as a set of 4 quaternions for each sensor placed within the FOV of the field generator. The quaternions were converted to a rotation matrix that contains information about the direction of the sensor.

6.3 EM field Distortion mapping using Transformation

In this CT scanner environment, the main source of EM field distortion was identified as the CT table with its metal plate that supports the patient and helps in the patient motion along the longitudinal axis (in and out of the CT gantry). The error in position and orientation of the sensor was least at a distance farthest from both the CT table but near the Aurora field generator.[26, 27] The baseline region was identified as a region of 10cm x 10cm x 10cm symmetric to the face of Aurora field generator within the FOV and located farthest away from the CT table. The baseline region was defined more by practicality than by optimization of errors in position or orientation of the sensors.[28]

In order to align the position data of sensors in Aurora coordinate system with respect to the positioning system coordinates in the CT scanner environment, a point-to-point rigid alignment of the two data sets was obtained. The rigid body rotation and translation parameters were computed using least-squares fit.[35, 36] 3D affine transformation parameters (rotation, translation, scaling and shearing) were also obtained. As a measure of accuracy, transformation error was estimated as the Euclidean distance between the registered data points and the positioning system coordinates in 3D space.

The final step in the transformation process was the non-rigid thin plate spline (TPS) based 3D non-rigid (warping) transformation that took into account elastic distortions to the EM field. TPS was a smooth function with continuous first order partial derivatives and was considered for modelling functions with local distortions that are too complex to fit with a polynomial.[37, 38, 39, 40] Consider a hypothetical, infinitely thin, metallic plate extending to infinity in all directions. At a finite number of discrete points, the plate was at fixed heights. The metal plate will take a unique form that minimizes the

bending energy.[41] The bending energy was considered equivalent to the physical energy needed to bend the plate normal to the surface at finite set of discrete points. Thus, by definition, any motion along the surface of the plate needs zero bending energy as it was the case with RT and affine transform (neglecting gravity). In this study, the EM field distortion in the CT scanner environment was estimated using the TPS based warping model. The TPS based warping transform maps the Aurora coordinates onto the corresponding three-axis positioning system coordinates with a minimum bending energy of any such interpolant. Having modeled the distortion to the EM field, error in the sensor position as well as the spatial variation can be estimated for a given sensor orientation. The computation time in estimating the EM field distortion using TPS transformation (TPST) was dependent on the number of DOF or number of sample points (typically, N=2197 points collected at 2.5 cm spacing along all three axes).[42]

6.4 Error Analysis using Jackknife Technique

Unbiased error estimation of the RT and TPST models were based on the jackknife cross-validation method.[43,44,45] Bias reduction aspect of the jackknife method is also related to the reduction in RMS error.[46, 47] From the collection of N=2197 independent and identically distributed data points, data was split into two portions without replacement.[48] Consider 2 set of data points: aurora location coordinates $\{x_i\}$ and positioning system coordinates: $\{y_i\}$ where $1<=i<=N$. The first subsample pairs of $\{x_j\}$ and $\{y_j\}$ data points where $1\leq j\leq N$ for $j\neq i$ consisting of N-1=2196 data points was used for construction of the RT and TPST models while the data point (x_i), (y_i) was used in estimating the error in transformation.[49] The corresponding transformation error is the Euclidean distance between the transformed data point in Aurora coordinate system $T(x_i)$ and the positioning system coordinates in 3D space, y_i. RMS error = $\| T(x_i) - y_i \|$, $1<=i<=N$. This process was repeated with each i where, $1<=i<=N$, in order to remove any spatial bias in the error distribution. The RMS, standard deviation and error range of RT and TPST based models were recorded and compared.

6.5 Validation with CT Abdomen Phantom

Using the three-axis positioning system, characterization of the EM field in the CT scanner environment yielded a set of RT and non-rigid transformation parameters. Given a new set of position and orientation data of EM sensor, these transformation parameters could be utilized to obtain the distortion corrected location of the sensor. A phantom study was designed using a CT abdomen phantom (CIRS, Norfolk, VA, USA) with 7 known fiducial markers and unknown test needle placed on the CT table within the FOV of Aurora field generator, as shown in Figure 6.3.

Figure 6.3: Experiment setup of CT abdomen phantom study with EM sensor coils embedded inside a needle that points along the +X axis (vertically downward). Center of the phantom is near the center of the FOV.

The methodology for EM field characterization was outlined below:

a) Traxtal needles with EM sensor coils were manually positioned at each of the 7 fiducials in the CT abdomen phantom (4 along +Y axis on the face of the phantom

away from the gantry; 3 along –Y axis on the face of the phantom near the gantry). These locations were recorded in Aurora coordinate system.

b) Orientation dependent and TPS based distortion corrected locations were obtained for these 7 data points in the Aurora coordinate system.

c) Along with a test needle placed inside the phantom along the +X axis, the phantom was translated into the CT gantry and a 3D CT image was obtained using standard imaging parameters.

d) From the locations of 7 fiducials in Aurora coordinates in a) and the corresponding CT image coordinates in c), a rigid transform ${}^{CT}R_A$ was obtained. This RT corresponds to the translation of the CT table along Y axis. Similarly, TPS based distortion corrected fiducial locations in b) and the corresponding CT imaging coordinates in c) were transformed rigidly to obtain ${}^{CT}R_{A\text{-}TPS}$.

e) Apply the rigid transform ${}^{CT}R_A$ on the location of test needle in Aurora coordinates without any distortion correction to obtain $P_{test\text{-}A}$. Repeat it with ${}^{CT}R_{A\text{-}TPS}$ using TPS based distortion correction $P_{test\text{-}A\text{-}TPS}$.

f) Location of test needle in CT coordinate system was $P_{test\text{-}CT}$. Error in transformation was the Euclidean displacement between test fiducial $P_{test\text{-}CT}$ and $P_{test\text{-}A}$ as well as with distortion correction, $P_{test\text{-}CT}$ and $P_{test\text{-}A\text{-}TPS}$.

6.6 Results

This section presents the results of data acquisition in the CT scanner environment with the center of 30cm x 30cm x 30cm FOV aligned with the center of the cube characteristic volume of the Aurora field generator. Sampling resolution of 2.5 cm along all the three axes yielded a total of N=2197 data points for each of the 8 sensors. Among the eight 5DOF EM sensors oriented along various directions, data was acquired from only six sensors along the ±X, ±Y, and ±Z axes. Due to certain unknown technical challenges, data was not recovered from the sensors along the 2 body diagonal of the sensor holder. In all of the 6 sensor position data, some of the data points were marked invalid by the internal quality flag, as per the manufacturer's specification and were discarded.

6.6.1 Baseline Accuracy

Sensor position in the Aurora system coordinates were aligned with the positioning system coordinates using 3D RT over the 10cm x 10cm x 10cm baseline region. The RMS, standard deviation and range of error (in mm) in position of the sensors appear in Table 6.1. Among the 6 sensor orientations within the baseline region, the RMS position errors were found to be lowest for sensors along ±X axes.

Table 6.1: Accuracy of position data (in mm) along the 6 orientations inside the baseline region using 3D rigid transform. Notice the lowest RMS position errors in sensor along ±X axes.

Orientation:	**+X**	**+Y**	**+Z**	**-X**	**-Y**	**-Z**
RT:RMS ± Std (mm)	1.6±0.8	5.8±2.8	6.3±3.8	1.6±0.8	5.2±2.5	5.4±2.9
Error range (mm)	0.3–4.7	0.6–17.6	0.2–30.3	0.2–4.7	0.9–15.8	0.3–15.5

6.6.2 Outliers

Data acquisition by Aurora system consisted of a position, orientation data along with the corresponding standard deviations from 20 such readings acquired at each of the N=2197 points within the FOV. Using RT for a sensor along +X axis in the CT scanner environment between the Aurora and positioning system coordinates, histogram of the error magnitude and positional errors (in mm) were shown in Figure 6.4 (a) and (b), respectively. Few outliers that were larger than 5 standard deviations from the mean were identified in the position data from all the 6 sensor orientations. Repetition of the raster scan under identical environment resulted in similar outliers at the same location. Hence, none of these outliers were discarded from data analysis for lack of any compelling reason.

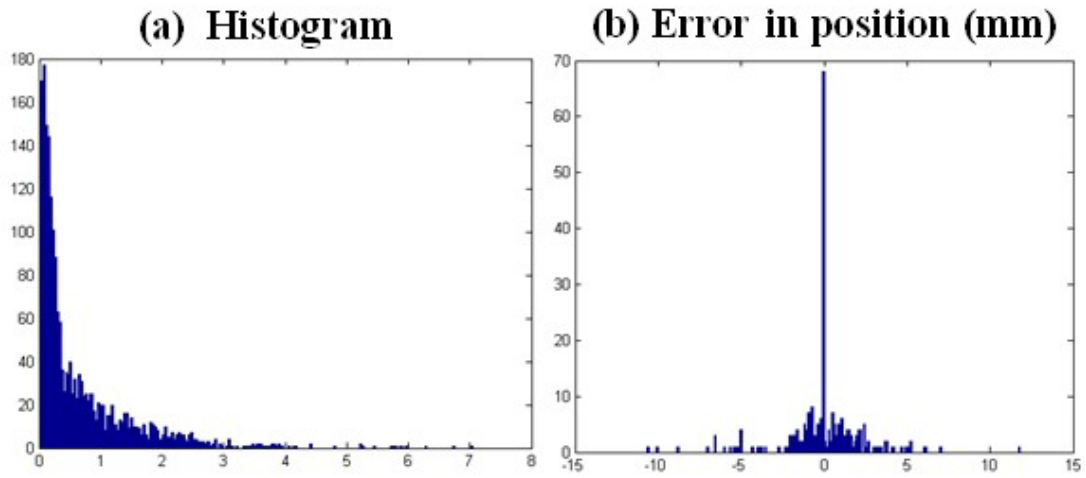

Figure 6.4: (a) Histogram of error magnitude and (b) Position error (in mm) using RT of Aurora system coordinates with the positioning system coordinates for the sensor along +X axis in the CT scanner environment.

6.6.3 Error Analysis – Jackknife technique

The relative sensor position data from the Aurora and positioning system coordinates for a probe along –Y axis in the CT scanner environment are shown in Figure 6.5. The largest error in the sensor position was observed in the region farthest from the field generator (located at origin: X=Y=Z=0) and nearest to the CT table (along Y axis, X=350mm, Z=–250mm). Similar observations can be inferred from sensors along all the six needle orientations. At any given location in 3D within the FOV, the positional errors were different for each sensor orientation. Thus, apart from the electromagnetic distortion in the particular configuration, the orientation of the sensor has a large effect on the accuracy of position measurement[28].

For error estimation of the 3D RT and TPST of the sensor position data in Aurora coordinates in the CT scanner environment, jackknife cross-validation method was used. N–1=2196 data points were used to construct the RT and TPST models, the corresponding error was estimated from the data point left out and this process was repeated for each of N data points. From N such transformations, the mean RMS, standard deviation and error range (in mm) are shown in Table 6.2 for each of the 6 sensor orientations. As compared with RT, TPST had a statistically significant lower

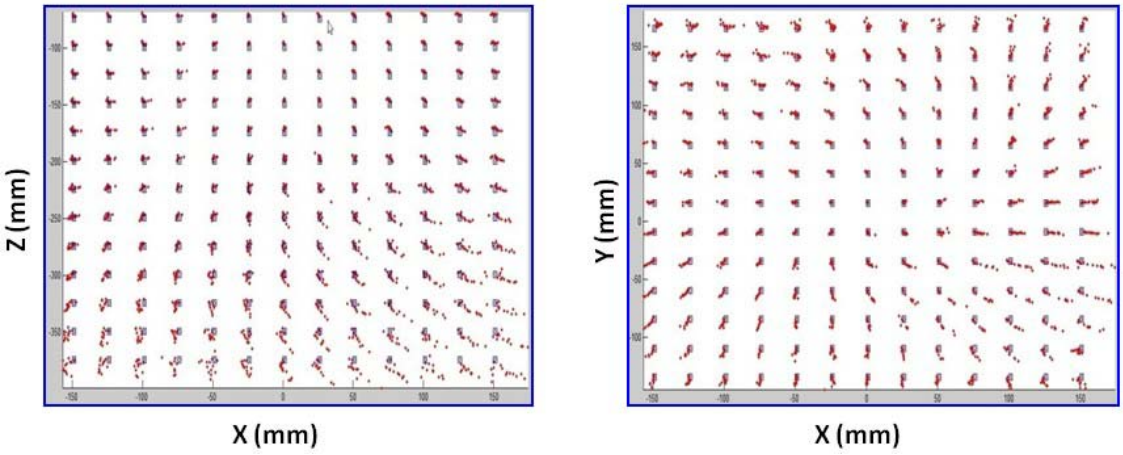

Figure 6.5: Shown for a probe along –Y axis, relative positions of the positioning system data (blue box) along with the Aurora system coordinates using 3D RT (red dots) and TPS warping (black circles) along XZ plane (left image) and along XY plane(right image). Not shown here was the Aurora field generator located with its center at a height of 35 cm from the CT table which was running lengthwise along the Aurora Y axes. Notice that the positioning error was least in the region closer to the field generator and farthest away from CT table. Also notice that the TPS warped data points match with the data points in the positioning system coordinates.

mean of RMS position errors along all 6 sensor orientations (p<0.002). Sensors along the +Y, –Y axes had higher mean RMS errors of 5.6 mm, 5.5 mm based on RT model and 1.1 mm, 1.0 mm based on TPST model, respectively. Sensor along –Z axis had lowest mean RMS error of 2.0 mm based on RT and 0.8 mm based on TPST.

Table 6.2: Accuracy of position data of sensors along the 6 orientations in CT scanner environment for RT and TPS based models constructed using (N-1) data points and error estimated using the 1 data point left out. 1st row shows various orientations along which the sensors were positioned. 2nd and 3rd rows show the RT based mean RMS ± standard deviation and error range in position (in mm), respectively. 4th and 5th row shows the corresponding values for TPST.

Orientation:	**+X**	**+Y**	**+Z**	**–X**	**–Y**	**–Z**
RT: Mean RMS ± Std (mm)	2.9±2.1	5.6±3.9	4.0±3.1	3.1±2.4	5.5±3.9	2.0±1.6
RT: Error Range (mm)	0.2–16.9	0.8–33.6	0.3–30.1	0.1–23.1	0.4–34.1	0.1–13.8
TPS: Mean RMS ± Std (mm)	0.8±1.1	1.1±1.7	1.6±2.7	0.8±1.3	1.0±1.4	0.8±1.3
TPS: Error Range (mm)	0.0–11.6	0.0–31.4	0.0–28.8	0.0–22.4	0.0–12.1	0.0–12.4

6.6.4 EM Field Curvature

3D spatial variation of error in the sensor position was crucial in characterizing the EM field distortion. In order to remove any spatial bias in error estimates, sensor

positions were normalized into a 10x10x10 rectangular grid for each of the 6 sensor orientations. This grid represented the *N* evenly spaced data points within FOV in the CT scanner environment and TPS based warping model was used to generate the warped grid for each sensor orientation. Shown in Figure 6.6 for a sensor along the +Z axis in the CT environment was the undistorted rectangular grid (black); the warped grid along the XY plane at Z=-250 mm (red) and along the axial XZ plane at Y=0 mm (blue). Notice the presence of EM field curvature and also large spatial variation of positional error.

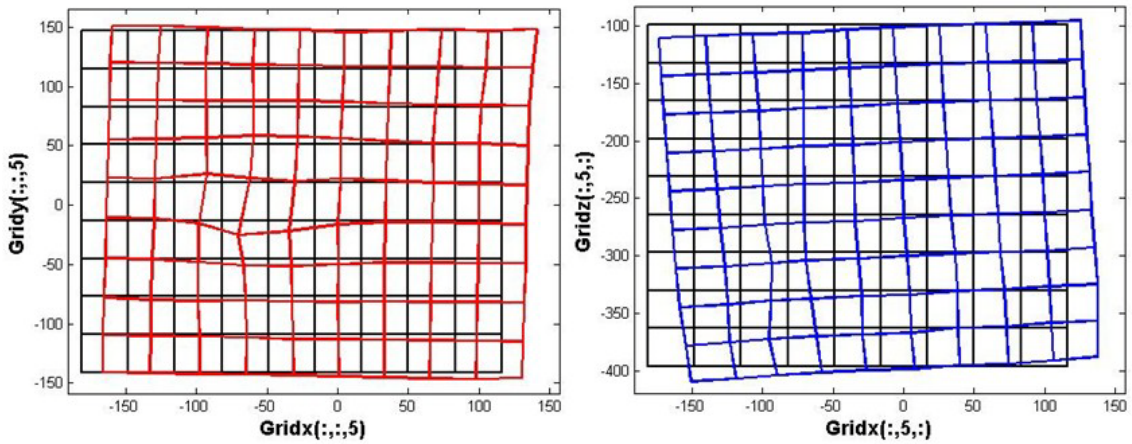

Figure 6.6: EM sensor position data collected for a sensor along the +Z axis in CT scanner environment. Shown here was the normalized 10x10x10 grid in black with a) the warped grid in red along the XY plane at Z=-250 mm and b) the warped grid in blue along the axial XZ plane at Y=0 mm.

6.6.5 Position Error as function of distance from field generator

The plot shown in Figure 6.7 was the RMS error in position of EM sensor as a function of Euclidean distance from the Aurora field generator (Z in mm – positioning system coordinates), for a sensor along the –Z axis in the CT scanner environment. Error estimation was based on the jackknife method. This plot was based on RT and TPST model formed using (*N*-1) points and the corresponding error was estimated using the lone data point left out. Notice the decrease in position error with distance from the field generator and also lower error magnitude using TPST than RT.

From Figure 6.7, the RMS error in position (rounding off to the nearest hundredth mm) was given by linear regression as:

RT: RMS Error = 0.0105*Z – 0.21(in mm)

TPST: RMS Error = 0.0066*Z – 0.57 (in mm)

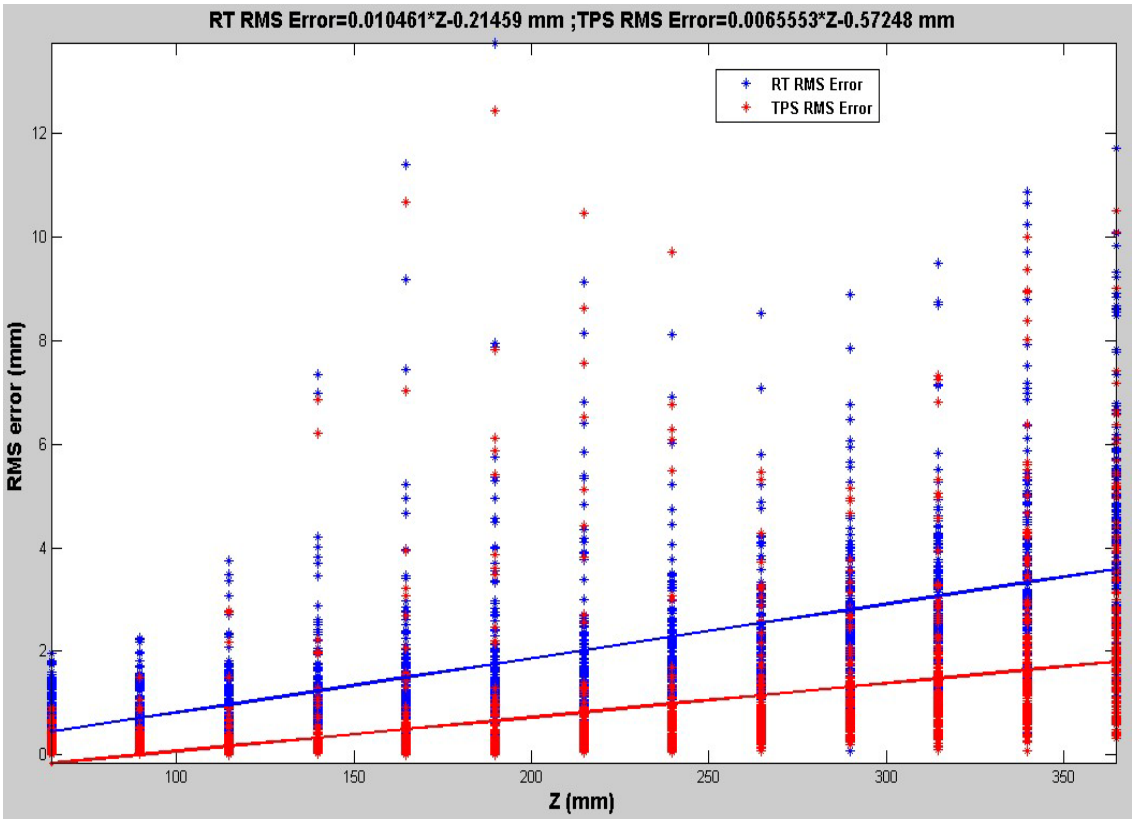

Figure 6.7: Positional RMS error for a sensor in CT scanner environment along –Z axis using a) RT (blue) and b) TPST (red) shown as a function of distance (in positioning system coordinates) from the Aurora field generator. Line of linear regression (least squares fit) was also drawn for reference. Clearly, the RMS error in sensor position increased with distance from the field generator and error magnitude was lower with TPST than RT.

6.6.6 Error in Orientation

Orientation of sensor was represented by a quaternion due to many advantages[33]. Quaternion data was converted into rotation matrix that contains directional information of the sensor. For a quaternion defined: $Q = [Q_0\ Q_x\ Q_y\ Q_z]$, the normal **n** was given by the third column of the rotation matrix[50]:

$$\mathbf{n} = [\ 2*(Q_0*Q_y + Q_x*Q_z) \quad 2*(-Q_0*Q_x + Q_y*Q_z) \quad Q_0^2-Q_x^2-Q_y^2-Q_z^2]$$

Orientation along X, Y or Z axes was defined as the normalized components of the normal, **n**. Figure 6.8 shows that orientation of 6 sensors along the ±X, ±Y, and ±Z axes as a straight line of uniform length pointing towards the direction of the normal (drawn in different colors) using sparse data set (*N*=64 points at 10 cm spacing along all three axes). Table 6.3 shows the accuracy in orientation measurement along the 6 orientations in the CT scanner environment on a scale of [0,1]. Notice the large standard deviation and range of the normal component of rotation matrix for the sensor along –Z axes. Notice that the accuracy of measurement of the normal direction depends not only on the orientation of the sensor but also on the location of the sensor within the FOV of Aurora field generator.

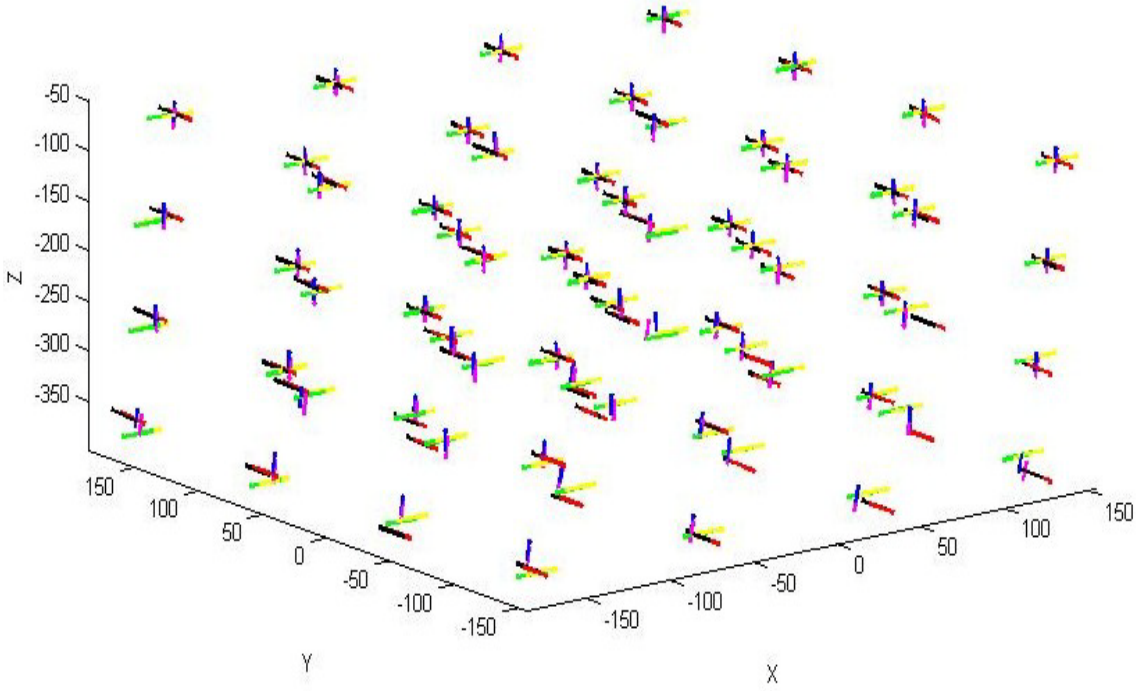

Figure 6.8: Orientation of all 6 sensors along the ±X, ±Y, and ±Z axes in FOV of Aurora system in the CT scanner environment. Notice that the sensor orientations nearest to the field generator (at top centre of figure near X=Y=Z=0) and farther away from CT table were estimated to have least error. Conversely, large errors were observed along all sensor orientations at distances farthest from the field generator. Notice that sparsely collected data (N=64 points at 10 cm spacing along all three axes) was shown here for clarity of viewing.

Table 6.3: Accuracy of magnitude of normal component of the rotation matrices for sensors along the 6 orientations in CT scanner environment. 2nd, 3rd and 4th rows shows the RMS mean, the standard deviation and the range of normal component of rotation matrix along the leading orientation;. Notice the large deviation and range of magnitude of normal component of rotation matrices for the sensor along –Z axes.

Orientations:	+X	+Y	+Z	-X	-Y	-Z
RMS normal	0.9966	0.999	0.9971	0.9967	0.9989	0.9683
Std Dev	$8.8*10^{-4}$	$7.1*10^{-4}$	$2.2*10^{-3}$	$1.3x10^{-3}$	$7.8x10^{-4}$	$7.5*10^{-2}$
Range	0.9923–0.9996	0.9914–0.9998	0.9779–0.9998	0.9566–0.9997	0.9936–0.9998	0.0025–0.9989

6.6.7 Presence of US system in CT scanner environment

Shown in Figure 6.9 is the CT scanner along with a iU22 Philips ultrasound (US) system turned ON within a distance of 5’ from the CT table and 4’ from the Aurora field generator. A C5-2 curved linear US probe with 128 elements was attached to the positioning system arm along with the sensor holder. The FOV was raster scanned by the sensor holder attached with the US probe. The accuracy of measurement of position data by the Aurora field generator for 6 EM sensor orientations shown in the setup in Figure 6.9 was tabulated in Table 6.4.

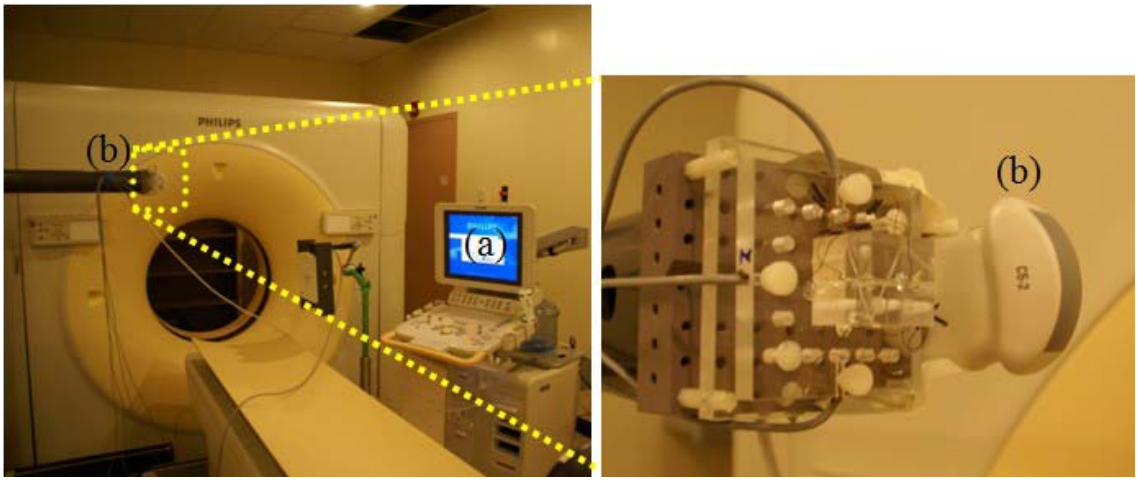

Figure 6.9: Setup of the CT scanner environment with (a) Philips Ultrasound (US) system turned ON and (b) C5-2 curved US probe attached along with the sensor holder.

In the CT scanner environment along with presence of the US system, 3D RT and TPST were used to model the sensor location coordinates. From these *N* independent estimates, mean of the RMS, standard deviation and error range (in mm) were estimated

using jackknife method for all 6 sensor orientations and the results were summarized in Table 6.4. In the CT scanner environment along with presence of the US system, TPST had a statistically significant lower mean of RMS position errors along all 6 sensor orientations as compared with RT (p<0.001). In comparison between the mean RMS errors in position of sensors along the 6 orientations with and without the presence of US system, there was no significant difference from each other either with RT (p-value>0.18) or with TPST (p-value>0.44). This shows that the presence of the Philips US system within 4' from the Aurora system and 5' from the CT scanner does not produce significantly detectable disturbance in the EM field. Even though there was no significant bias of location error for sensors along a particular direction, a general trend was seen in sensors along the +Y, –Y axes with larger position errors using both RT and TPST models.

Table 6.4: Accuracy of position data of EM sensors along the 6 orientations in CT scanner environment in the presence of the ultrasound system in the vicinity. RT and TPS based models were constructed using (N-1) data points and error estimated using the lone data point left out. 1st row shows various orientations along which the sensors were positioned. 2nd and 3rd row shows the RT based mean RMS ± standard deviation and error range (in mm), respectively. 4th and 5th row shows the corresponding values for TPST. TPST gave significantly lower mean RMS error than RT (p-value<0.001) while the presence of Philips US system in the vicinity of CT scanner did not significantly alter the mean RMS error in position either using RT (p-value>0.18) or using TPST models (p-value>0.44). Notice the low mean RMS error in position for a sensor along +X axis and high RMS errors in sensors along ±Y axis.

Orientation:	**+X**	**+Y**	**+Z**	**–X**	**–Y**	**–Z**
RT: Mean RMS ± Std (mm)	2.9±2.1	5.7±4.0	3.8±2.7	3.0±2.4	5.7±6.4	3.3±2.5
RT: Error Range (mm)	0.1–15.1	0.7–60.2	0.3–21.5	0.1–22.2	0.5–162.6	0.2–21.7
TPS: Mean RMS ± Std (mm)	0.7±0.9	1.0±2.3	1.3±2.1	0.7±1.1	1.3±4.5	1.2±1.9
TPS: Error Range (mm)	0.0–13.9	0.0–61.1	0.0–21.7	0.0–21.6	0.0–103.8	0.0–22.9

6.6.8 Validation with CT Abdomen Phantom

CT imaging was performed to obtain the error in location of a test sensor along +X axis having known the locations of 7 fiducial markers on the abdomen phantom in the Aurora and CT imaging coordinate systems. The locations of the 7 fiducials were identified in Aurora coordinate system by touching them with the sensor fortified needle.

CT image coordinates of 7 fiducials were rigidly transformed into the 7 Aurora coordinates with and without TPS based distortion correction. Then a CT image of the phantom was obtained with a needle inserted along +X axis seen as streaking metal artifact in Figure 6.10. Due to the streaking artifact, there was an approximation involved in the identification of needle tip.[51] The phantom was moved away from CT gantry and into the FOV of Aurora field generator and location noted in the Aurora coordinates. RT between Aurora and CT imaging coordinate systems were applied with and without TPS based distortion correction. The error in location of the sensor was estimated to be the RMS Euclidean 3D distance between the CT image and Aurora coordinates with and without TPS based distortion correction. Subtracting the separation of needle tip from the EM sensor of 7mm, the mean position error reduced substantially from 3.5 mm to 1.7 mm due to TPS based distortion correction. More tests are needed to produce statistically significant results.

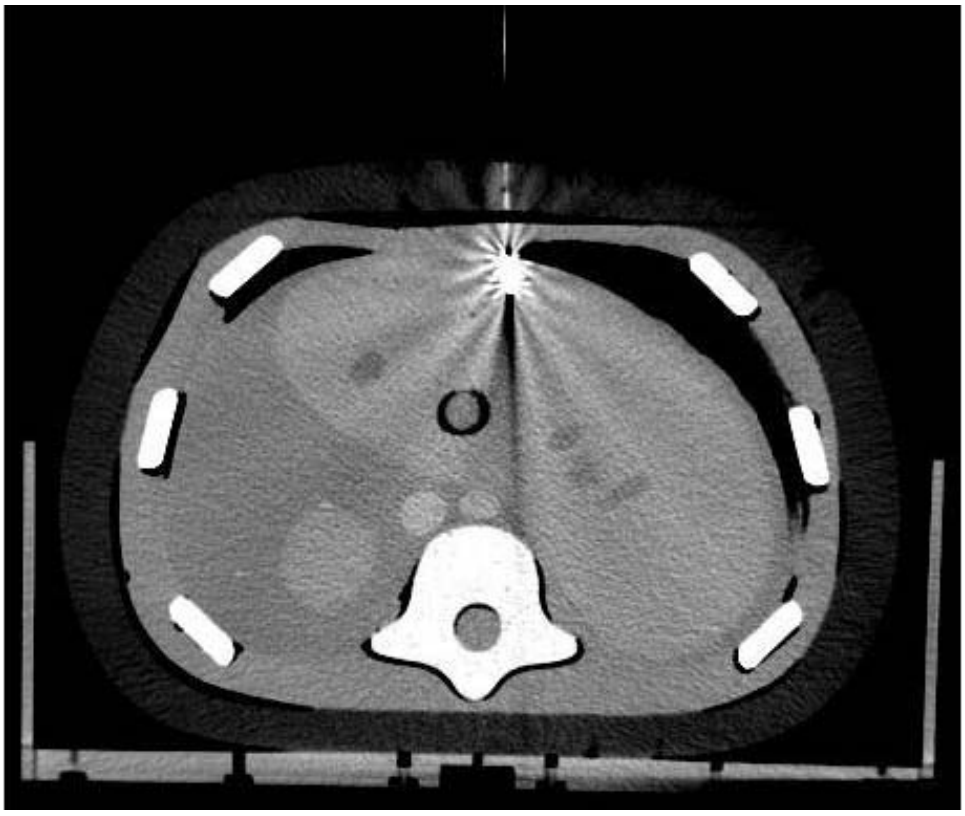

Figure 6.10: CT image of abdomen phantom with needle insertion (top center) that could be tracked using EMTS.

6.7 Discussions and Conclusions

We have demonstrated a few simple ways to evaluate the static accuracy of Aurora field generator. The latest generation of EMTS continues to improve their accuracy and tolerance with metal distortion in a clinical environment. Although the EMTS were affected by metal distortion, they can detect and limit the magnitude of distortion.

This study has covered the use of sensors to characterize the EM field so that EM tracking could be used with improved accuracy in MIS. Characterization of systematic distortions to the EM field in the CT scanner environment was studied using an Aurora field generator (second generation). EM field curvature and positional error of sensors along a few orientations were some of the vital results of this study. It was also shown that the error in position was large near the CT table and increased with distance from the field generator. Use of TPS based warping model resulted in significant reduction in positional error of sensors over an RT model. Estimation of warping coefficients contributed towards the reduction in the position error in the CT scanner environment. These coefficients were based on the model, environment and also accuracy requirements. Presence of the US system in the CT scanner environment did not alter the positional accuracy of EM sensors significantly. However, more investigation was needed for the sensor along –Z axis as it had the lowest RMS position error (refer to Table 6.2) while the RMS orientation error had the highest standard deviation and largest range (refer to Table 6.3).

6.8 Acknowledgements

This summer internship work was performed in and supported by Philips Research North America, Briarcliff Manor, NY 10510. I would like to thank Drs. Luis Gutierrez, Douglas Stanton and Ameet Jain who helped in various capacities including with ideas, materials, fabrication and regular feedback. Special thanks go to Drs. Guy Shechter and Eric Shen for letting us use their Matlab® based algorithm for collecting data.

6.9 References

1 R Shahidi, MR Bax, CR Maurer Jr, JA Johnson, EP Wilkinson, B Wang, JB West, MJ Citardi, KH Manwaring, R Khadem, "Implementation, calibration and accuracy testing of an image-enhanced endoscopy system," IEEE Transactions on Medical Imaging 21,1524–1535, 2002.

2 J Hummel, M Figl, C Kollmann, H Bergmann, W Birkfellner, "Evaluation of a miniature electromagnetic position tracker," Medical Physics 29(10), 2205–2212, 2002.

3 HC Sagi, R Manos, R Benz, NR Ordway, PJ Connolly, "Electromagnetic Field-Based Image-Guided Spine Surgery Part One: Results of a Cadaveric Study Evaluating Lumbar Pedicle Screw Placement," Spine 28(17), 2013–2018, 2003.

4 HC Sagi, R Manos, SC Park, R Von Joko, NR Ordway, PJ Connolly, "Electromagnetic Field-Based Image-Guided Spine Surgery Part Two: Results of a Cadaveric Study Evaluating Thoraric Pedicle Screw Placement," Spine 28(17), E351–E354, 2003.

5 OH Gilja, T Hausken, S Olafsson, K Matre, S Odegaard, "In vitro evaluation of three-dimensional ultrasonography based on magnetic scanhead tracking," Ultrasound in Medicine and Biology 24, 1161–1167, 1998.

6 K Nakada, M Nakamoto, Y Sato, K Konishi, M Hashizume, S Tamura, "A rapid method for magnetic tracker calibration using a magneto-optic hybrid tracker," MICCAI 2003, Springer, 285–293, 2003.

7 N De Groot, "3-dimensional catheter positioning during radiofrequency ablation in patients," J. Cardiovascular Electrophysiology 11, 1183–1192, 2000.

8 CG Meskers, H Fraterman, FC van der Helm, HM Vermeulen, PM Rozing, "Calibration of the 'Flock of Birds' electromagnetic tracking device and its application in shoulder motion studies," Journal of Biomechanics 32, 629–633, 1999.

9 AD Milne, JM Lee, "Error analysis of a direct current electromagnetic tracking system in digitizing 3-dimensional surface geometries," Biomedical Science Instrumentation 35, 23–28, 1999.

10 D Wilheim, H Feussner, A Schneider, J Harms, "Electromagnetically navigated laparoscopic ultrasound," Surgical Technology Intl, 11, 50–54, 2003.

11 M Hastenteufel, M Vetter, HP Meinzer, I Wolf, "Effect of 3D ultrasound probes on the accuracy of electromagnetic tracking systems," Ultrasound in Medicine and Biology 32(9), 1359–1368, 2006.

12 JB West, CR Maurer Jr., "Designing Optically Tracked Instruments for Image-Guided Surgery," IEEE Transactions on Medical Imaging, 23 (5), 533–545, 2004.

13 ND Glossop, K Cleary, F Banovac, "Needle Tracking Using the Aurora Magnetic Position System," Proc. CAOS 2002.

14 A Wagner, K Schicho, W Birkfellner, M Figl, "Quantitative Analysis of Factors Affecting Intra-operative Precision and Stability of Optoelectronic and Electromagnetic Tracking Systems," Medical Physics 29(5), 905–912, 2002.

15 AJ Chung, PJ Edwards, F Deligianni, G Yang, "Freehand Cocalibration of Optical and Electromagnetic Trackers for Navigated Bronchoscopy," MIAR, Springer LNCS 3150, 320–328, 2004.

16 DD Frantz, AD Wiles, SE Leis, SR Kirsch, "Accuracy assessment protocols for electromagnetic tracking systems" Physics Medicine and Biology 48, 2241–2251, 2003.

17 W Birkfellner, F Watzinger, F Wanschitz, G Enislidis, C Kollmann, D Rafolt, R Nowotny, R Ewers, H Bergmann, "Systematic distortions in magnetic position digitizers," Medical Physics 25, 2242–2248, 1998.

18 A Wagner, K Schicho, W Birkfellner, M Figl, R Seemann, F K¨onig, R Ewers, “Quantitative analysis of factors affecting intraoperative precision and stability of optoelectronic and electromagnetic tracking-systems,” Medical Physics 29, 905–12, 2002.
19 DD Frantz, SR Kirsch, AD Wiles, “Specifying 3D Tracking Accuracy: One Manufacturer’s Views,” Workshop - Bildverarbeitung f¨ur die Medizin, Berlin, 234–238, 2004.
20 S Bryson, “Measurement and Calibration of Static Distortions of Position Data from 3D Trackers,” RNR Technical Report. No. RNR-92-011, 1992.
21 MA Livingston, A State, “Magnetic Tracker Calibration for Improved Augmented Reality Registration,” Presence: Teleoperators and Virtual Environments 6(5), 1997.
22 X Tian, KV Ling, WS Ng, “Magnetic Tracker Calibration for an Augmented Reality System for Therapy,” Proc. Inst of Mech. Eng. 215(1), 51–59, 2001.
23 X Wu, R Taylor, “A Direction Space Interpolation Technique for Calibration of Electromagnetic Surgical Navigation Systems,” MICCAI 2003 Springer LNCS 2879, 215–222, 2003.
24 X Wu, R Taylor, “A Framework for Calibration of Electromagnetic Surgical Navigation Systems,” Procs. Conf. Intelligent Robots Systems 1, 547–552, 2003.
25 X Wu, “JHU-NDI Aurora Project”. Johns Hopkins University Project Report, 2003.
26 E Shen, G Shechter, J Kruecker, D Stanton, “Quantification of AC electromagnetic tracking system accuracy in a CT scanner environment,” Proc. SPIE Medical Imaging 6509, 65090L, 2007.
27 G Shechter, E Shen, D Stanton, “Measuring and modeling metal artifacts of a CT table on AC electromagnetic tracking system accuracy,” Proc. 19th International Congress and Exhibition of Computer Assisted Radiology and Surgery, 2006.
28 GS Fischer, “Electromagnetic tracker characterization and optimal tool design with applications to ENT surgery,” MS thesis, John Hopkins University, MD, USA, 2005.
29 E Shen, G Shechter, J Kruecker, D Stanton, “Effects of sensor orientation on AC electromagnetic tracking system accuracy in a CT scanner environment” Proc. SPIE, 6918, 691823, 2008.
30 http://www.ndigital.com/medical/aurora-techspecs.php
31 http://velmex.com/bislide/motor_bislide.html
32 D Pletinckx, “Quaternion calculus as a basic tool in computer graphics,” The Visual Computer, Springer Berlin 5(1-2), 2–13, 1989.
33 K Shoemake, “Animating Rotation with Quaternion Curves,” Siggraph, Proc. Computer Graphics 19(3), 245–254, 1985.
34 R Mukundan, “Quaternions: From classical mechanics to computer graphics, and beyond,” Procs. 7th Asian Technology Conference in Mathematics, 2002.
35 PH Schönemann, “A generalized solution of the orthogonal procrustes problem,” Psychometrika 31, 1–10, 1966.
36 KS Arun, TS Huang, SD Blostein, “Least-Squares Fitting of Two 3-D Point Sets,” IEEE Transactions on Pattern Analysis And Machine Intelligence, 9 (5), 698–670, 1987.
37 FL Bookstein, Morphometric Tools for Landmark Data (Cambridge University Press, Cambridge, U.K., 1991).
38 FL Bookstein, “Shape and information in medical images: a decade of morphometric synthesis,” Computer Vision and Image Understanding 66, 97–118, 1997.
39 H Johnson, G Christensen, “Landmark and Intensity-based, consistent thin plate spline image registration,” Information Processing in Medical Imaging 2082, 329–343, 2001.
40 CR Meyer, JL Boes, B Kim, PH Bland, KR Zasadny, PV Kison, K Koral, KA Frey, RL Wahl, “Demonstration of accuracy and clinical versatility of mutual information for automatic multimodality image fusion using affine and thin plate spline warped geometric deformations,” Medical Image Analysis 1(3), 195–206, 1997.

41 FL Bookstein, “Principal Warps: Thin-plate splines and the Decomposition of Deformations,” IEEE Transactions on Pattern Analysis and Machine Intelligence 11(6), 567–585, 1989.
42 J Krücker, Ph.D Thesis, Applied Physics Program, University of Michigan, 2003.
43 MH Quenouille, “Approximate tests of correlation in time-series,” J. Royal Statist. Soc. B 11(1), 68–84, 1949.
44 B Efron, “Bootstrap Methods: Another look at the Jackknife,” The Annals of Statistics, 7(1), 1–26, 1979.
45 RG Miller, “The Jackknife – A Review,” Biometrika 61(1), 1–15, 1974.
46 JE Adams, HL Gray, TE Watkins, “An asymptotic characterization of bias reduction by jackknifing,” Ann. Math. Statist. 42(5), 1606–1612, 1971.
47 JNK Rao, JT Webster, “On two methods of bias reduction in the estimation of ratios,” Biometrika 53(3/4), 571–577, 1966.
48 DR Cox, “A note on data-splitting for the evaluation of significance levels,” Biometrika 62(2), 441–444, 1975.
49 CC Frangos, M Stone, “On Jackknife, cross-validatory and classical methods of estimating a proportion with batches of different sizes,” Biometrika 71(2), 361–366, 1984.
50 A Hast, “Shading by Quaternion Interpolation,” Winter School in Computer Graphics SHORT papers proceedings, ISBN: 80-903100-9-5, 2005.
51 GH Glover, “Compton scatter effects in CT reconstructions,” Medical Physics 9(6), 860–867, 1982.

CHAPTER 7 CONCLUSIONS & FUTURE WORK

7.1 Finger study

This study, presented in chapter 2, showed that: 1) IVBaR could reproducibly register 3D US image volumes of substantially rigid anatomical structures; 2) readers could identify the same finger in two separate scans from among those of 15 other individuals, suggesting possible use of ultrasound imaging as a patient or other human identifier and 3) physiologic stress of the individual can be detected.

In the finger study, success of IVBaR was estimated by a tolerance parameter that was defined as the deviation from the ideal rigid transformation. IVBaR on 15 finger image volume pairs from repeated scans met the 10% tolerance level, giving a sensitivity and specificity of 1.00 and 1.00, respectively. For a stricter tolerance level of 5% on the same finger image volumes, we obtained sensitivity of 0.93 and specificity of 1.00. While the IVBaR gave good results, the sample size was small and these results will require additional studies under varied conditions.

The four-reader study of matching 36 image pairs shows that the area under the ROC curve is high (Az=0.96) while that by the two expert musculoskeletal radiologists yielded ideal results (Az=1.00) signifying high accuracy for detecting matches and mismatches. These preliminary results suggest that in the majority of cases, the reader needs to be familiar with viewing US images of human anatomy but need not necessarily be a trained radiologist to identify image volumes of the same fingers.

The cardiac-gated Doppler study was designed to study another set of independent data from fingers – blood flow pattern. The advantages of having Doppler signal include the ability to measure the physiologic status of an individual. The results indicate that the Doppler signal responds rapidly to changes in the physiologic status of the individual. The password-based identification system currently being used does not

provide the physiologic status (e.g., mental stress) of an individual. In a scenario where an individual is acting against his free-will to conduct a certain act (e.g., withdrawal of cash from ATM under threatening situations), physiologic stress should alter the blood flow pattern from the ordinary. Doppler US has the capacity to detect such changes in blood flow pattern, within reasonable limits. In this study, we attempted just one mechanical task of jogging in place for a few minutes. Further research needs to be done to explore such a possibility whereby volunteers can be exposed to different kinds of stress – mechanical, mental etc. Mechanical stress could be more rigorous jogging, cycling, weightlifting, etc. while mental stress could examine reactions to their ability to solve mathematical puzzles while watching scary movie or under other stress. The sensitivity of the Doppler imaging to these types of stressors and the actual heart rate and finger perfusion would be assessed.

The finger study clearly identified a potential biometric system. A practical biometric system should not only have high sensitivity and specificity, ease of usage and simple acquisition but also be economical that are inherent advantages of US based system. It is an open question as to whether this stands a chance against iris scanners, fingerprint scanners, face recognition systems, etc. that are already available commercially. While hand-held US systems have been around for a while now, USB based US devices that can be plugged into mobile phone are starting to become available now.

7.2 Improved US breast imaging for IVBaR

Overall quality of US imaging has improved steadily in the last decade with spatial compound imaging, harmonic imaging, speckle reduction, automated or manual correction for speed-of-sound etc. Most of these capabilities are available among a variety of US system manufacturers. Shadows in US images are probably the greatest obstacle to IVBaR, as they dominate the image information content and are dependent on angle of incidence of US waves. Spatial compounding with signal processing to remove shadow artifacts would greatly improve IVBaR. A good understanding of various types of artifacts is essential in order to improve US IVBaR.

7.2.1 Mesh Paddle

In the rest of this dissertation work, a 2.5 mm thick TPX plastic plate was used for mammography-like compression of the whole breast for automated scanning. There are a few issues that include accessibility challenges with applying gel on the breast periphery, reverberation artifact (predominantly in Doppler imaging), and speed of sound correction as well as paddle attenuation of ultrasound.[1] Recently we have started using the mesh paddle that goes between the US transducer and breast surface. The mesh paddle is a crisscross pattern of 0.18 mm diameter filaments, made from ultra high molecular weight polyethylene (Dyneema®, DSM Dyneema, Netherlands), with rectangular windows of size 3mmx3mm. The mesh paddle was compared with the TPX paddle as well as no paddle for ultrasound imaging via a study of contrast, contrast to noise ratio and signal

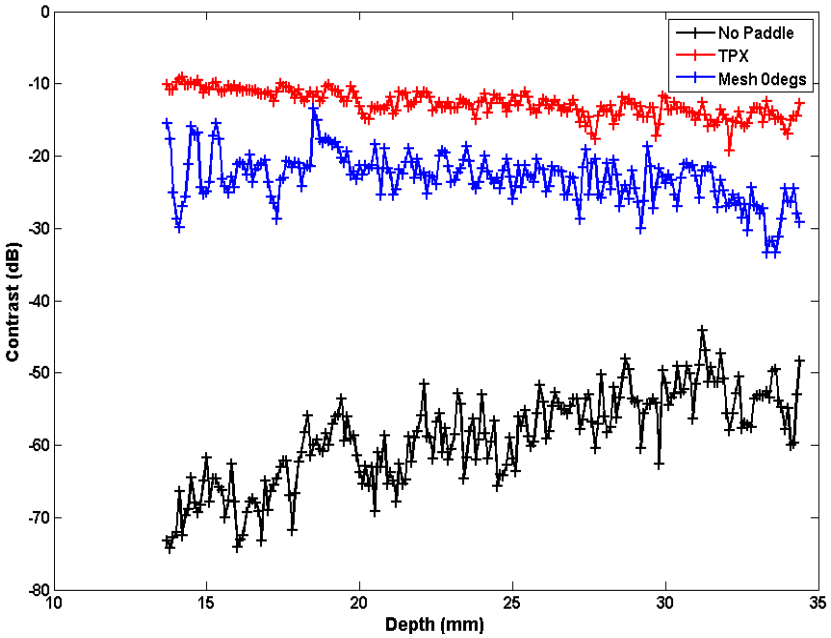

Figure 7.1: Contrast (dB) as a function of depth (mm) for 3D-US scanning using no paddle, TPX and mesh paddle oriented at 0 degrees to the direction of probe motion.

strength. It was hypothesized that the mesh paddle, compared to the TPX paddle, allows for lower attenuation of ultrasound waves, low image artifacts as well as providing higher friction that minimizes breast slippage. Phantom studies for grayscale sensitivity and contrast were performed with this paddle and initial results are promising. Shown in Figure 7.1 is the contrast (dB) as a function of imaging depth. The mean contrasts

available in US image volume at depths varying from 14 to 34 mm for no paddle, mesh paddle and TPX paddle are 59.1, 23.1 and 12.8 dB, respectively.

7.2.2 Local Compression

Another method for improving 3D viewing of tissue structures (including tumor) and at greater depths is via local, rather than global compression as in mammography or no compression. In a preliminary test by our group, breast tissue was compressed locally by the probe face. As compression was increased, deeper structures had increased echogenicity and overall thickness of the compressed breast was also reduced. [2] Attenuation of US waves through compressed breast appears to be substantially lower than uncompressed breast and shadowing artifacts were also reduced. One of the main reasons behind improved image quality is the nearly normal incidence of US waves as the interface between various tissue structures are flattened, resulting in low attenuation, higher reflection and deeper penetration of acoustic energy. If done in the mammographic

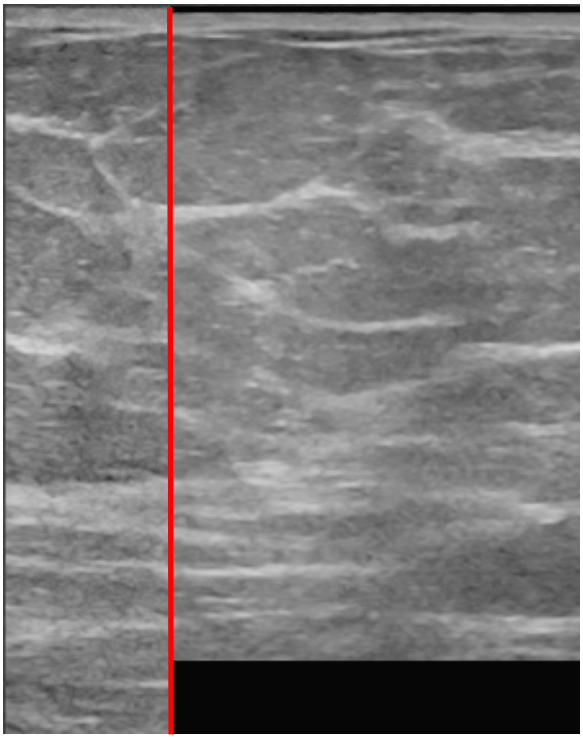

Figure 7.2: 2D composite registered image of locally compressed 2D breast image (left) and global compressed image (right). Notice the increase in depth of penetration of acoustic waves with local compression and also continuity of structures at various depths by registration.

view, one might still, *via* IVBaR, be able to employ local compression to obtain the improved image of the breast still registered to a 3D tomosynthesis mammography image volume. In a test by our group, the breast of a volunteer was uniformly compressed with a flexible mesh paddle and rescanned with the mesh relaxed and the scanning transducer compressing the breast under manual pressure. These two US image volumes were registered and the initial results are encouraging. Shown in Figure 7.2 is a composite registered 2D breast image of the local compression (left) *vs.* mammography-style global compression alone (right). The local compression flattens out structures increasing the depth of penetration of US waves and improves image contrast.

7.3 IVBaR and tumor volume estimation

In chapter 3, quantitative 3D-US imaging was performed for estimation of tumor volume using IVBaR. We studied patients undergoing chemotherapy throughout the multiple stages of the procedure. IVBaR performed successfully in 12 of 17 longitudinal scans with MRE = 5.2±2 mm and on 9 of 10 repeat scans with MRE = 3.2±1.2 mm. A reduced registration error in scans obtained in the same session might be expected compared with scans separated by a substantial time during chemotherapy. The mean percentage change in ratio of tumor volumes from the IVBaR based semi-automated method and the radiologist's manual segmentation method was 86±8% on 7 cases with tumor volume ranging between 0.1 to 2.1 cc. Measuring the accuracy of clinical registrations is very challenging in the absence of a "gold standard". For such evaluations, multiple observers may be required to mark landmark points as well as the boundary of the tumor. Also, registrations could be improved with better placement of initial control points and by adding more control points within the ROI. More work is needed in finding the optimal number of control points for a given image volume pair.

7.3.1 Digital Filtering

Some of the latest US scanners come with speckle-reduction software and compound imaging that produces images with better contrast, enhanced edges as well as

reduced speckle noise. Median filtering is a non-linear filter that reduces the 'salt and pepper' or speckle noise in US images while preserving details. Our hypothesis was that IVBaR could be improved by median filtering the US image volumes and initial results are encouraging. 2D and 3D median filters were designed according to the spatial resolution of US imaging system. The spatial resolution of M12L array transducer and GE Logiq-9 US system is given by the full width at half maximum (FWHM) of 0.23, 0.39 and 0.9 mm along the axial, lateral and elevational direction respectively. As resolution is better along axial and lateral direction than along the elevational direction, 2D and 3D median filters were designed with window sizes of 3x5 and 3x5x15, respectively. By applying the 2D and 3D median filters on the same image volume as in Figure 7.2, the corresponding composite images are displayed in Figure 7.3 (A) and (B).

Also, speckle reduction imaging available in the Logiq-9 US system was used to suppress the random speckle noise while enhancing the image edges and features.[3] In a pilot study on registration of whole breast ABU image volumes acquired before and during chemotherapy, MRE was 2.1±1.2 mm while 2D median filtering resulted in a decrease in MRE to 1.8±2.0 mm and speckle reduction imaging reduced it to 1.6±1.3 mm.

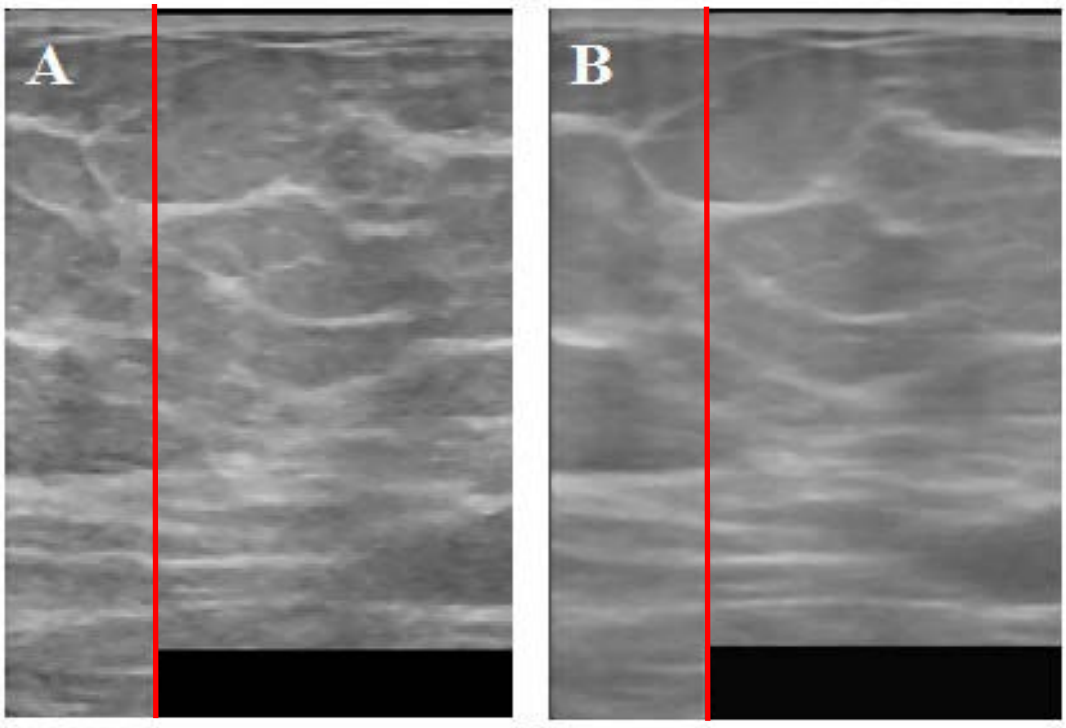

Figure 7.3: 2D composite registered images of locally compressed 2D breast image (left) and global compressed image (right) pre-processed using (A) 2D and (B) 3D median filters. Refer to text. Notice the decreased noise with filtering compared to Figure 7.2.

Filtering and speckle reduction algorithms are expected to achieve faster optimization and this needs to be studied further.

7.3.2 Robustness of IVBaR for clinical relevance

With radiologist identification of the tumor boundary in just one image volume, tumor boundary in the other stages could be automatically identified, provided the two image volumes were registered to each other. The main advantage of such automated tumor volume estimation was minimizing the necessity to manually identify the tumor boundary in subsequent scans thereby saving radiologist's time. Affine transformation could estimate the global changes (including positioning differences) in nearly real-time. However, non-rigid IVBaR is computationally intensive and hence mostly relegated to offline analysis with as yet limited clinical application until computational speed increases.

The necessity for robust and efficient registration as well as faster computing is increasing. Accelerated registration is gaining popularity with device drivers in graphics processing unit (GPU) powered by compute unified device architecture (CUDA). Non-rigid image registration could be accomplished within minutes if not seconds using GPUs, leading to more clinical impact not only in imaging but also in surgery and therapy.[4,5] Programmable GPUs have been used to register previously acquired CT images with intraoperative fluoroscopy images leading to better visualization of the anatomic structures and computer-aided surgery.[6]

With the emergence of multi-modal scanners for medical imaging like positron emission tomography (PET)/CT or PET/MRI, registration and fusion of anatomic and functional information holds a lot of diagnostic importance. In perfusion studies for imaging tumor metabolism, patients may not be able to be in the same position for extended periods and registration is vital to correct for positional and breathing motion. In interventional procedures, registration methods could be used to obtain real-time spatial information superimposed on preoperative images. Good segmentation could be achieved by lining up images to an atlas using image registration that helps in visualization and quantification.

Searching for information online has mostly been restricted to textual data. Some of the developments in the fields of image registration, pattern recognition and visual object recognition hold promise for image retrieval.

7.4 Non-rigid registration for interventional guidance

Electromagnetic (EM) tracking provides spatial and orientation information needed for accurate and precise navigation of tools like catheters, guide wires, needles, etc. used in minimally invasive surgery. The main sources of EM field distortion in CT scanner environment were the CT table and CT gantry with negligible contributions from the US system in the vicinity. Using precise spatial location information of the EM sensors along the 6 orientations from a 3D positioning system, mean positional error was reduced significantly from 3.9±2.8 mm for a rigid transform to 1.0±1.6 mm by a TPS transform (p-value<0.002). The error in sensor position as well as the orientation showed an increasing trend with increased distance of separation between EM sensor coil and EM field generator. Error in position and orientation of an EM sensor coil were shown to be dependent on the position as well as the orientation. While TPS-based non-rigid transformation modeling was performed on the position data along 6 orientations, modeling of orientation data at various spatial locations need to be studied further. In the future, custom designed CT scanners could be built with minimum use of metal for reduced distortion to the surrounding EM field. A relatively short-term alternative would be to provide software along with the CT scanner for real-time distortion correction based on non-rigid modeling.

7.5 Summary of Contributions

Some of the salient features of performing IVBaR in US image volumes in this dissertation include:

I. Registration assisted biometric of the finger for human identification and physiologic assessment and automated identification based on tolerance limits placed on the amount of rotation and scaling along the 3 axes.

II. Registration of sequential scans of breast cancers during treatment to
    - speed up and enhance confidence in manual tumor segmentation in subsequent studies
    - perform automatic segmentation of cancer in subsequent studies from: a) manual segmentation of first study; b) transforming the surface enclosing the mass to obtain tumor boundary in subsequent studies

III. Assessment of registration by
    - expert identification of homologous anatomical landmarks in the scans
    - independent validation by Doppler information.

IV. Registration to allow estimation and correction of field distortion in electromagnetic position sensors as used for real-time guidance of interventional procedures.

7.6 References

1 RC Booi, JF Krücker, MM Goodsitt, M O'donnell, A Kapur, GL Lecarpentier, MA Roubidoux, JB Fowlkes, PL Carson, "Evaluating thin compression paddles for Mammographically compatible ultrasound," Ultrasound Med. Biol. 33(3), 472–482, 2007.

2 M Halliwell, S Curtis, "Ultrasound breast imaging: A 3-dimensional approach, work-in progress," Ultrasound visions, 12, 67–75, 2008. http://www.visions-journal.com/GB-2008-V12/S67-75.pdf

3 Andy Milkowski, Yadong Li, David Becker, Syed O. Ishrak. Speckle reduction imaging. White paper - GE Healthcare (Ultrasound), last accessed on Oct 14, 2009 and available: http://www.gehealthcare.com/usen/ultrasound/education/docs/whitepaper_SRI.pdf

4 C Vetter, C Guetter, C Xu, R Westermann, "Non-rigid multimodal registration on the GPU," Proc. SPIE Medical Imaging: Image processing 6512, 651228, 2007.

5 SS Samant, J Xia, P Muyan-Ozcelik, JD Owens, "High performance computing for deformable image registration: Towards a new paradigm in adaptive radiotherapy," Med. Phys. 35(8), 3546–3553, 2008.

6 F Ino, J Gomita, Y Kawasaki, K Hagihara, "A GPGPU approach for accelerating 2-D/3-D rigid registration of medical images," In Parallel and Distributed Processing and Applications (ISPA), vol. 4330 of LNCS, pp. 939–950, 2006.